AD NUMBER

AD840269

NEW LIMITATION CHANGE

TO

Approved for public release, distribution unlimited

FROM

Distribution authorized to U.S. Gov't. agencies and their contractors; Critical Technology; AUG 1968. Other requests shall be referred to Air Force Flight Dynamics Lab., AFSC, Wright-Patterson AFB, OH 45433.

AUTHORITY

AFFDL ltr, 1 Feb 1973

AFFDL-TR-67-192
VOLUME II

AD-840269

ESTABLISHMENT OF AN UNSYMMETRICAL WAKE TEST CAPABILITY FOR AERODYNAMIC DECELERATORS

VOLUME II. ANALYSIS OF HIGH-SPEED AXISYMMETRIC WAKES AND PARASONIC PARACHUTE PERFORMANCE

DANIEL W. HENKE

Goodyear Aerospace Corporation

TECHNICAL REPORT AFFDL-TR-67-192, VOLUME II

AUGUST 1968

Best Available Copy

AIR FORCE FLIGHT DYNAMICS LABORATORY
AIR FORCE SYSTEMS COMMAND
WRIGHT-PATTERSON AIR FORCE BASE, OHIO

NOTICES

When Government drawings, specifications, or other data are used for any purpose other than in connection with a definitely related Government procurement operation, the United States Government thereby incurs no responsibility nor any obligation whatsoever; and the fact that the Government may have formulated, furnished, or in any way supplied the said drawings, specifications, or other data, is not to be regarded by implication or otherwise as in any manner licensing the holder or any other person or corporation, or conveying any rights or permission to manufacture, use, or sell any patented invention that may in any way be related thereto.

This document is subject to special export controls, and each transmittal to foreign governments or foreign nationals may be made only with prior approval of the Air Force Flight Dynamics Laboratory (FDFR), Wright-Patterson Air Force Base, Ohio 45433.

The distribution of this report is limited because the report contains technology identifiable with items on the strategic embargo lists excluded from export or re-export under U.S. Export Control Act of 1949 (63 Stat. 7) as amended (50 U.S.C. App. 2020.2031) as implemented by AFR 400-10.

Copies of this report should not be returned unless return is required by security considerations, contractual obligations, or notice on a specific document.
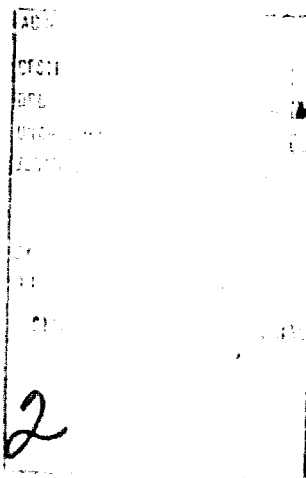
FOREWORD

The work described in this report was performed by Goodyear Aerospace
Corporation (GAC), Akron, Ohio, under USAF Contract AF33(615)-3595.
The contract was initiated under Project 6065, "Performance and Design of
Deployable Aerodynamic Decelerators," Task 606507, "Aerodynamic Decel-
erator Free-Flight Performance at High Mach Numbers." The program was
administered by the Air Force Flight Dynamics Laboratory, Air Force Sys-
tems Command, Wright-Patterson Air Force Base, Ohio Mr. W. R. Pinnell
and Mr. C. A. Babish III, (FDFR), were project engineers.

The work covered in this report was initiated on 1 March 1966 and completed
on 15 January 1968. The report was submitted in March 1968.

This volume does not cover all the program's primary objectives. Volume I
of this report presents analyses and preliminary design efforts to determine
feasibility of reconfiguring a free flight decelerator test vehicle by means of
an inflatable appendage in order to simulate the wake of a lifting body. Vol-
ume III contains a tabulation of wake survey and body surface pressure data
obtained from wind-tunnel tests conducted during this program.

The contractor's report number is GER-13528.

The authors and contributing personnel of Goodyear Aerospace Corporation
are: J. T. McShera, project engineer; D. W. Henke, assistant project engi-
neer; S. A. Weinberg, boundary layer and wake analyses; I. M. Jaremenko
parachute performance analysis and drag prediction; and F. A. Pake, aero-
dynamics consultant.

Special acknowledgment is made of conscientious support of Dr. R. M. Nerem
of Ohio State University who, in his activities as a consultant, added technical
assistance to the boundary layer and wake analyses.

This technical report has been reviewed and is approved.
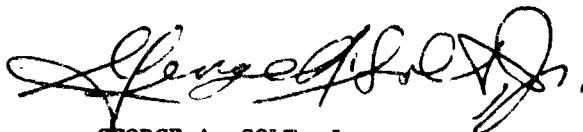
GEORGE A. SOLT, Jr.
Chief, Recovery & Crew Station Branch
Vehicle Equipment Division
AF Flight Dynamics Laboratory

ABSTRACT

Methods were developed to predict the boundary layer and wake characteristics of symmetric bodies m... at supersonic speeds. The methods developed for predicting boundary layer characteristics are applicable to both laminar and turbulent flow over axisymmetric or two dimensional bodies and can be used as an approximation for the flow over quasisymmetric bodies. The wake predictive methods were developed for axisymmetric flow and are applicable to both laminar and turbulent wakes. The aforementioned methods were combined and programmed such that wake profiles may be determined based only on inputs of forebody geometry and free stream conditions. Also presented is a method for calculating the drag of PARASONIC[1] parachutes using the flow field immediately ahead of the parachute as the free stream conditions. An analysis of the effects of various geometric and free stream parameters on PARASONIC parachute performance was conducted and trends determined.

The distribution of this abstract is unlimited.

---

[1] TM, Goodyear Aerospace Corporation, Akron, Ohio

TABLE OF CONTENTS

AFFDL-TR-67-192
Volume II

LIST OF ILLUSTRATIONS

LIST OF TABLES

(Reverse is blank)

LIST OF SYMBOLS

BOUNDARY LAYER ANALYSIS (SECTION II AND APPENDIXES I AND III)

a = speed of sound or semi-minor axis of ellipse

B = Equation 36

b = semi-major axis of ellipse

D = forebody base diameter

G_1 = Equation 34

h = enthalpy

h = h_w/h_{aw}

k = exponent from Equation 24

M = Mach number or boundary layer integrated momentum defect

M^* = wake integrated momentum defect

P = pressure

Pr = Prandtl number

R = base radius for axisymmetric body, or hydraulic base radius for non-axisymmetric body

Re = Reynolds number

R_T = transition Reynolds number

R_1 = gas constant

r = radial coordinate

s = distance from stagnation point measured along surface

$\tilde{s}$ = circumferential coordinate

T = temperature

$T_{r,1}$ = Equation 38

u = velocity

U'/U = free stream turbulence

V = velocity

x = axial coordinate of forebody

β = pressure gradient parameter, Equation 24

γ = ratio of specific heat capacities

θ = boundary layer momentum thickness

θ_{tr} = transformed boundary layer momentum thickness

μ = viscosity

ν = kinematic viscosity

ξ = Equation 24

ξ^* = Equation 27

ξ_T^* = Equation 41

ρ = gas density

ϕ = angular coordinate in plane normal to body axis of symmetry

Subscripts

a = adiabatic

e = edge of body boundary layer

s = nose stagnation conditions

w = body wall conditions

t = stagnation conditions

x_{tr} = value of x at transition

∞ = free stream conditions

$\theta_{critical}$ = momentum thickness at which the boundary layer becomes unstable to small disturbances

θ_{tr} = momentum thickness at transition

WAKE ANALYSIS (SECTION III AND APPENDIX IV)

a = velocity of sound

a_i = coefficients in velocity profile, i.e., Equation 5

$a_{1,2...}$ = enthalpy constants determined from boundary conditions

c_p = heat capacity at constant pressure

D = forebody base diameter

H = total enthalpy

h = enthalpy

K = turbulence constant in Equation 6

K_1, K_2, K_3 = constants in Equations 16 and 17

$\overline{M}_1$ = effective Mach number, Equation 17

M = Mach number

m = exponent in Equation 6

n = transformed coordinate, Equation 57; exponent, Equation 6

P = pressure

Pr = Prandtl number

p = exponent in Equation 6

P_t = total pressure

R = universal gas constant

Re = Reynolds number

Rs = shock radius

$\overline{R}_T$ = Townsend Reynolds number

r = radial coordinate

r^* = half-width at half-depth; see Equation 8

T = temperature

u = x-direction velocity component

V_∞ = free stream velocity

v = radial direction velocity component

X = downstream distance from forebody base

x_0 = rear stagnation point location

Y = vertical distance from forebody centerline (+ above and - below)

Z = horizontal distance from forebody centerline (+ right and - left, looking upstream)

γ = ratio of specific heat capacities

Δ = transformed wake radius or thickness

δ = wake radius or thickness

δ_D = wake diameter, $\delta_D = 2\delta$

δ^* = wake displacement thickness

η = nondimensional transformed radial coordinate

θ = momentum thickness

θ_T = enthalpy thickness

μ = viscosity

ξ = wake form parameter in Equation 63

ρ = gas density

Subscripts

B = forebody base where boundary layer separates

D = forebody diameter

L = local conditions

t = total condition

s = forebody surface condition

TR = transition condition

w = wall condition

x = distance from rear stagnation point

∞ = freestream condition

$\delta_{D_{TR}}$ = wake diameter at transition

θ = momentum thickness

0 = wake centerline conditions

1 = viscous wake edge condition

DRAG PREDICTION (SECTION V); PARASONIC PARACHUTE PERFORM-
ANCE (SECTION IV); WIND-TUNNEL TESTING AND DATA REDUCTION
(APPENDIX V)

A = area

a = camber

b = chord for linear downwash

C_D = drag coefficient

C_{D_P} = pressure drag coefficient

C_p = pressure coefficient

D = forebody base diameter; drag; parachute diameter

Di = inlet diameter of parachute

D_{open} = porous area equivalent diameter

DR = roof cap diameter

f = frequency

l_s = suspension line length

M = Mach number

NG = number of gores

NS = number of suspension lines

n = number of annular rings

P = pressure

q = dynamic pressure

R = maximum radius of parachute

Re = Reynolds number

r = radius of ring of differential width ds

r_i = inlet radius of ring of constant pressure differential

r_o = exit radius of ring of constant pressure differential

WR = width of radials

X = downstream distance from forebody base

Y = vertical distance from forebody centerline (+ above and - below

Z = horizontal distance from forebody centerline (+ right and - left, looking upstream)

α_c = angle between chord and skirt axis

$\beta = \sqrt{M^2 - 1}$

λ_g = geometry porosity

λ_T = total porosity

ϕ = angle between a line tangent to parachute canopy and parachute centerline

Subscripts

b = forebody base or breathing

c = constructed or canopy

e = mesh opening

f = drag oscillation

i = inlet

L = local conditions

o = stagnation conditions

p = projected

t = total conditions

exp = experimental

ext = external

int = internal

α = canopy oscillation angle

1 = conditions forward of shock wave

2 = conditions aft of shock wave

∞ = free stream conditions

FOREBODY FLOW FIELD PROGRAM (APPENDIX II)

i = axial indexing parameter

M = Mach number

p = pressure

R = average base radius

r = radial coordinate normal to body centerline

γ = ratio of specific heats

θ = angle of the forebody surface with the body axis in each ϕ plane

θ_c = critical cone angle for attached shock

ϕ = Reference plane passing through body centerline

Subscripts

e = Conditions at boundary layer edge

o = local stagnation conditions

s = nose stagnation conditions

∞ = free stream conditions

(Reverse is blank)

SECTION I

INTRODUCTION

As a portion of the Establishment of an Unsymmetrical Wake Test Capability for Aerodynamic Decelerators (EUREKA) program sponsored by the Air Force Flight Dynamics Laboratory (AFFDL), a study was performed to analyze performance characteristics of supersonic parachutes operating in the wakes of both axisymmetric and asymmetric forebodies and to develop the capability to analytically predict the performance of a parachute operating in the wake of an axisymmetric forebody. The results of that study are presented in this volume.

In order to predict the parachute performance, the properties of the wake flow field in which the parachutes operate and the forebody flow field properties that establish the development of the wake flow field had to be determined. The three basic tasks performed were:

1. Analysis of the flow field and boundary layer characteristics of the axisymmetric forebodies

2. Determination of the viscous and inviscid wake flow field characteristics behind these forebodies

3. Prediction of the drag performance characteristics of the parachute operating in the wake of such forebodies

Presented in Section II is a method for determining the flow properties over the forebody and the boundary layer momentum thickness and momentum defect on the body. The inviscid flow properties necessary for the boundary layer analysis are computed using Newtonian and tangent cone theories, where the tangent cone theory is based on the Taylor-Maccoll conical flow solution. The laminar compressible boundary layer characteristics are determined by using a local similarity solution, and the turbulent boundary layer is analyzed by using an integral method. An approximate criterion for the boundary layer transition point also is given.

Presented in Section III is a momentum integral solution for laminar and turbulent viscous wake characteristics and a mass flow balance solution for the inviscid wake characteristics. The viscous wake theory is based on the assumption that the details of the base flow and free shear layer regions may be largely ignored, thus allowing the wake momentum defect to be equated to the forebody momentum defect. Boundary layer type equations then can be applied to the wake flow region downstream of the wake rear stagnation point. Also presented in Section III is a method for determining inviscid wake characteristics by a mass flow balance that is performed with the forebody bow shock shape.

Based on the viscous and inviscid wake solutions along with the computed forebody characteristics, comparison of predicted wake profiles has been made with experimental wake profile data obtained from EUREKA wind-tunnel tests behind an Arapaho C with nose cone forebody. These correlations

indicate that excellent agreement between wake theory and experiment can be obtained using the methods presented in this volume. The wake methods of solution, as well as the forebody methods of solution, have been programmed in FORTRAN IV for use on the IBM 360, Model 40, and IBM 7094 computers. This computer program was used in making all the wake comparisons shown.

Section IV contains an analysis of the effects of Mach number, Reynolds number, forebody shape, canopy location, and canopy size on PARASONIC[1] parachute performance.

Section V presents a method for calculating the pressure drag coefficient of a PARASONIC parachute operating in the wake of an axisymmetric forebody. Comparisons of calculated and experimentally determined drag coefficients are presented also and show good agreement.

Other sections of this volume contain conclusions, recommendations for future work, and appendixes giving the details of the flow field analyses and wind tunnel tests.

This report does not cover all primary program objectives. Volume I presents analyses and preliminary design efforts to determine feasibility of reconfiguring a free flight decelerator test vehicle with inflatable appendage in order to simulate the wake of a lifting body.

Volume III contains a tabulation of wake survey and body surface pressure data obtained from wind tunnel tests conducted during the EUREKA program.

---

[1] TM, Goodyear Aerospace Corporation, Akron, Ohio.

SECTION II

BOUNDARY LAYER ANALYSIS

1. BOUNDARY LAYER CHARACTERISTICS

In investigating the various characteristics of the viscous wake trailing a typical aerodynamic body, one of the dominant features is integrated momentum defect. The wake momentum defect, M^*, can be expressed as

$$M^* = \int_0^\infty \int_0^{2\pi} \rho u(u_1 - u) \, r d\phi \, dr ,$$

and for a wake in which there is little or no static pressure gradient, the momentum defect remains invariant as the wake develops in the downstream direction. Furthermore, by neglecting the details of the base flow and shear layer regions and assuming that no external work is done on the wake fluid in these regions, the wake momentum defect, M^*, may be evaluated by equating it to the integrated boundary layer momentum defect, M, at the trailing edge of the forebody. The equation at momentum defects provides a direct link between the viscous wake properties and the forebody configuration, and any attempt to predict the properties of the viscous wake behind a body must begin with some knowledge of the forebody trailing edge boundary layer momentum defect.

This section describes the development of a method for calculating the growth of the boundary layer momentum thickness and momentum defect over an aerodynamic body of arbitrary shape. In doing this, an extensive literature survey was made of the available literature on compressible boundary layer flow. The method finally chosen for use on the program is representative of the state of the art of present boundary layer theory. The resultant procedures developed yield solutions for two-dimensional or axisymmetric flow and are good approximations for quasi-two-dimensional or quasi-symmetric flows. The method of analysis as developed for laminar and turbulent flow has been programmed for use on high-speed digital computers and has been utilized to determine the momentum defect and momentum thickness on the Arapaho C vehicle with nose cone and on a blunted elliptical cone configuration.

2. BOUNDARY LAYER CALCULATION METHODS

a. Laminar Boundary Layer

Kemp, Rose, and Detra (Reference 1) have studied the compressible laminar boundary layer, including effects due to pressure gradient and due to chemical dissociation. The former effect has been investigated through the study of similar solutions that may be obtained for cases in which the boundary layer pressure gradient parameter, β, is constant with respect to surface distance. Although for most cases of interest β is not constant over the entire surface of a body, it has been generally accepted that the results of such calculations still may be applied in

engineering calculations if the local value of the pressure gradient parameter, β, is used (References 2 and 3). This application is called the concept of "local similarity." Lees in Reference 4 has shown that for highly cooled boundary layers the effect of the parameter β is small and may even be neglected entirely for heat transfer calculations. However, for skin friction calculations and for cases where the wall temperature is comparable to the free stream total temperature, β still can have an important effect. Within the assumption of local similarity, however, this influence may be accounted for by using the local value of β.

As was indicated, Kemp, Rose, and Detra also have included effects due to dissociation by using the binary model of Fay and Riddell in Reference 5. The results obtained indicate no important effects for catalytic or near catalytic surfaces; and thus, for the analysis described herein the gas is treated as thermally and calorically perfect.

Stetson in Reference 6 has presented an empirical correlation of the results of the numerical solution for momentum thickness, θ, of Kemp, Rose, and Detra which is given by Equation 24 (Appendix I). This equation applies to two-dimensional or axisymmetric flows and can be used with reasonable accuracy for quasi-symmetric flows such as that over elliptical cones. Knowing the equation for the momentum thickness, θ, and knowing the inviscid flow properties at the edge of the boundary layer (from Item 3 below), the momentum thickness and the momentum defect

$$M = \int_{circumference} \rho_e u_e^2 \theta \, d\tilde{s}$$

can be evaluated. The details of this development are given in Appendix I.

b. Turbulent Boundary Layer

The state of knowledge of turbulent boundary layers is not as well developed as that of the laminar case. Although there have been many approximate treatments of turbulent flow, most of which can be supported to one degree or another by some of the existing experimental data, there are no "exact" theoretical solutions such as that of Kemp, Rose, and Detra for laminar flow.

One approximate solution, the results of which lend themselves to the present problem, is that of Reshotko and Tucker (Reference 7). This solution uses the momentum integral and moment-of-momentum equations and is simplified by using Stewartson's transformation from Reference 8. In order to solve these two equations, a skin friction relation must be used. Reshotko and Tucker chose the Ludwieg-Tillman relation (Reference 9) in a form suitable for compressible flow with heat transfer through application of the reference enthalpy concept. The above equations were further simplified through the use of an approximate shear stress distribution and the power law velocity profile.

The moment-of-momentum equation is needed in order to account for pressure gradient effects on the boundary layer velocity profile. The

4

method o: Reshotko and Tucker, as applied to insulated surfaces, is quite well founded. However, for noninsulated or nonadiabatic wall cases, the method (though qualitatively correct) is based on some speculative assumpti ns. It is still anticipated, however, that for such cases the method will yield reasonable quantitative results. The method certainly is representative of the best solution that can be obtained within the present status of turbulent flow theory.

Reshotko an Tucker have presented their results in terms of a transformed momentum thickness, θ_{tr}, given by the equation

$$\theta = \theta_{tr}(1 + \frac{\gamma - 1}{2} M_e^2)^3 .$$

If the boundary layer is turbulent over the entire body, the solution begins at the stagnation point. However, if the boundary layer is initially laminar, the calculation must begin at the transition point. The transition point can be specified either in terms of a location or a transition Reynolds number, Re_θ, or it can be determined from the transition criterion developed in Item 3, b. This criterion has been programmed along with the turbulent boundary layer solution. The details of the solution for boundary layer momentum thickness and momentum defect are given in Appendix I along with the basic elements of the programmed boundary layer solution.

3. SUPPORTING ANALYSES

a. Forebody Inviscid Flow Field

In order to evaluate the boundary layer momentum thickness and momentum defect, the inviscid flow field characteristics at the edge of the boundary layer must be determined. In particular, for the programmed boundary layer analysis, the following flow properties must be evaluated along the forebody: (1) P_e/P_0, (2) P_0/P_s, and (3) M_e. A general computation procedure was developed to calculate the flow properties along the forebody based only on inputs of free stream conditions and forebody geometry.

The procedure is applicable for a wide range of free stream conditions and is suitable for quasi-symmetric geometries as well as for axisymmetric and two-dimensional bodies. A tangent cone method of solution was used to obtain the flow properties for sharp-nosed bodies and a combination of Newtonian and tangent cone methods was used for a blunt-nosed configuration. To this end, a Taylor-Maccoll conical flow solution was programmed along with a logic procedure for the application of the tangent cone and Newtonian methods to quasi-symmetric forebody geometries. The logic procedure is shown in Appendix II.

The use of Newtonian theory and tangent cone theory is sufficient to yield solutions for pressure and Mach number within 10 to 20 percent accuracy, which is quite sufficient for engineering purposes. Since the momentum defect varies as the square root of the pressure, a 20-percent error in pressure would cause less than a 10-percent error in

momentum defect. Note also that the effects of boundary layer separation on the pressure are not considered in this analysis.

b. Boundary Layer Transition

In order to make use of the turbulent boundary layer analysis, it is necessary to determine the location at which transition occurs. As a part of the computer program developed to predict boundary layer momentum defect, three choices exist for determining transition:

1. Input the transition point location

2. Input the transition Reynolds number, $Re_{\theta_{tr}}$

3. Compute $Re_{\theta_{tr}}$ based on a programmed transition criterion

The criterion developed to predict transition was based on a correlation by Dr. R. Nerem, consultant, of the form

$$Re_{\theta_{tr}} \approx 1000 \, (1 - 0.12 \, M^2 + 0.023 \, M^3)^{1/2}$$

$$(-2.29 + 17.38 \, \bar{h} - 18 \, \bar{h}^2 + 3.91 \, \bar{h}^3)^{1/2} , \qquad (1)$$

where

$$\bar{h} = h_w/h_{aw} .$$

For regions of adverse pressure gradients, such as in the vicinity of a compression surface, the $Re_{\theta_{tr}}$ is replaced with the critical Reynolds number given by

$$Re_{\theta_{critical}} = 163 \, (1 - 0.12 \, M^2 + 0.023 \, M^3)^{1/2}$$

$$(-2.29 + 17.38 \, \bar{h}^2 - 18 \, \bar{h}^2 + 3.91 \, \bar{h}^3)^{1/2} . \qquad (2)$$

These equations have been programmed as part of the boundary layer calculation procedure and are used if transition location or transition Re_{θ} is not specified. The evolution of the above equations and a general discussion of boundary layer transition may be found in Appendix III.

SECTION III

WAKE ANALYSIS

1. **WAKE REGIONS**

Analysis of the characteristics of high-speed wakes begins by examining
the various regions that comprise the conventional high-speed wake.
The five distinct regions of the high-speed wake shown in Figure 1 are:

1. Recirculating base flow

2. Free shear layer

3. Rear stagnation point and the neck region

4. Inner viscous wake (downstream of the neck)

5. Outer inviscid wake

Each of these regions has its own peculiar characteristics. The recir-
culating base flow region, for example, is boundary layer fluid entrained
due to the adverse pressure gradient associated with the deflection of
fluid at the axis of symmetry back into the streamwise direction. The
free shear layer is also boundary layer fluid; this fluid initiates the de-
velopment of the neck region, which is characterized by steep gradients
due to the presence of the recompression shock.

Aft of the neck region, the viscous wake develops in a rather orderly and
well-behaved manner. This viscous wake is the subject of Item 3 of this
section in which the conventional boundary layer equations, including the
various integral relations, are applied to the viscous wake and a momen-
tum integral method is used in obtaining a solution.

The outer inviscid wake also is shown in Figure 1. It surrounds the
viscous wake and reflects the nature of the forebody inviscid flow field
and, in particular, the curvature of the forebody bow shock wave and
the entropy gradient there produced. The inviscid wake is discussed in
detail in Item 4 of this section.

2. **VISCOUS WAKE MODELS**

Considering the viscous wake in more detail and the velocity profiles
shown schematically in Figure 1 in particular, it may be seen that for
the conventional high-speed wake, the centerline X-direction velocity,
u_o, increases with increasing distance downstream of the rear stagnation
point. In the far wake ($X/D >> 1$), the centerline velocity actually ap-
proaches asymptotically to the local free-stream velocity. For this
problem, the radial velocity gradient is zero at the centerline for all
of X, as are also the gradients in temperature, density, and the other
fluid properties. On the other hand, the outer edge of this viscous wake,
at least where the viscous and inviscid wakes are clearly separated
from one another, is defined in the usual manner for boundary layer
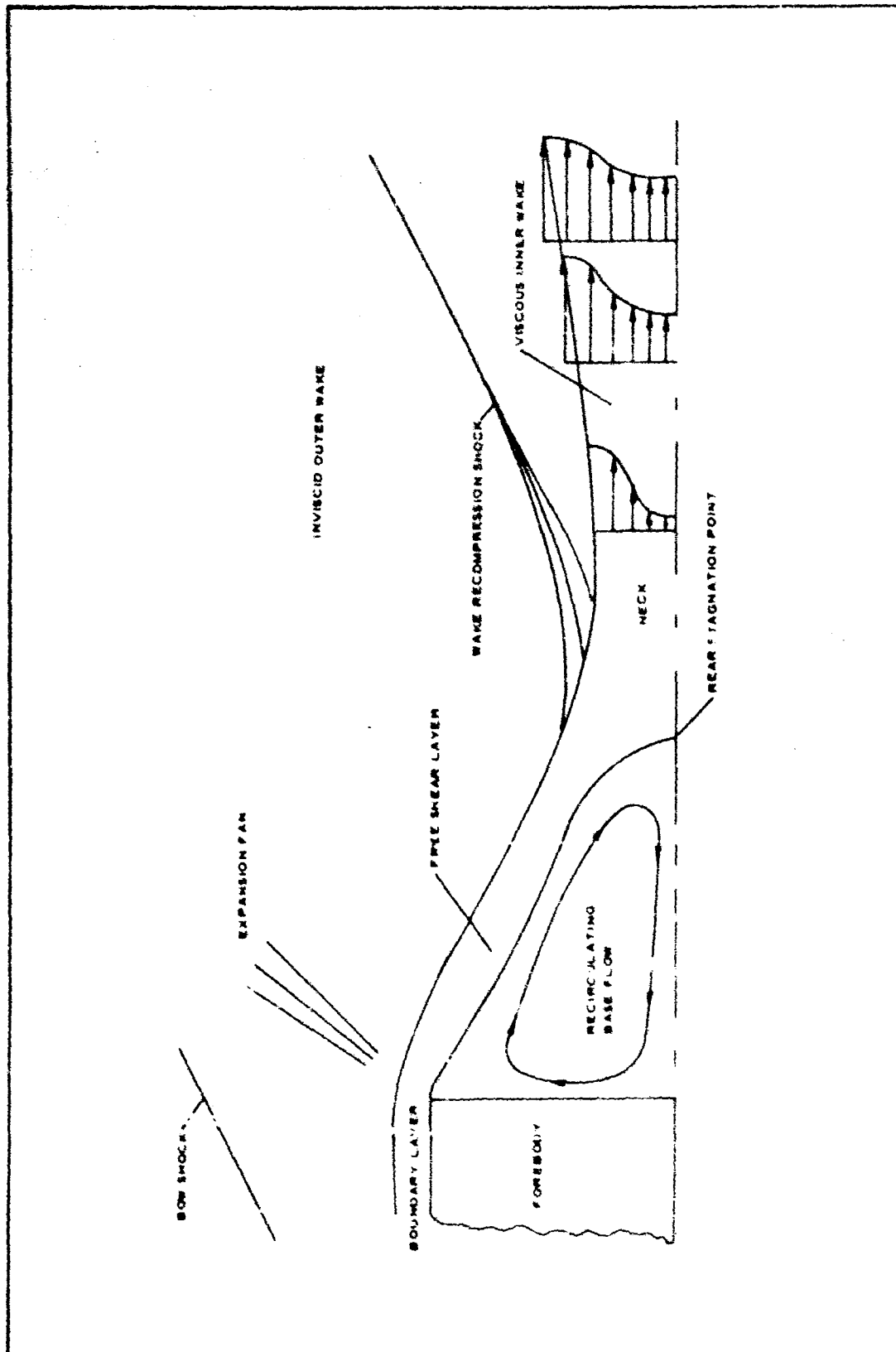
Figure 1 - Conventional High-Speed Wake

type flows. Here the properties are equal to their inviscid values, and
the gradients in these properties are zero. Furthermore, for the case
where viscous and inviscid wakes are clearly separated from one another
and in the absence of any pressure gradient, the momentum defect will
remain constant as the wake develops in the downstream direction.

When a decelerator is attached to a forebody by a cable and is positioned
in such a conventional high-speed wake, consideration must be given to
the extent to which the wake characteristics are altered due to the inter-
action of the forebody wake, the decelerator, and the tow cable that links
these two bodies. If the decelerator was located in the immediate neigh-
borhood of the base of the forebody, a conventional high-speed wake
would not have the opportunity to develop. In this case even the base
flow and free-shear layer would be completely altered (see, for example,
Figures 13 and 14 of Reference 10), and the proximity of the decelerator
to the base of the forebody might result in the presence of a strong ad-
verse pressure gradient in the largely subsonic cavity region separating
the two bodies. In this case, the wake growth is explosive and the de-
celerator, being immersed in a subsonic cavity type of flow, produces a
low drag coefficient.

If, however, the decelerator was located far downstream of the base of
the forebody, then very little alteration of the wake flow would be ex-
pected due to the interaction of the decelerator with the wake itself. In
this case the only alteration to the wake (except in the immediate vicinity
of the decelerator) is due to the presence of the tow cable or riser line.

If it is assumed for the limiting case described above that the cable dia-
meter is very small compared with the wake diameter, then the amount
of work done on the wake due to skin friction on the cable is negligible.
For this case, in the absence of any pressure gradient, both the wake
momentum defect and momentum thickness are constant in the axial
direction, exactly as in the conventional high-speed wake. However, at
least for laminar flow here, the similarity between these wakes ends
because in the present case, i.e. for the wake with a trailing decelerator
in it, the tow cable forces the wake centerline velocity to be zero. As-
suming further that the wake profiles are similar at all axial stations,
then the ratio of the wake momentum thickness to the wake diameter is
the same at all axial stations, and the conclusion is that the wake dia-
meter is constant with axial position. In other words, for this particular
case there is no wake growth such as is present in the conventional high-
speed wake. The wake is cylindrically shaped and does not change
characteristics in the axial direction. This is illustrated in Figure 2.

For the turbulent viscous wake, however, this cylindrical wake model is
not applicable. The turbulent wake in the presence of a tow cable or
riser line must include both a laminar sublayer and an outer turbulent
mixing layer. In this case, the effects of the tow cable are solely limited
to the sublayer region. This region, though not present in the conven-
tional wake, is such that it allows the no-slip condition to be satisfied
at the wall, i.e. the cable surface. At this region's outer edge, the
velocity is equal to that of the turbulent outer layer. This outer layer,
on the other hand, not being constrained by the no-slip condition at the
centerline, grows as in the case for the conventional turbulent wake.
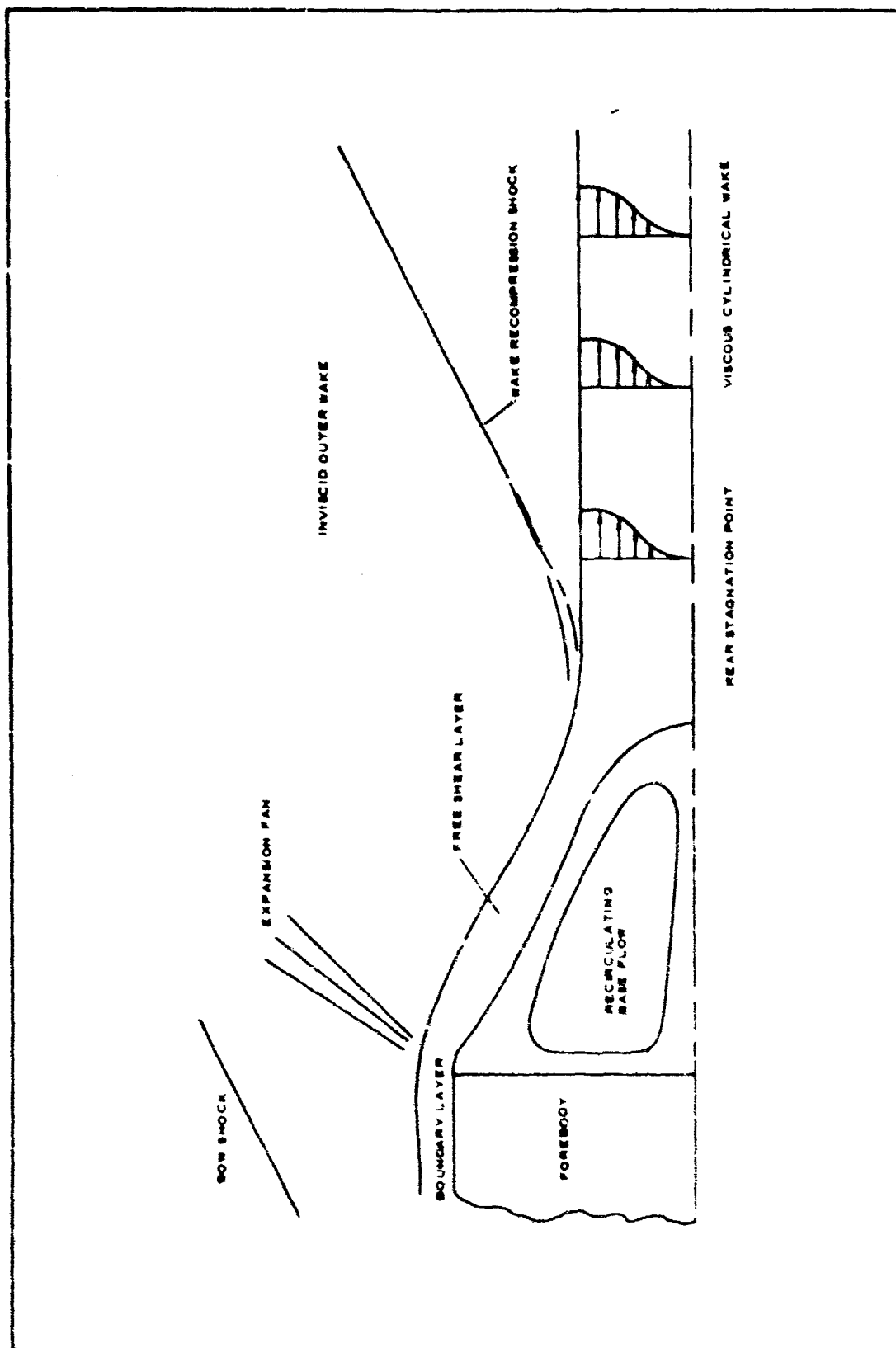
Figure 2 - "Cylindrical" Wake Model

For the condition of a contant viscous wake momentum defect (the
assumption of negligible work due to cable skin friction is still
made here), the velocity at the inner edge of the turbulent layer
increases just as the centerline velocity increases for the conven-
tional turbulent wake.

During the first series of wake survey tests (WT-IIA) conducted under
the EUREKA program, wake profile measurements were obtained behind
an axisymmetric cone-cylinder-flare-cylinder forebody with and without
a simulated riser line. These measurements are summarized in Fig-
ures 3 and 4 where impact pressure profiles at four different X/D sta-
tions are presented for Mach numbers of 2 and 5. There is virtually
no difference between the properties of these two kinds of wakes. Fur-
thermore, there is an obvious wake growth and the centerline region
velocity may be shown to increase with X/D for both cases. The turbu-
lent wake in the presence of a riser line is illustrated in Figure 5.

The discussions presented here concerning the nature of both laminar
and turbulent wakes in the presence of a tow cable or riser line are based
on only the preceding arguments and an extremely limited amount of ex-
perimental data. In spite of this, these models should prove useful in
engineering calculations. They do appear to be applicable for a wide
range of conditions in terms of Reynolds number, Mach number, etc.
They are, however, limited to the case where the radius of the tow cable
or riser line is much less than the wake momentum thickness and to
X/D > 3, avoiding the "strong interaction region."

3. VISCOUS WAKE ANALYSIS

a. Wake Flow Assumptions

An integral method of solution was applied to the problem of determining
the properties of both laminar and turbulent viscous wakes with parti-
cular attention to the problem of the wake flow preceding a trailing aero-
dynamic decelerator. In the paragraphs that follow, the theory will be
summarized for the different types of wake flows. The important assum-
ptions contained in the theory are as follows:

1. The fluid is thermally and calorically perfect, and
   there are no chemical reactions or other real gas
   phenomena.

2. The Prandtl number is unity ($Pr = 1$).

3. Prandtl's concept of viscous flow phenomena is valid
   for the high-speed compressible wake such that gra-
   dients in the streamwise or axial direction are much
   smaller than those normal to the wake axis and
   boundary layer type equations may be used.

4. The details of the base flow and free shear layer
   regions may be largely ignored. Thus, the region
   of validity for the present analysis must be con-
   sidered to extend from somewhere in the vicinity
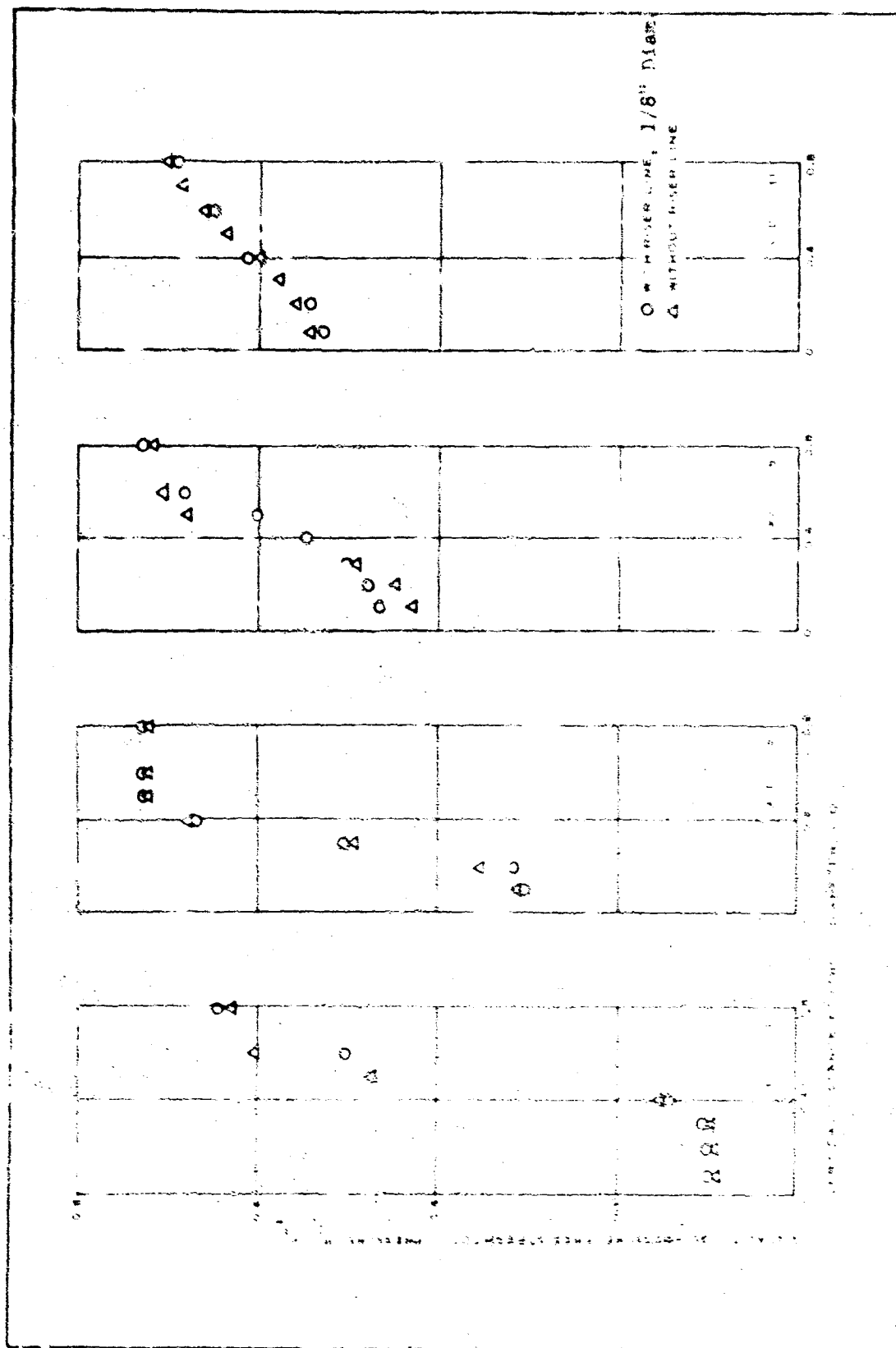
Figure 5 - Impact Pressure Profiles in Turbulent Viscous Wake with and
without a Riser Line ($R_{\infty D}$ - 2)
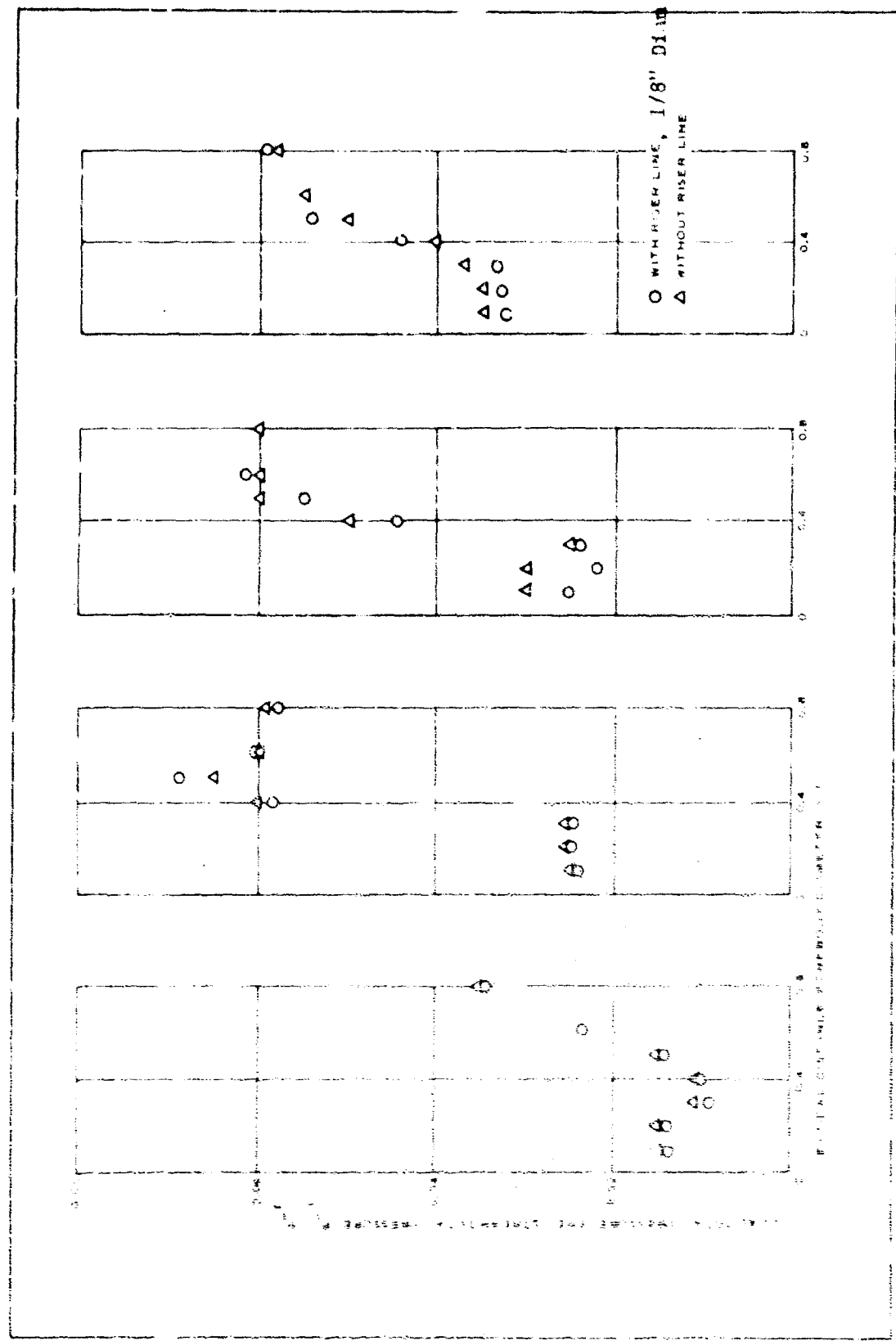
Figure 4 - Impact Pressure Profiles in Turbulent Viscous Wake with and without Riser Line ($M_\infty = 5$)
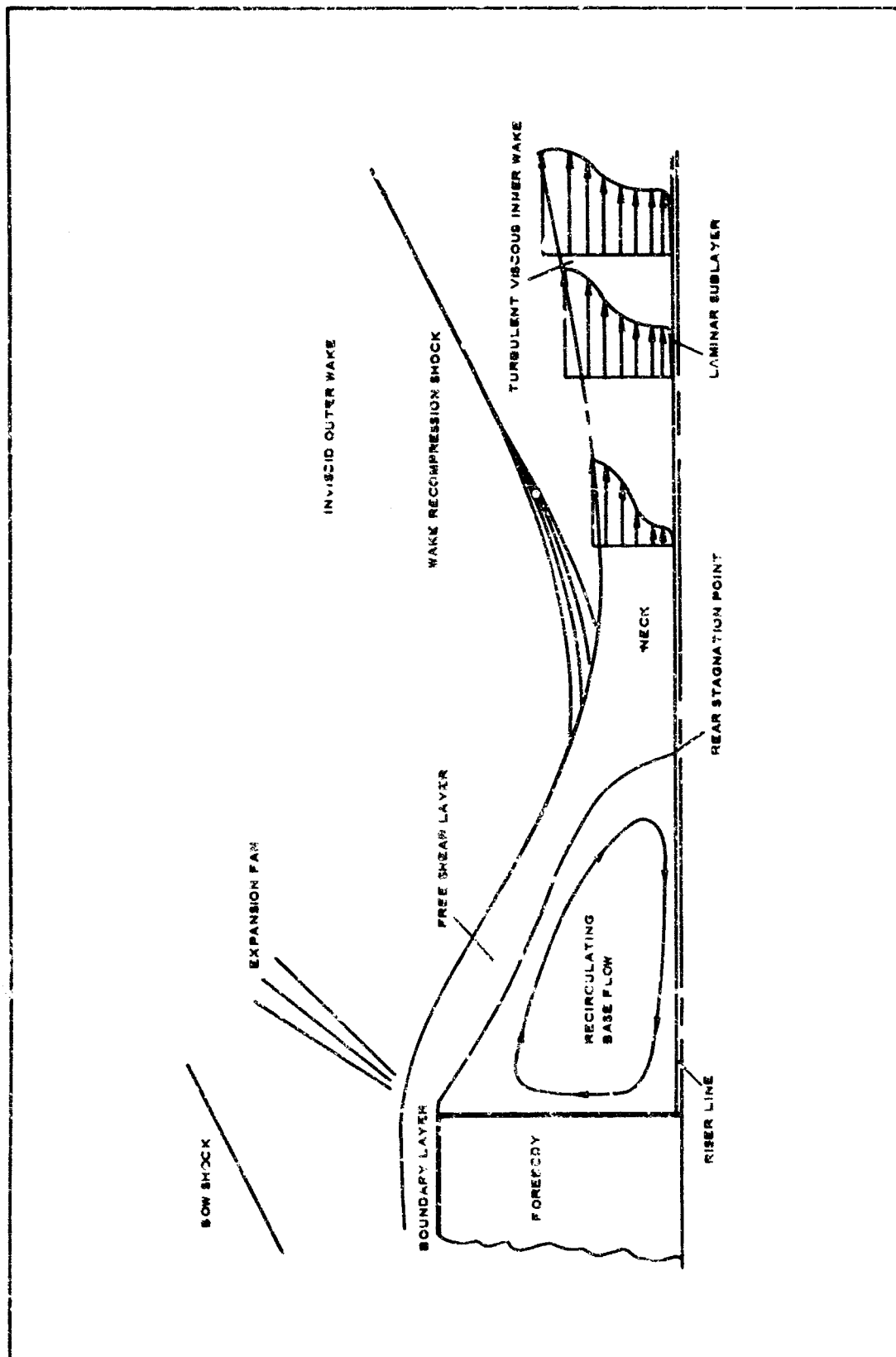
Figure 5 - Turbulent Wake in Presence of Riser Line

of the wake neck or further downstream and on
down into the far wake.

5. Effects due to the existence of an external pressure
gradient are negligible.

Note that this last assumption is not intended to restrict the solution to
flows with zero pressure gradient. The assumption only implies that
local acceleration in the inner wake itself is much more important than
acceleration due to an external pressure gradient. This assumption
allows the momentum integral equation to be simply written as

$$\rho_1 u_1^2 \, (\pi \, \theta_1^2) = 2\pi \int_0^\delta \rho u \, (u_1 - u) \, r dr \tag{3}$$

constant with respect to X.

Here θ is the momentum thickness and Equation 3 is simply a statement
to the effect that the wake momentum defect is constant in the axial di-
rection. Since the pressure gradient has been assumed to be negligible,
then there is no external work being done on the wake, and the momen-
tum defect must be constant.

As a check on the validity of the assumption of constant wake momentum
defect, experimental wake momentum defect values were calculated
from wake survey data obtained during wind tunnel tests conducted under
this program. In looking at the viscous wake, it was found that the width
of the wake decreased with increasing Mach number. For this reason,
the viscous wake momentum defect comparisons were conducted at
Mach 2. The comparisons were made for an axisymmetric spherical
nose cone-cylinder-flare forebody at a Mach number of 2 and a Reynolds
number of 0.369×10^6/in. The wake momentum defects were computed
at several wake stations using a data reduction program, which reduced
wake survey pressure and temperature data to local velocities. The
data reduction program used a linear variation between experimental
data points in computing momentum defects. The edge of the viscous
wake was determined by using the criterion that at the edge of the viscous
wake, the total pressure would be equal to the total pressure immediately
behind a normal forebody bow shock. The data reduction program chose
the data point having a total pressure closest to this pressure. The
spacing of the experimental data points was equal to one-tenth of the
forebody base diameter. The experimental wake momentum defects
also were compared with forebody momentum defect calculated using
the method described in Section II. The results of the comparison are
shown in Table I.

The tabulated values indicate that the method used for predicting the edge
of the viscous wake is not accurate enough to produce accurate experi-
mental wake momentum defect results. The $X/D = 3$ data are too near
the wake neck to be a useful profile for this study. The general decrease
in the momentum defect values from $X/D = 5$ to $X/D = 11$ is the result of
the inaccuracy in selection of the nearest experimental data point as the

15

TABLE I - VISCOUS WAKE MOMENTUM DEFECT COMPARISON

M_∞	Re_∞/in.	X/D	Momentum defect in Y plane (lb)	Wake radius, Y/D	Momentum defect in Z plane (lb)	Wake radius, Z/D	Forebody momentum defect (lb)
2	0.369×10^6	3	5.68	0.5	2.98	0.5	1.203
2	0.369×10^6	5	4.46	0.5	1.65	0.5	1.203
2	0.369×10^6	7	4.10	0.5	1.02	0.4	1.203
2	0.369×10^6	9	2.29	0.5	0.964	0.4	1.203
2	0.369×10^6	11	1.73	0.5	0.786	0.4	1.203

viscous wake edge. Since the wake is growing, the value of the momentum defect within a given circle will decrease with increasing X/D. The experimental data also may contain errors induced by the forebody mounting strut that spanned the wind tunnel in the Z plane. Within the limits of the accuracy of the experimental data and the computation method, the momentum defect is assumed to be constant. In an attempt to improve the method for computing the momentum defect in the wake, a polynomial curve fit technique was used to smooth the experimental data and therefore improve the accuracy of the calculation. Using the curve fit technique in the wake momentum defect calculations did not have an appreciable effect on the results.

Assumption 5 listed above thus does not limit the solution to wake flows with zero pressure gradient. However, the validity of the solution certainly does decrease with increasing pressure gradient. For blunt bodies with strong pressure gradients, the solution should be considered as being highly approximate.

By ignoring the details of the base flow and shear layer regions and assuming that no external work is done on the wake fluid in these regions, then the constant in Equation 3 may be evaluated by equating the momentum defect of the boundary layer at the base of the forebody to the momentum defect of the wake. This may be stated mathematically as

$$\rho_B u_B^2 (\pi \theta_B D) = \rho_1 u_1^2 (\pi \theta_1^2) \ , \tag{4}$$

where the subscript 1 refers to the properties associated with the outer edge of the wake and the subscript B, to properties at the base of the vehicle where the boundary layer separates. The symbols ρ_B and u_B represent inviscid properties, and D is the forebody base diameter. Next, the Dorodnitzyn transformation is introduced in order to obtain a solution to the axial direction momentum equation. In the integral method of solution, it is assumed that the velocity profile in the viscous wake may be expressed as a fourth-order polynomial of the form

$$\frac{v}{u_1} = \sum_0^4 a_i \eta^i \quad .$$

(5)

Applying the appropriate boundary conditions to the above equation, a solution for the viscous wake velocity profile in the transformed coordinate system may be obtained. Considering the energy equation for the assumption of Pr = 1 and applying the appropriate boundary conditions to the energy equation, the enthalpy profile in the transformed coordinate system is obtained as a function of ξ the form parameter as derived in Appendix IV.

The details of the above development are given in Appendix IV and apply to both laminar and turbulent viscous wake flows. The necessary equations for determining the properties of a high-speed compressible wake were derived using an integral technique and the Dorodnitzyn transformation. In order to describe the entire wake flow field, the inviscid flow field must be determined (see Item e., below) and that an estimate be made of the vehicle boundary layer momentum thickness (Section II above).

b. Laminar Axisymmetric Wake

Appendix IV describes the case of both the conventional laminar wake and the cylindrical laminar wake. In the appendix, the relationship between ξ and x is determined. For each case, it is necessary to specify a relation for the viscosity coefficient and, for both laminar flow cases, the viscosity is assumed to be linearly dependent with respect to fluid temperature; i.e., μ/RT = constant. For the cylindrical wake case, $u_0/u_1 = 0$, which is equivalent to $\xi = 24$ (Appendix IV). Thus, the properties of the cylindrical wake are solved by setting $\xi = 24$, and ξ will not depend on X for this case since there will be complete similarity between radial profile at each X direction station.

Having solved for ξ as a function of X (Appendix IV) together with the equations derived in that appendix for the velocity and enthalpy profiles and the relationship between the transformed and physical radial coordinates, the properties of the laminar viscous wake are completely known.

Using this theory, as shown in Figure 6, reasonable agreement is attainable even in the near wake region where the present theory should give the least reliable results. A further check on the laminar wake theory is presented in Figure 7 where the wake growth behind a conical body is presented as a function of distance downstream of the body. Figure 7 also shows both ballistic range experimental data from Reference 11 and the result of a theoretical calculation using the laminar wake method developed in Appendix IV. As may be seen, excellent agreement exists.

Unfortunately, good data does not exist at the present time for the laminar wake in the presence of a decelerator with which the laminar cylindrical wake results may be compared. Note that during the wind tunnel tests
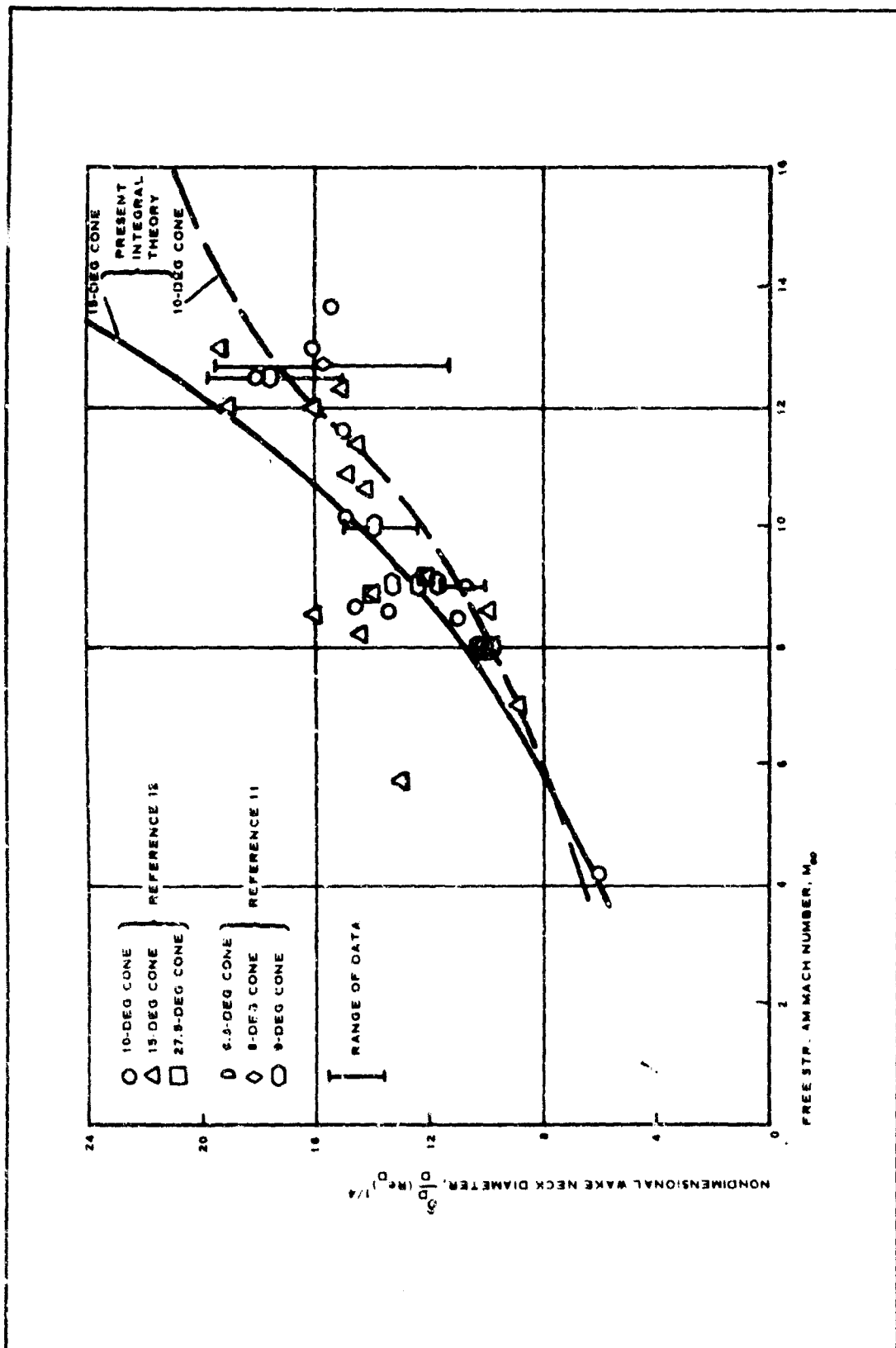
Figure 6 - Experimental Measurements of Neck Diameter for Laminar High-Speed Wake
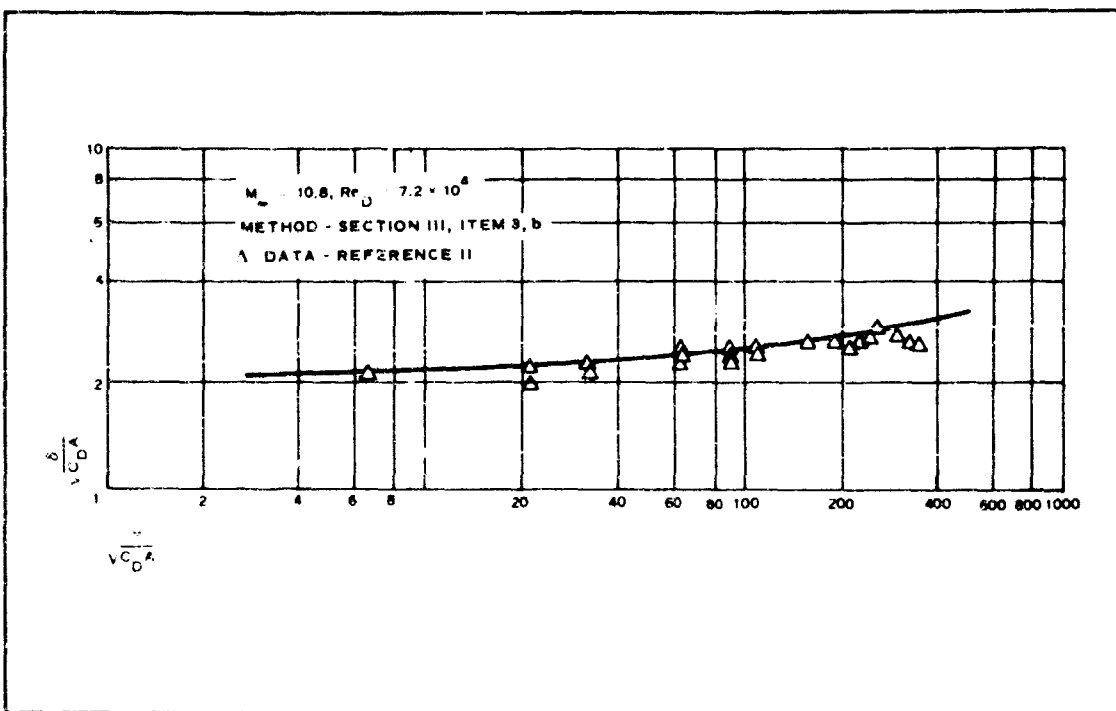
Figure 7 - Comparison of the Momentum Integral Method Solution with
Experimental Laminar Far Wake Data

performed as a part of this program only turbulent wakes were obtained.
It is felt, however, that since the conventional laminar wake results in
Figure 6 are for conditions similar to these of the cylindrical wake (for
example, the centerline velocity is low in the near wake region and the
velocity profile is similar to that of a cylindrical wake); and since
reasonably good agreement exists, then the laminar cylindrical wake
results should lead to equally good agreement.

c.   Turbulent Axisymmetric Wake

For the turbulent wake case, a form for the viscosity relationship must
be chosen different from that used for the laminar case. In turbulent
flow, the viscosity coefficient is only an effective one (artificially intro-
duced due to the manner in which the governing equations are expressed)
and is related to the momentum transfer caused by the fluctuating, mixing
type motion.   Many different mathematical forms for the turbulent visco-
sity coefficient have been suggested in the literature, and four of these, as
applied to the wake centerline, are summarized below (these four models
are virtually identical to those discussed in Reference 13):

$$\mu_0 = k\, \rho_0 u_0 \quad ,$$

$$\mu_0 = K \Delta\, (\rho_1 u_1 - \rho_0 u_0) \quad ,$$

$$\mu_0 = K \Delta \rho_1 (u_1 - u_0) \; ,$$

and

$$\mu_0 = K \Delta \rho_0 (u_1 - u_0).$$

While only the above models were considered in this investigation, the solution is not restricted to these viscosity models. In all of the above models, the value of the constant K is required. The first model relates the turbulent viscosity coefficient to the centerline momentum flux, the second model form involves a momentum difference, and the third and fourth models involve only a velocity difference. These latter models correspond to the accepted "classical" form for incompressible flow. However, the second model also reduces to a velocity difference for the incompressible case. The first model obviously does not reduce to the classical form for incompressible flow. In fact, the first model did not originate from classical viscous flow work, but from studies of jet-mixing phenomena. All of the above modes may be expressed using the general form written below:

$$\mu_0 = K \Delta \rho_1 u_1 \left(\frac{\rho_0}{\rho_1}\right)^m \left[1 - n - (-1)^n \left(\frac{\rho_0}{\rho_1}\right)^p \frac{u_0}{u_1} \right] \; . \tag{6}$$

In Table II, the values for the constants m, n, and p are presented. In the computer program for the viscous turbulent wake, the specification of the model number directs the program to use the proper values of m, n, and p.

The value of K must be determined from experiments. In low-speed flows, it is conventional to define μ_0, and thus K, through introduction of the Townsend Reynolds number, R_T, where

$$R_T = \frac{(u_1 - u_0) r^*}{\mu_0 / \rho_0} \; . \tag{7}$$

TABLE II - CONSTANTS FOR TURBULENT VISCOSITY RELATIONSHIP

Model	μ_0	m	n	p	Remarks
First	$K \Delta \rho_0 u_0$	1	1	0	Momentum flux
Second	$K \Delta (\rho_1 u_1 - \rho_0 u_0)$	0	0	1	Momentum difference
Third	$K \Delta \rho_1 (u_1 - u_0)$	0	0	0	Velocity difference
Fourth	$K \Delta \rho_0 (u_1 - u_0)$	1	0	0	Velocity difference

Here, r^* is the so-called half-width at half-depth, i.e., the radius at which the velocity is exactly intermediate to the axial and edge values, and R_T is the constant to be determined from experiment. For the second, third, and fourth models and in the limit of either incompressible flow or an "incompressible like" flow, i.e. the far wake where $\rho_O = \rho_i$, then K and R_T are related by

$$K = \frac{r^*/\Delta}{R_T} \quad . \tag{8}$$

For the polynomial velocity profile of Equation 65 of Appendix D, it follows that

$$\frac{r^*}{\Delta} \cong \eta^* \simeq 0.4 \quad ,$$

and thus

$$K \cong \frac{0.4}{R_T} \quad . \tag{9}$$

Typical experimental values for R_T are tabulated in Table III together with the value of K calculated from Equation 9. These values of K may be compared with those of Zakkay and Fox in Reference 13 where the first model is similar to their Model 1, the second model to their Model 2, the third model to their Model 2A, and the fourth model to their Model 4. Based on the analysis of wind-tunnel data, Zakkay and Fox concluded that a value of K = 0.01 for the second model and K = 0.04 - 0.06 for third and fourth models represented a best fit to their data. Zakkay and Fox also suggested a value of 0.02 for use with the first model. In project EUREKA, the best correlation with wind-tunnel wake test data has been obtained for values of K on the order of 0.005 to 0.01. Details of the comparison of the theory with experimental data will be given later in this section.

By substituting Equation 6 for the viscous wake into Equation 63, Appendix IV, for ξ, the form parameter, the relation between ξ and X can be determined.

TABLE III - TOWNSEND REYNOLDS NUMBER IN WAKE

Wake type	R_T	K
Axisymmetric, incompressible	14.1	0.027
Two-dimensional, incompressible	12.0	0.033
Two-dimensional, compressible	10.0	0.040
Axisymmetric, compressible	13.7	0.029

If the present method of solution and the turbulent viscosity coefficient models included in the analysis are accepted, then the resulting equations for ξ as a function X, together with the equations derived in Appendix IV for the velocity and enthalpy profiles and the relationship between the transformed and physical radial coordinates, are sufficient to completely determine the properties of the turbulent viscous wake. Again, the properties of the forebody boundary layer and at the edge of the viscous wake are assumed to be known from the forebody computer program.

Using the above method of analysis, the turbulent viscous wake characteristics were determined and comparisons were made with the velocity profiles obtained from wind-tunnel test data obtained in the wake of the Arapaho C vehicle with nose cone (Appendix V). These comparisons were based on the iterated wake solution described in Item 5 of this section. In Figures 8 through 23, the wake velocity profiles are shown plotted versus the nondimensional distance (Y/D or Z/D) measured from the centerline of the viscous wake. Comparisons are shown for a range of Mach numbers from 2 to 5 for two Reynolds number conditions and for stations behind the base of the forebody from 3 to 11 calibers, which is the region of interest for decelerator application.

The theory is shown as a solid line and represents the total wake description, i.e., both viscous and inviscid portions. The inviscid wake comparisons are further discussed in Item 4 of this section. The experimental velocity data points shown were calculated from the wake wind tunnel pressure measurements obtained as a part of this program. The disparity between the Y/D-plane data and the Z/D-plane data is at least partially due to the presence of the forebody mounting strut in the Z/D plane. However, this strut also may influence the Y/D data, and thus data for both planes is shown. Note also that at X/D = 3, there may be added inaccuracies in the data due to the influence of the rake used to obtain pressure readings.

The best correlation with the experimental EUREKA wake data has been obtained using the third viscosity model, $\mu_o = K \Delta \rho_1 (u_1 - u_o)$ with a viscosity coefficient K = 0.005. This K value, while below those normally used, was justified by considering that the solution had been iterated as explained in Item 5 of this section and thus had changed the boundary layer approach that originally defined the range of acceptable viscosity coefficient values. Using K = 0.005 for the third model (shown in Figures 8 through 15), agreement with experiment to well within 10 percent has been obtained in almost all cases over the range of Mach numbers and wake location considered in this program and for both Reynolds number conditions considered. For X/D > 3, the correlation of the centerline velocities is to within 5 percent in all but one case.

Correlation with the experimental data has been obtained using other viscosity models; the results using the fourth model are shown in Figures 16 through 19 for K = 0.010 and in Figures 20 through 23 for K = 0.005 in order to show the effect of changing viscosity model and/or viscosity coefficient. Using the fourth model, the results show that the trend of the predicted centerline velocity is affected by Mach number. At Mach 2 the predicted centerline velocity is significantly higher than
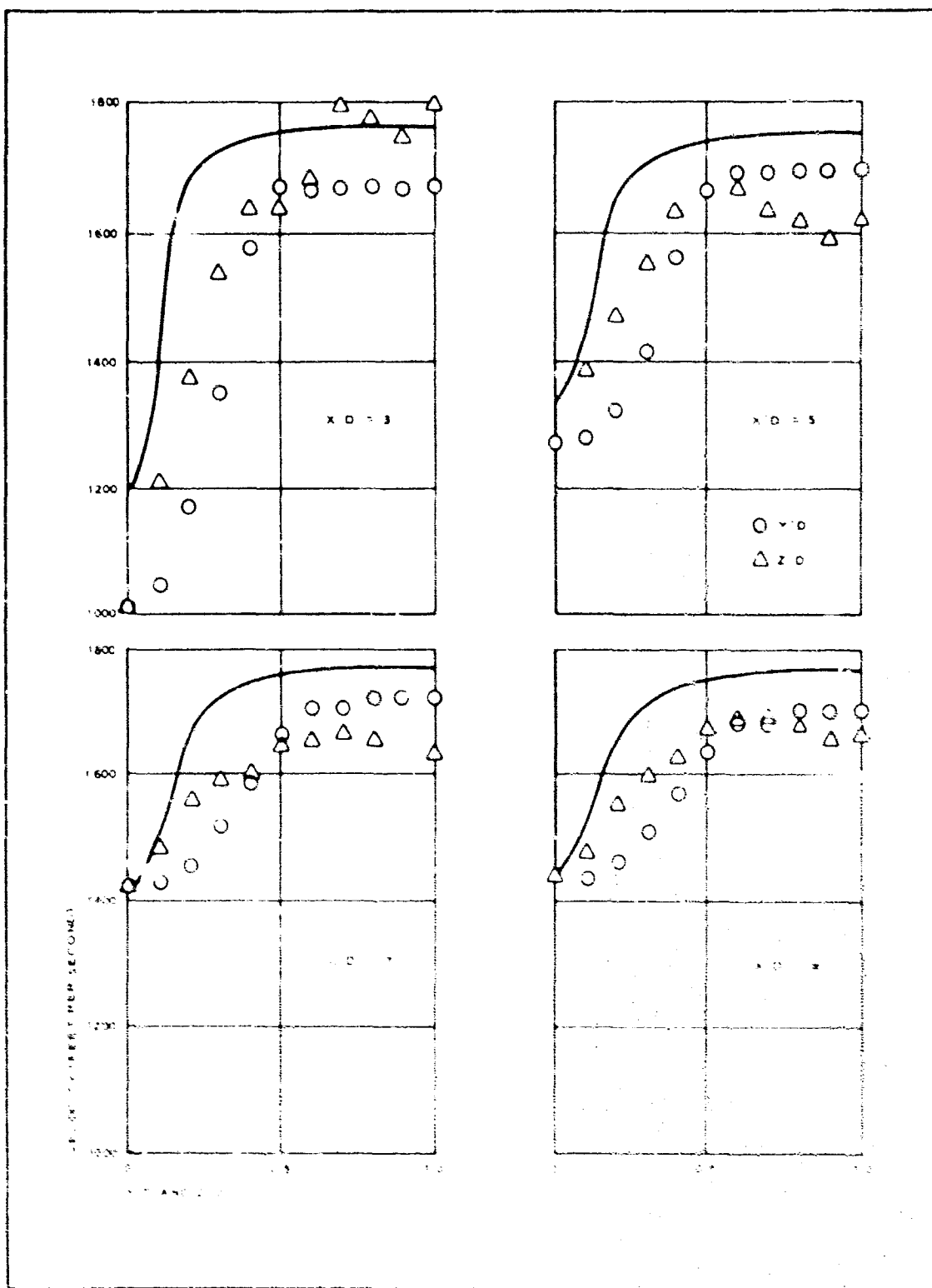
Figure 8 - Comparison of Experimental and Calculated Wake Profiles
$(M_{\infty} = 2,\ p_{\infty} = 2.5\ psi,\ Model\ K)$
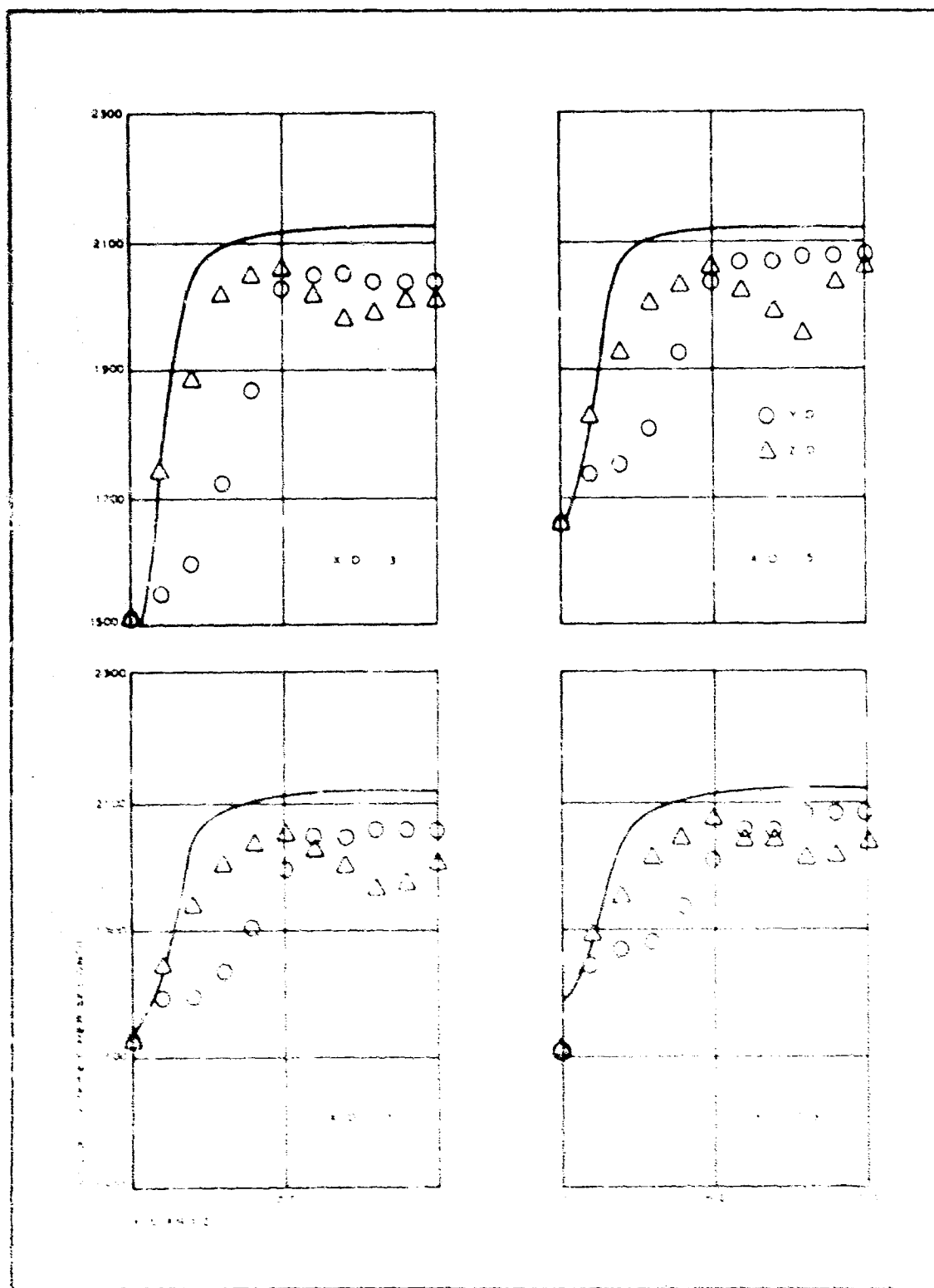
Figure 7 - Comparison of Experimental and Calculated Wall Pressure
($M_\infty = $ ..., $r_{nose} = $ ... psi, Model ..., $R = $ ...)
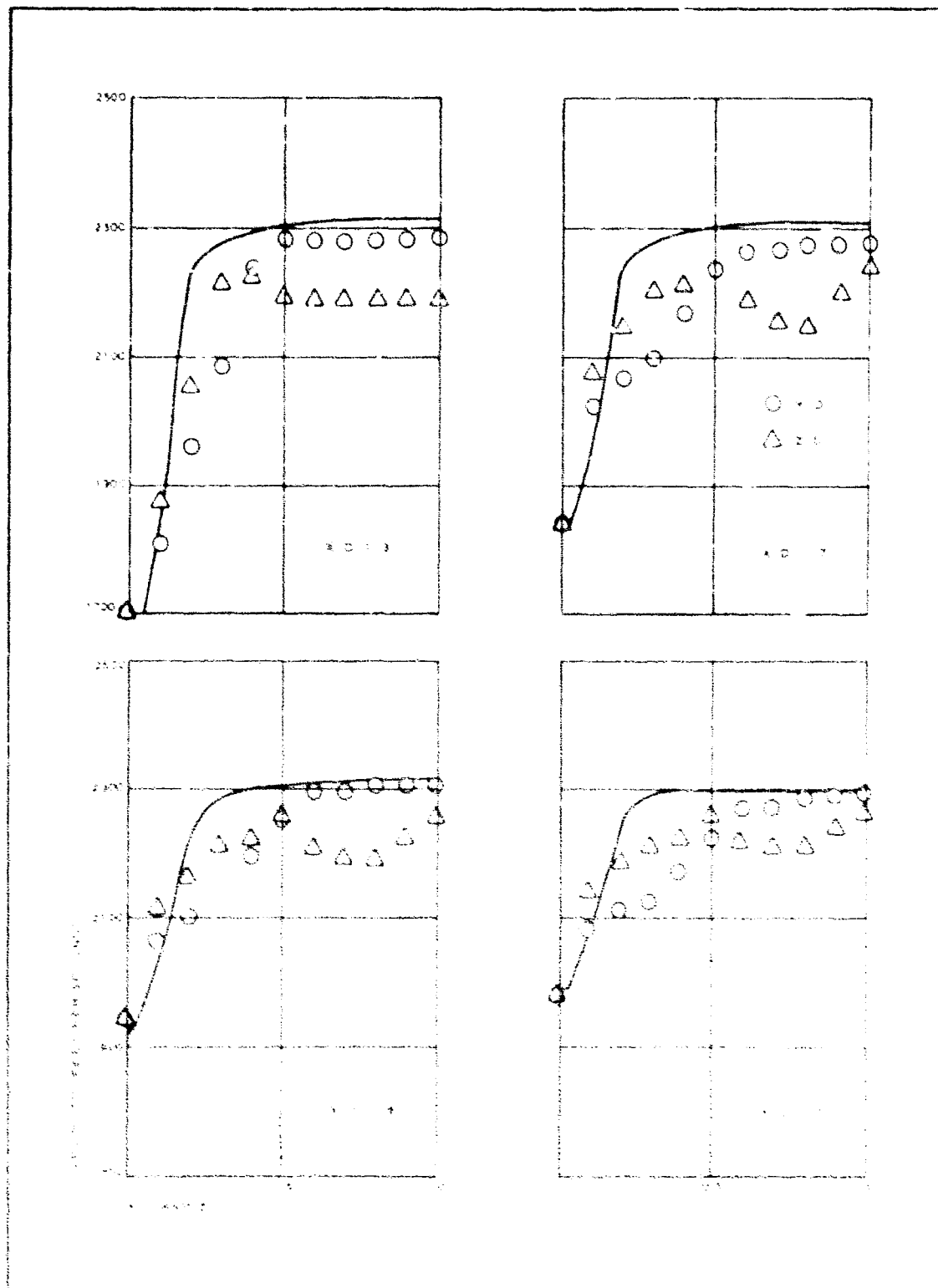
Figure 18 - Comparison of Experimental and Calculated Static Pressure
$M_3 = 4$, $P_1 =$ ... M ... R ...
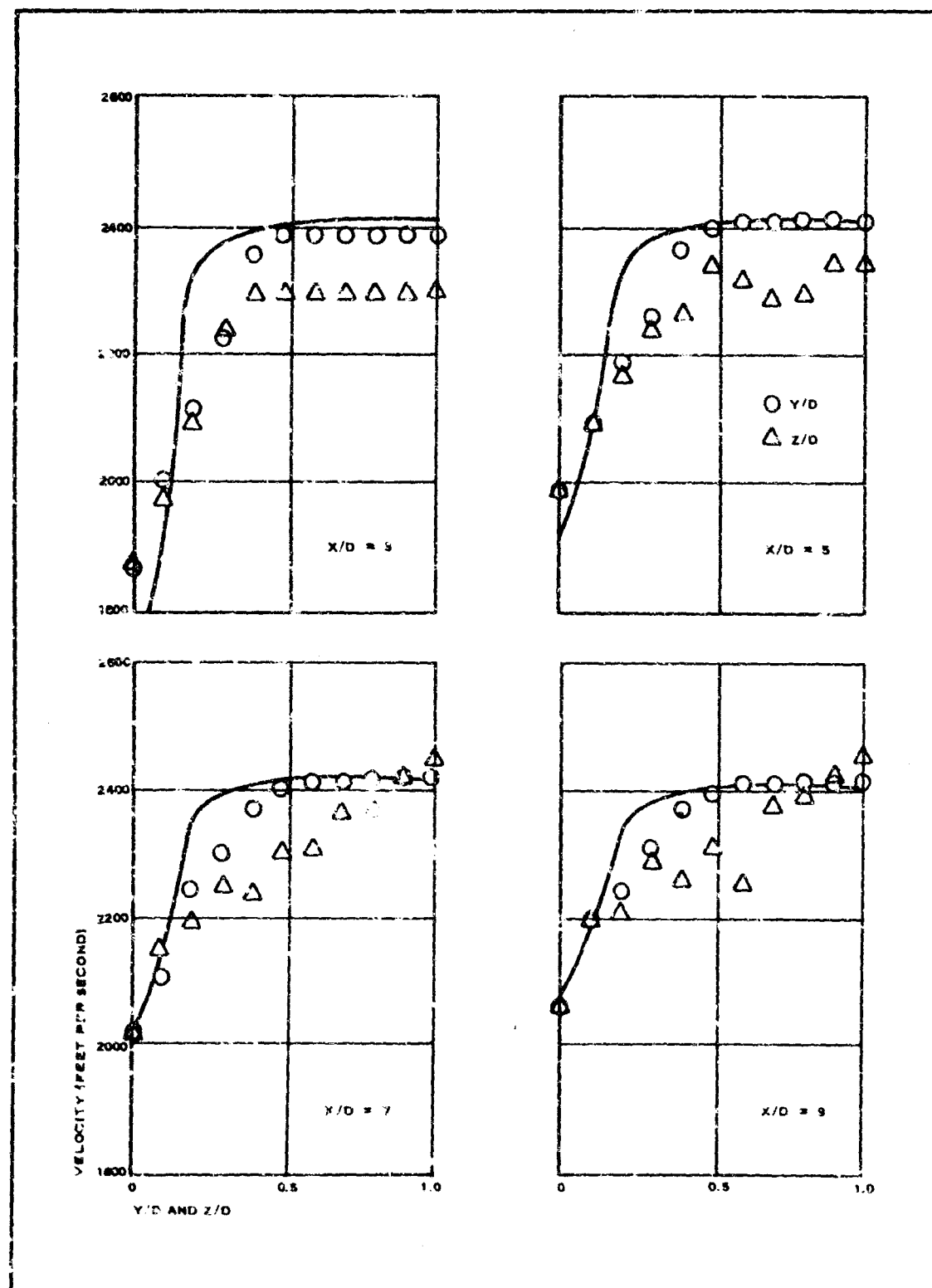
Figure 11 - Comparison of Experimental and Calculated Wake Profiles
(M_∞ = 5, P_{t_∞} = 30.5 psi, Model 3, K = 0.005)
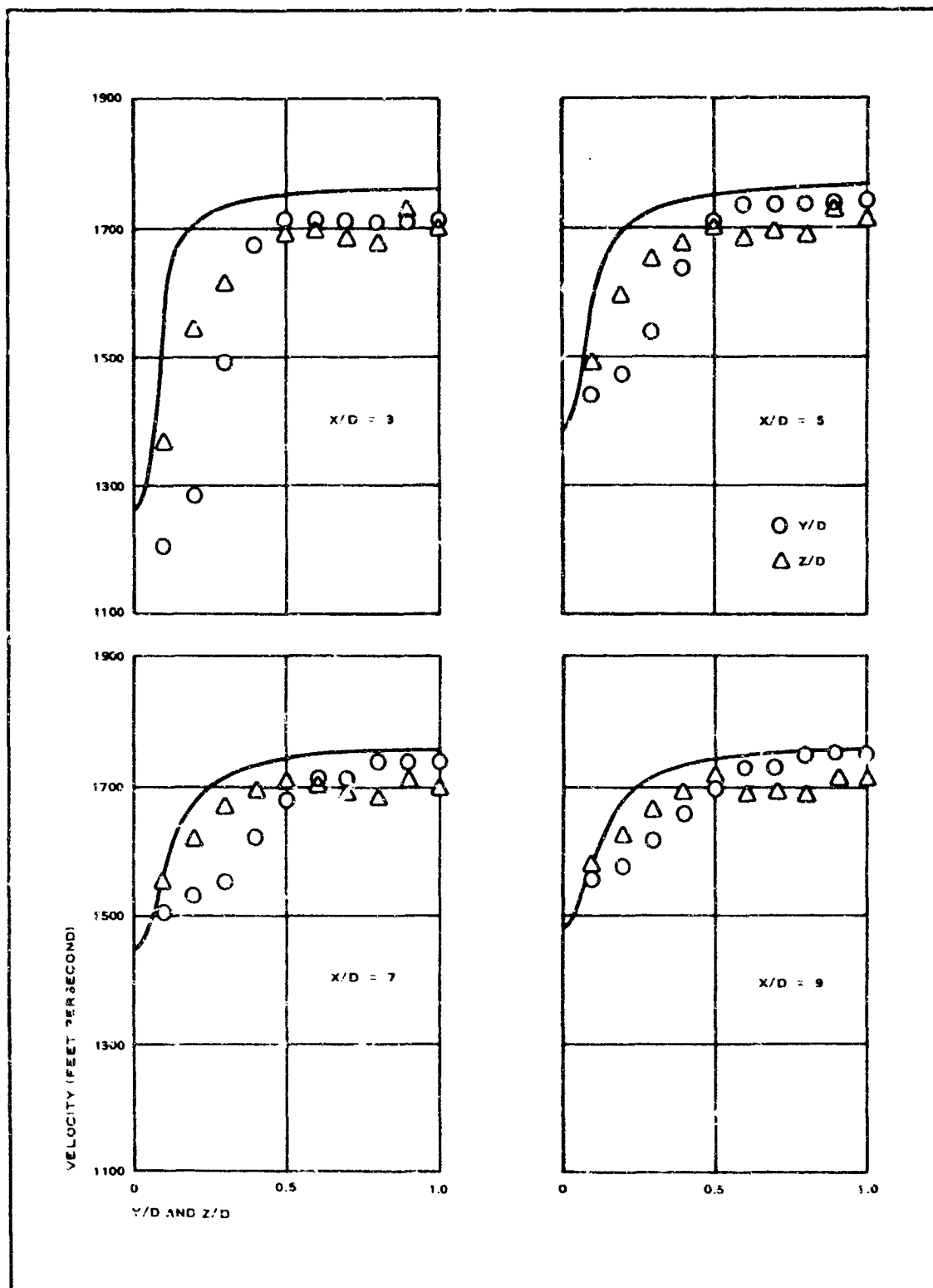
Figure 12 - Comparison of Experimental and Calculated Wake Profiles
$(M_\infty = 2, \ P_{t_\infty} = 19.1 \ psi, \ Model \ 3, \ K = 0.005)$
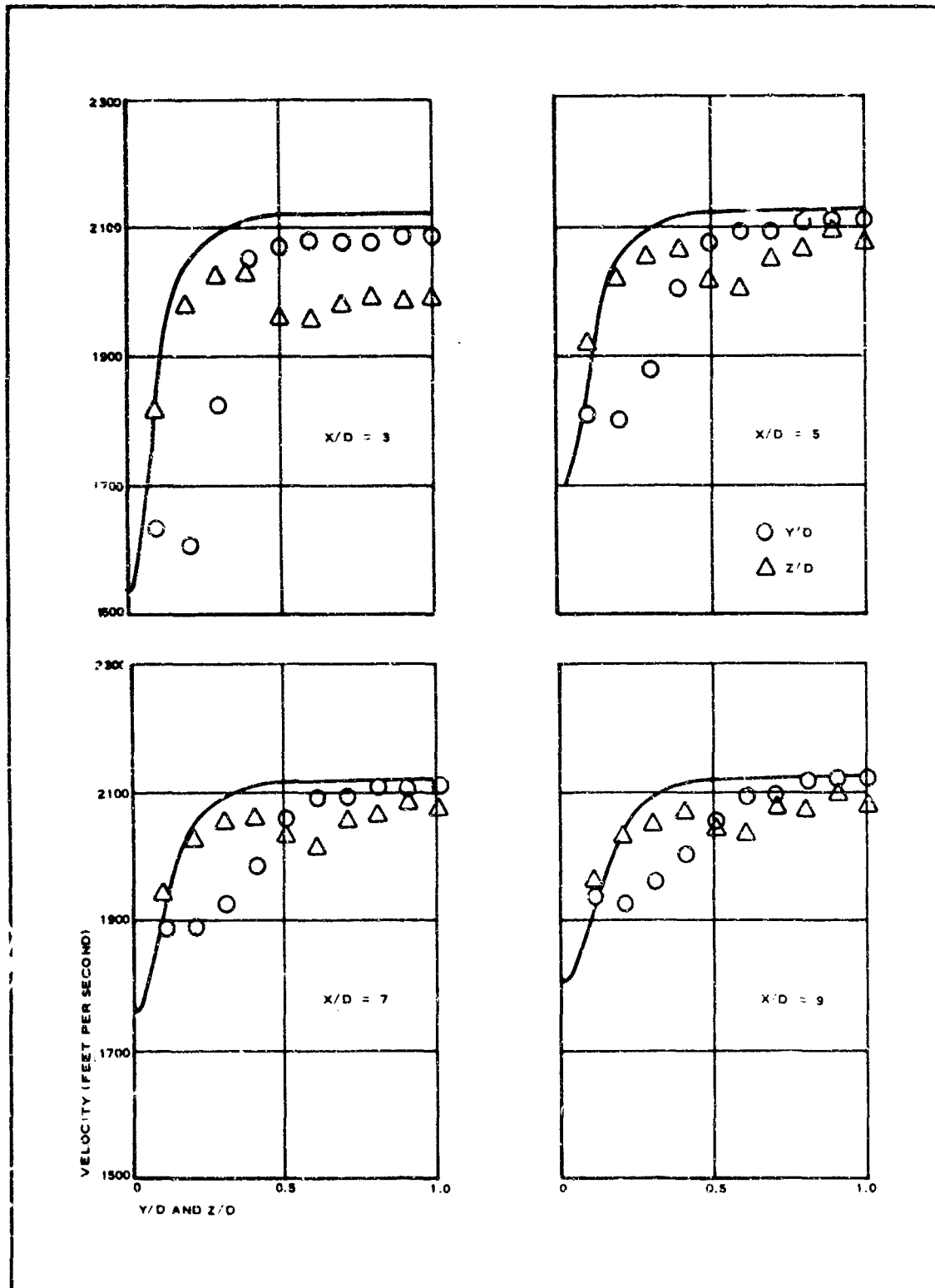
Figure 13 - Comparison of Experimental and Calculated Wake Profiles
$(M_\infty = 3,\ P_{t_\infty} = 43.2\ psi,\ Model\ 3,\ K = 0.005)$
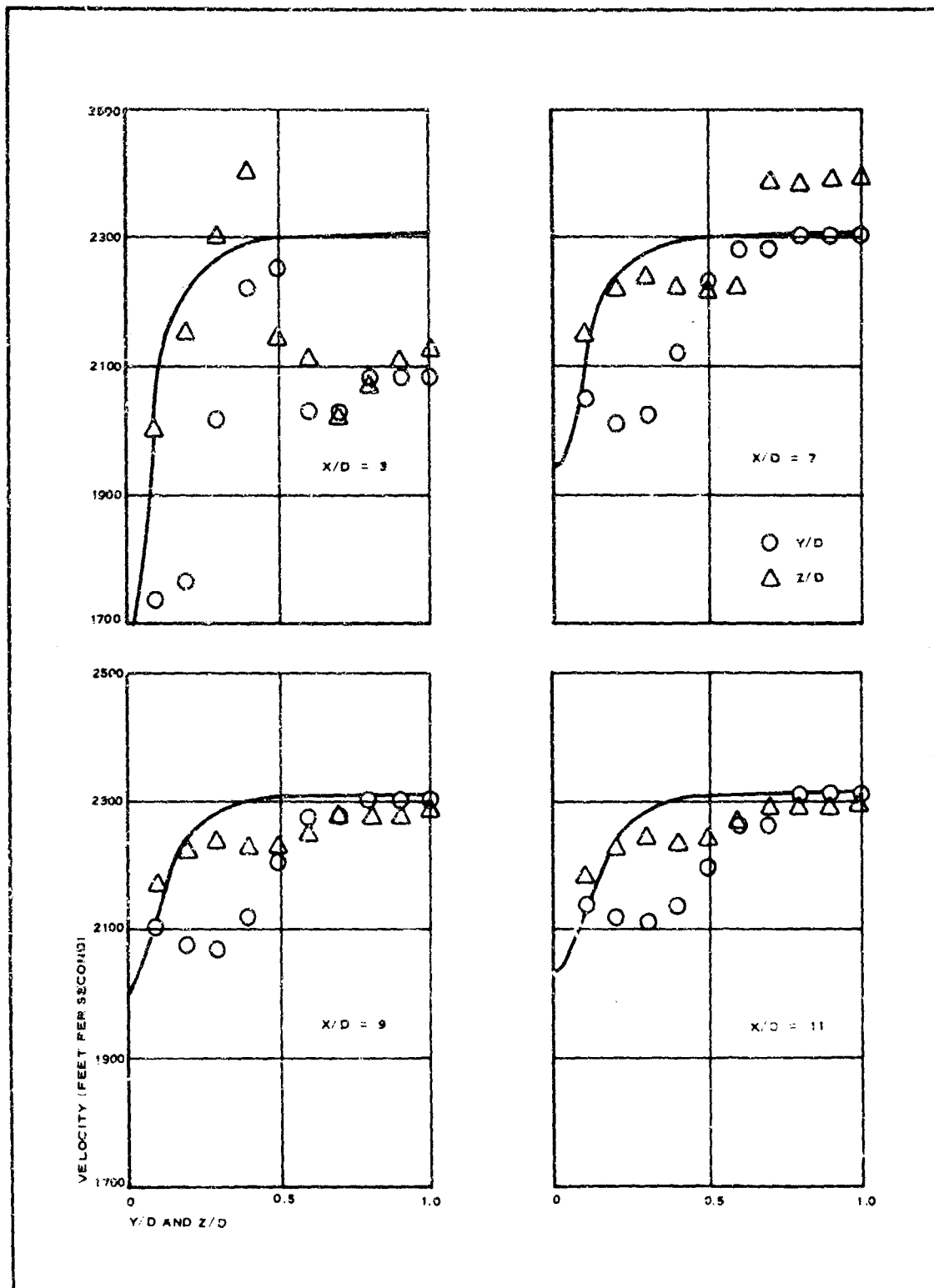
Figure 14 - Comparison of Experimental and Calculated Wake Profiles
($M_\infty = 4$, $P_{t_\infty} = 73.3$ psi, Model 3, K = 0.005)
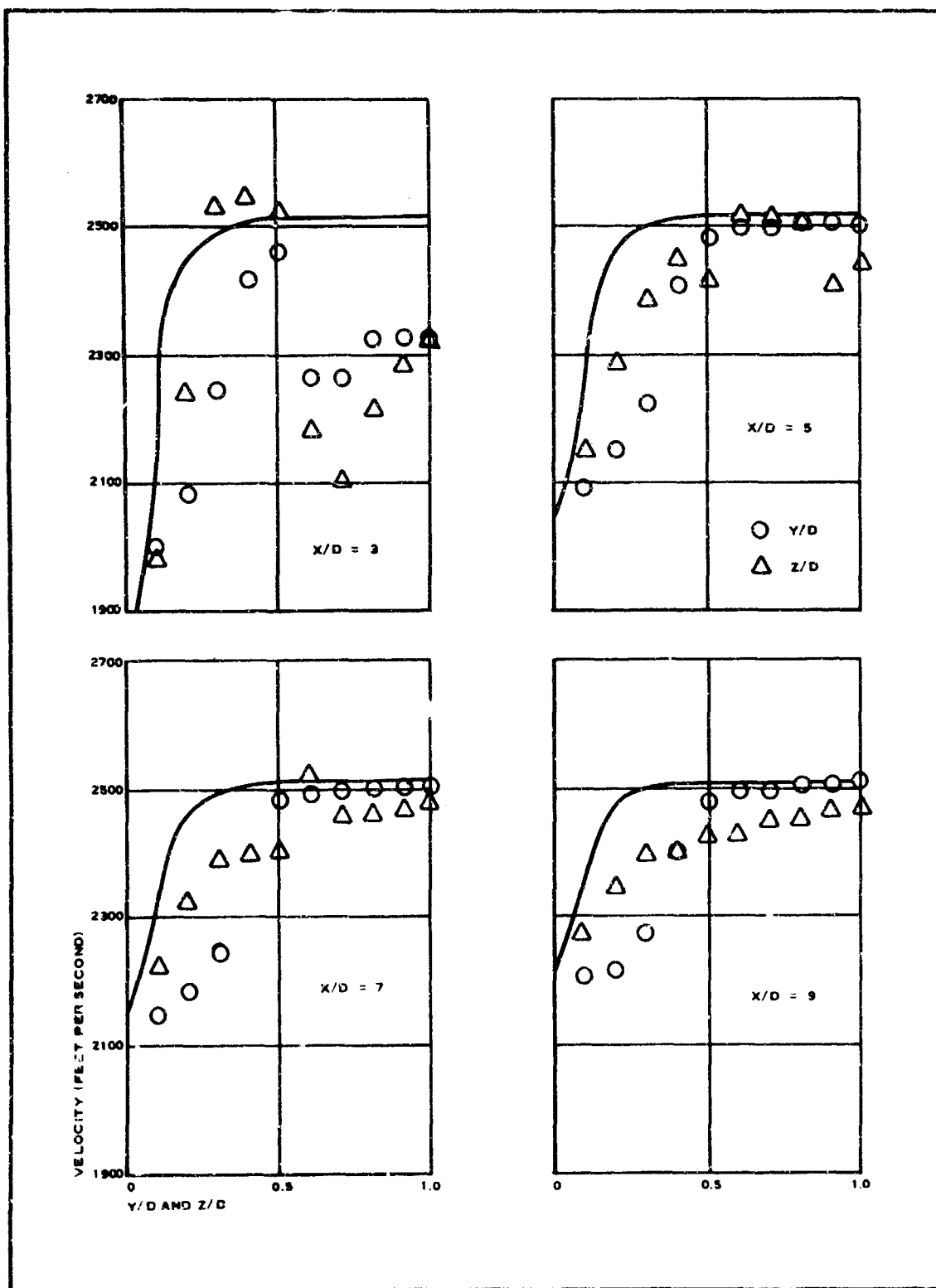
Figure 15 - Comparison of Experimental and Calculated Wake Profiles
$(M_\infty = 5, P_{t_\infty} = 133 p$ Model 3, K = 0.005)
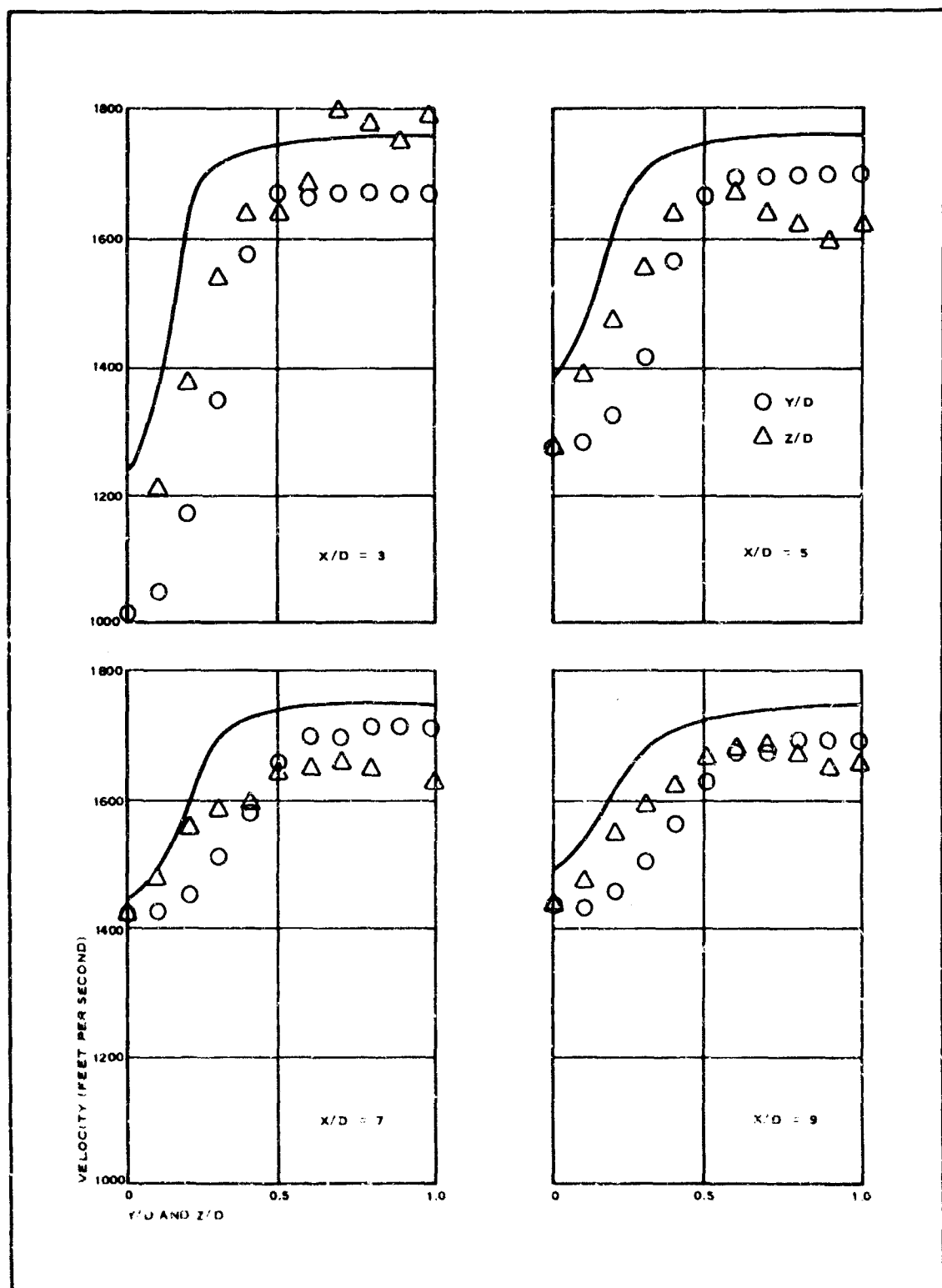
Figure 16 - Comparison of Experimental and Calculated Wake Profiles
$(M_\infty = 2, \ P_{t_\infty} = 2.8 \text{ psi}, \text{ Model 4}, \ K = 0.01)$
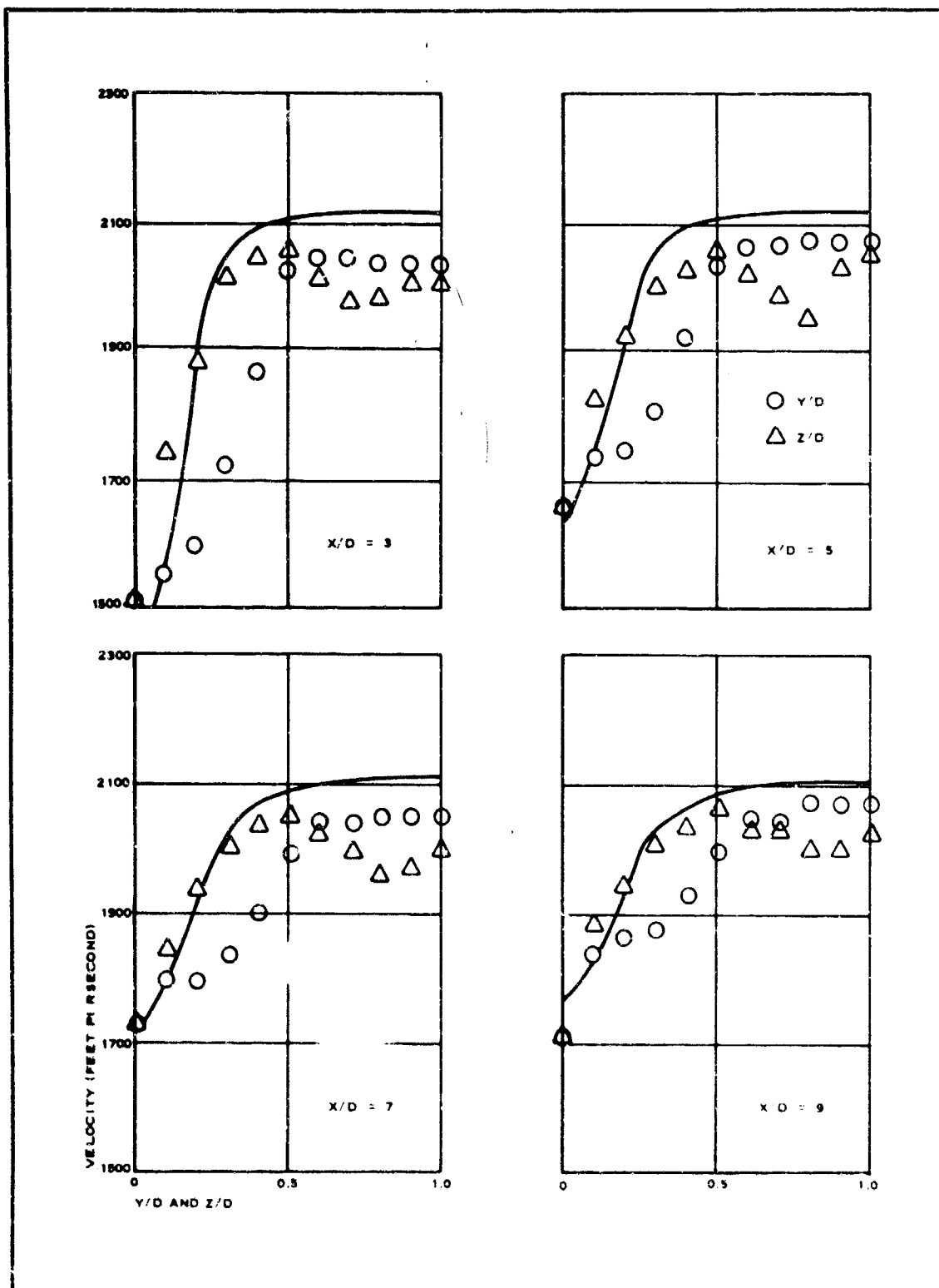
Figure 17 – Comparison of Experimental and Calculated Wake Profiles
($M_\infty = 3$, $P_{t_\infty} = 5.9$ psi, Model 4, $K = 0.01$)
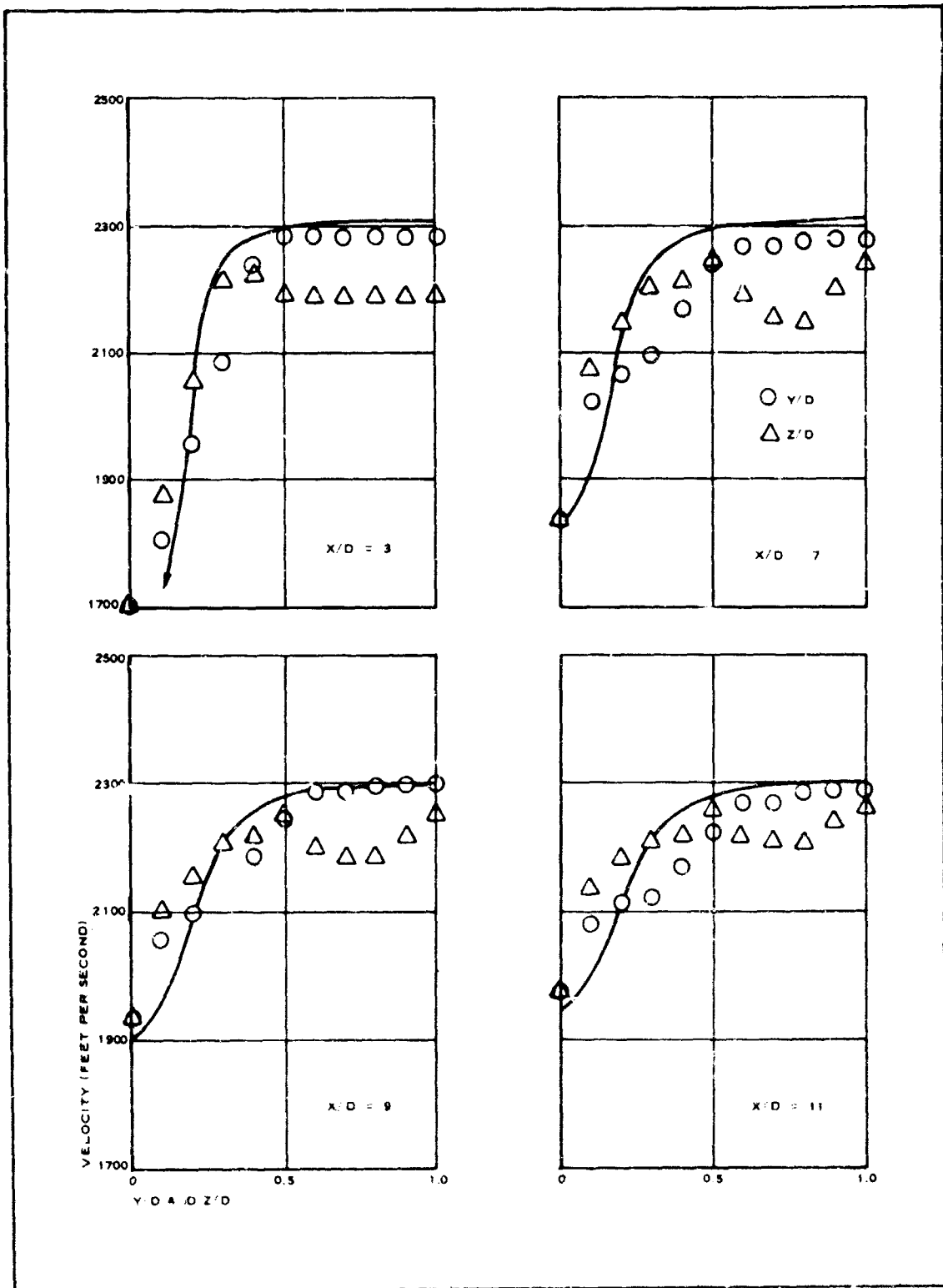
Figure 1ᵃ - Comparison of Experimental and Calculated Wake Profiles
($M_\infty = 4$, $P_{t_\infty} = 13.6$ psi, Model 4, $\kappa = 0.01$)
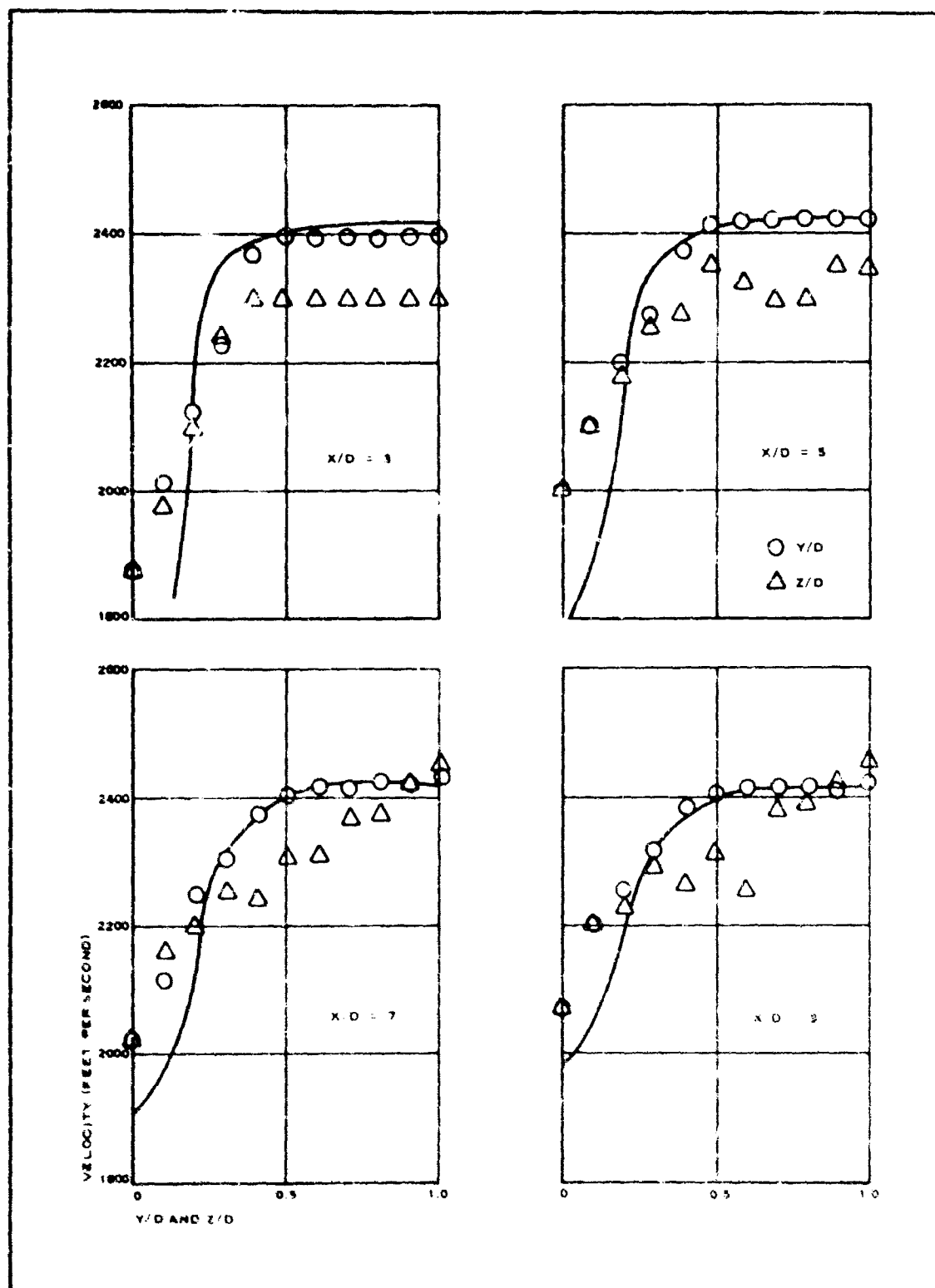
Figure 19 - Comparison of Experimental and Calculated Wake Profiles
(M_∞ = 5, P_{t_∞} = 30.5 psi, Model 4, K = 0.01)
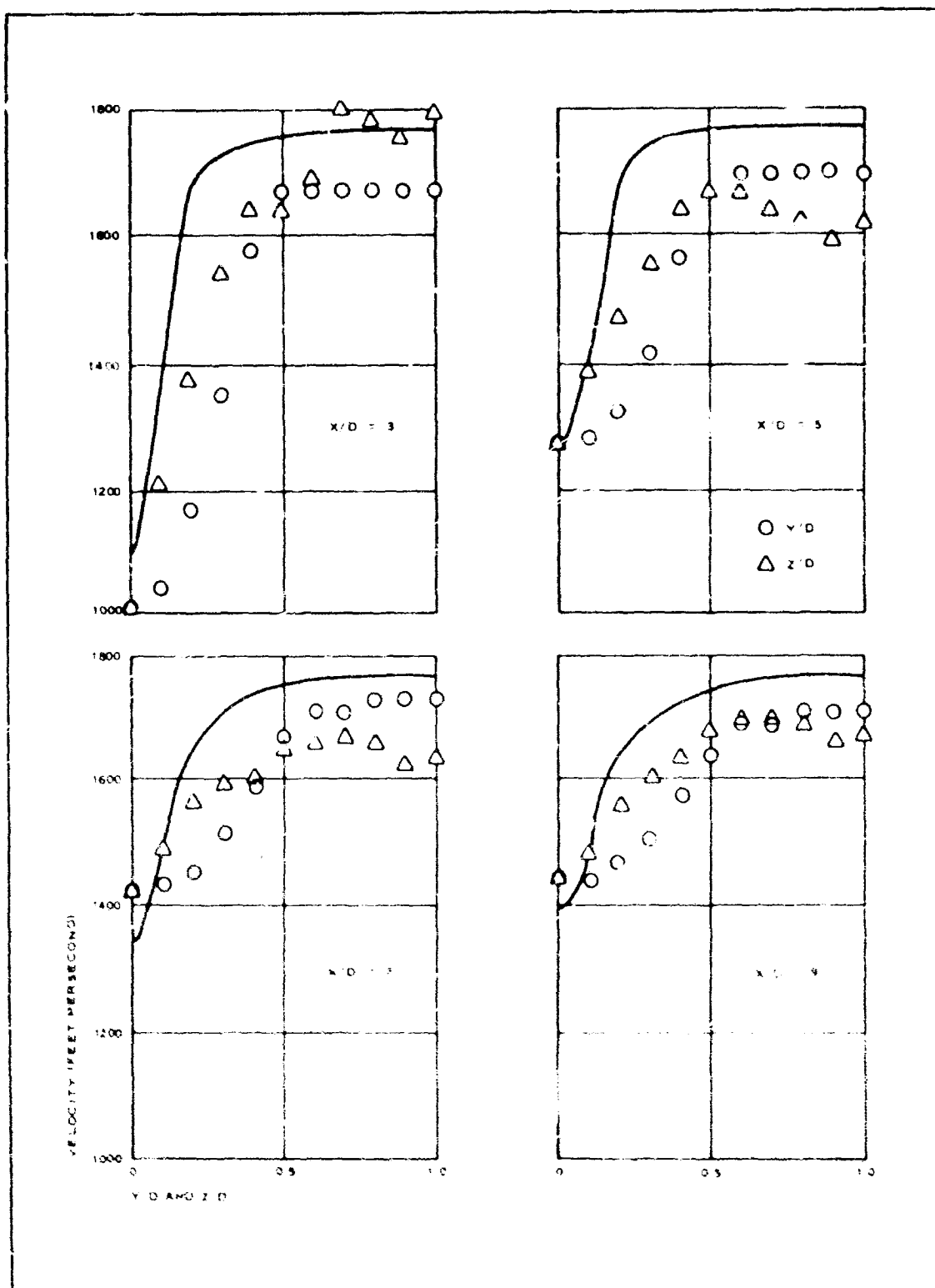
Figure 20 - Comparison of Experimental and Calculated Wake Profiles
($M_\infty = 2$, $P_{t_{(3)}} = 2.8$ psi, Model 4, K = 0.005)
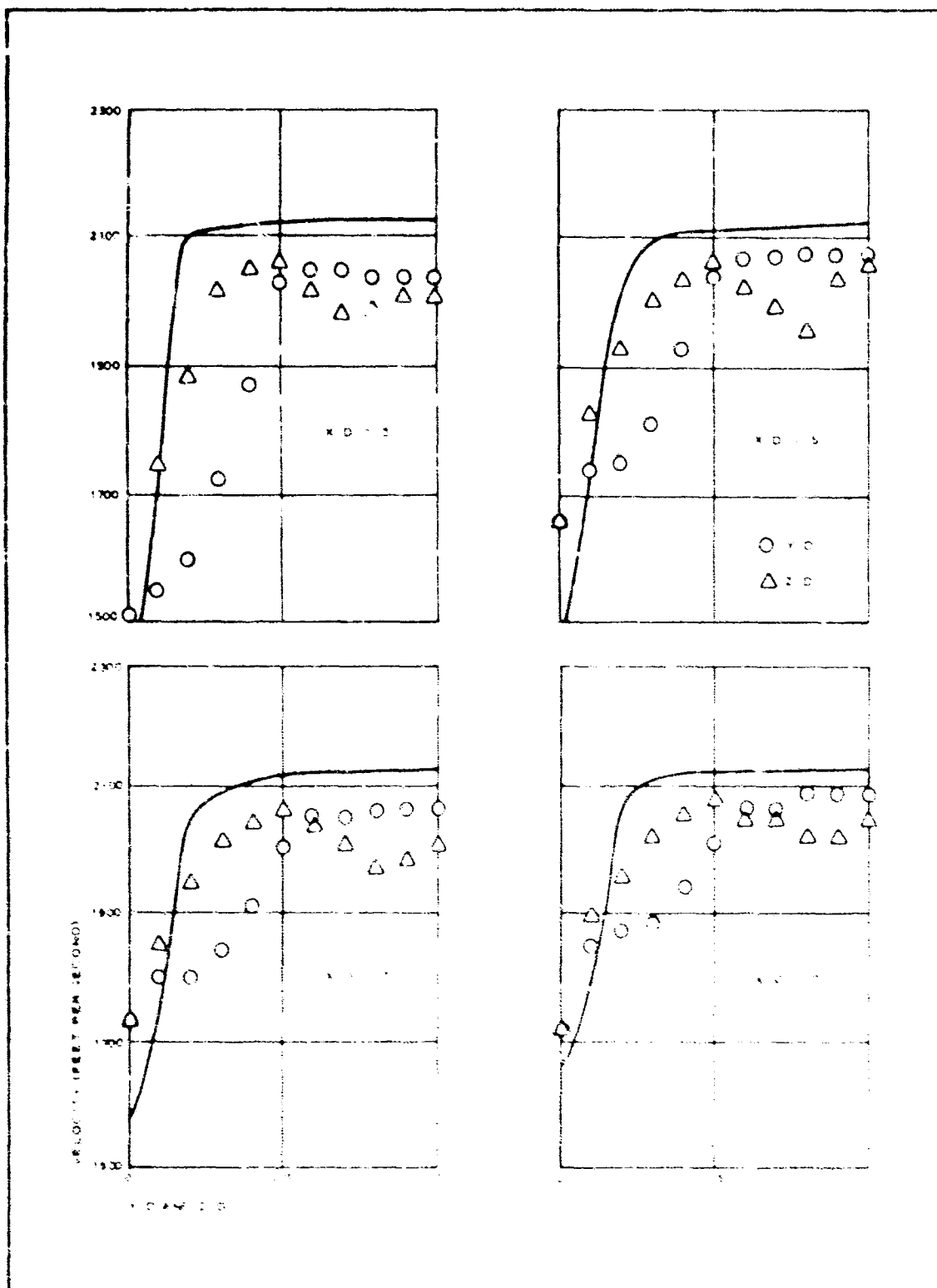
Figure 27 - Comparison of Experimental and Calculated Wake Profiles
(M_D = 3, P_{t_D} = ... , Model 4, h = ...)
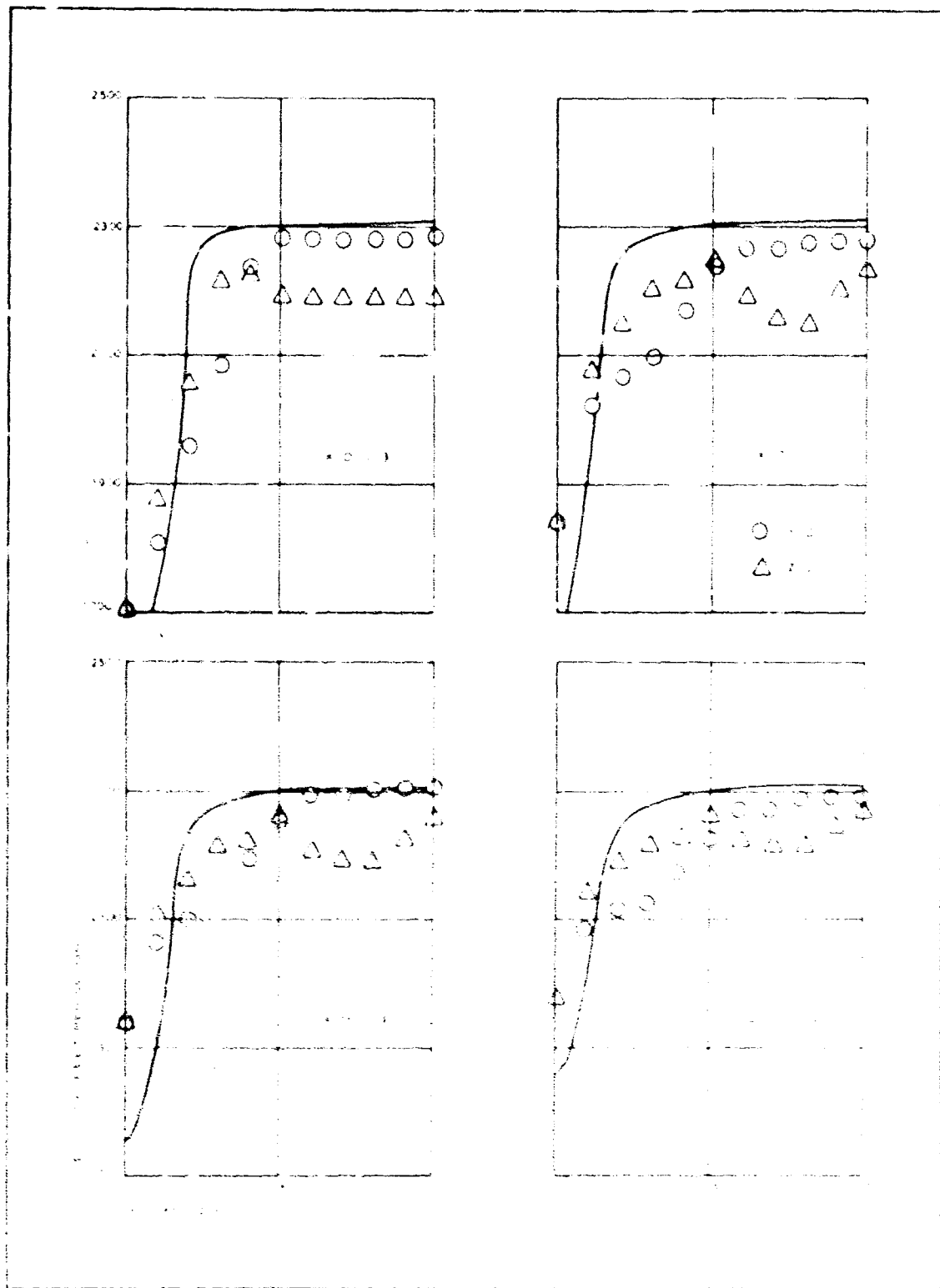
Figure 22. Comparison of ...
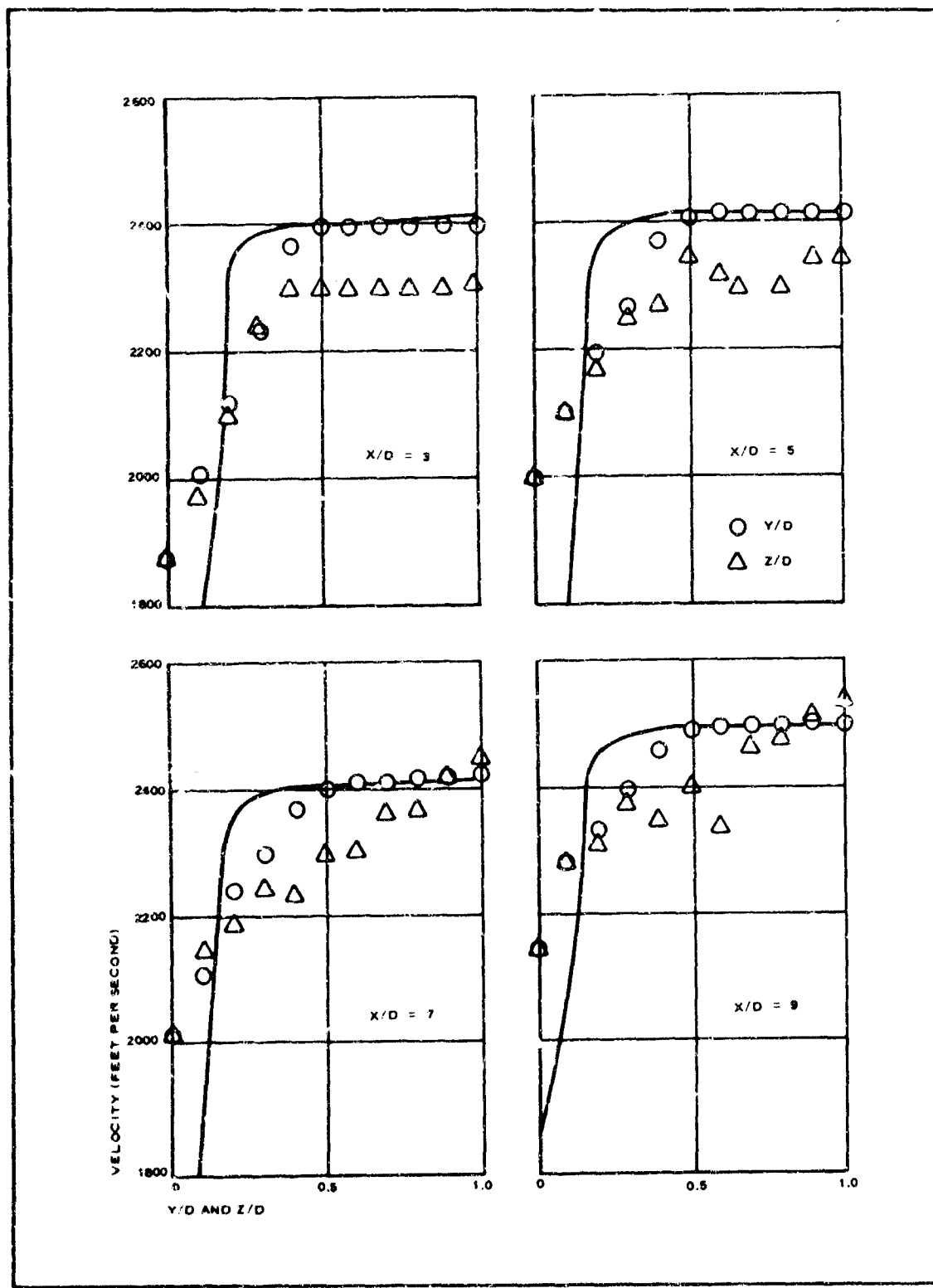
Figure 23 - Comparison of Experimental and Calculated Wake Profiles
($M_\infty = 5$, $P_{t\infty} = 30.5$, Model 4, $K = 0.005$)

the experimental value. As the Mach number is increased, the degree of correlation changes until at $M_\infty = 5$ the theory significantly under-predicts the velocity. This effect is not seen with the choice of the third model. For the same K value, the use of the fourth model will yield a lower centerline velocity than will the third model. The second model for which no data are shown, will result in even higher predicted center-line velocities than the third model. The first model was excluded due to the fact that it deviated from the proper variation of velocity with X/D as exhibited by the other models (see Appendix IV). With each model the choice of the viscosity coefficient K will influence the resultant velocity profile. As K is increased, the velocity predicted by a given model will increase and, as K is decreased, the predicted velocity will decrease.

Prior to the use of the iterated solution, reasonable correlations between experiment and theory were obtained for a value of $K = 0.025$ with the third and fourth models.

d.   Wake Transition

In Items 3, b and 3, c, an integral method for calculating the properties of both laminar and turbulent wakes was presented. However, up to this point no mention has been made of the conditions under which the viscous wake would be laminar or turbulent. Obviously, if the forebody boundary layer is turbulent, then the wake also will be turbulent, and a calculation of the wake profiles as a function of x/D proceeds as described in Item 3, c. However, if the borebody boundary layer is laminar, then the viscous wake may be either laminar or turbulent, depending on whether or not the flow conditions are suitable for transition to occur.

The phenomena of transition in hypersonic wakes has been studied ex-tensively in the laboratory. As pointed out in Reference 14, the correlation of wake transition data that appears to indicate the most physical insight and thus be the most general is that of Pallone, Erdos, and Eckerman. In their work they used a transition Reynolds number based on local properties at the edge of the wake, a velocity equal to that at the edge relative to the centerline velocity, $u_1 - u_o$, and on the wake diameter at transition, $\delta_{D_{TR}}$. The correlation of experimental data that they present is thus in terms of the transition Reynolds number,

$$Re\delta_{D_{TR}} = \frac{\rho_1 u_1}{\mu_1} \delta_{D_{TR}} \left(1 - \frac{u_o}{u_1}\right) \tag{10}$$

and the effective Mach number,

$$\overline{M}_1 = \frac{u_1}{a_1} \left(1 - \frac{u_o}{u_1}\right) . \tag{11}$$

Figure 24 shows a summarization of experimental measurements of wake transition Reynolds number. There is a reasonable correlation of the different experiments and the wake transition may be predicted to within a factor of two in Reynolds number.
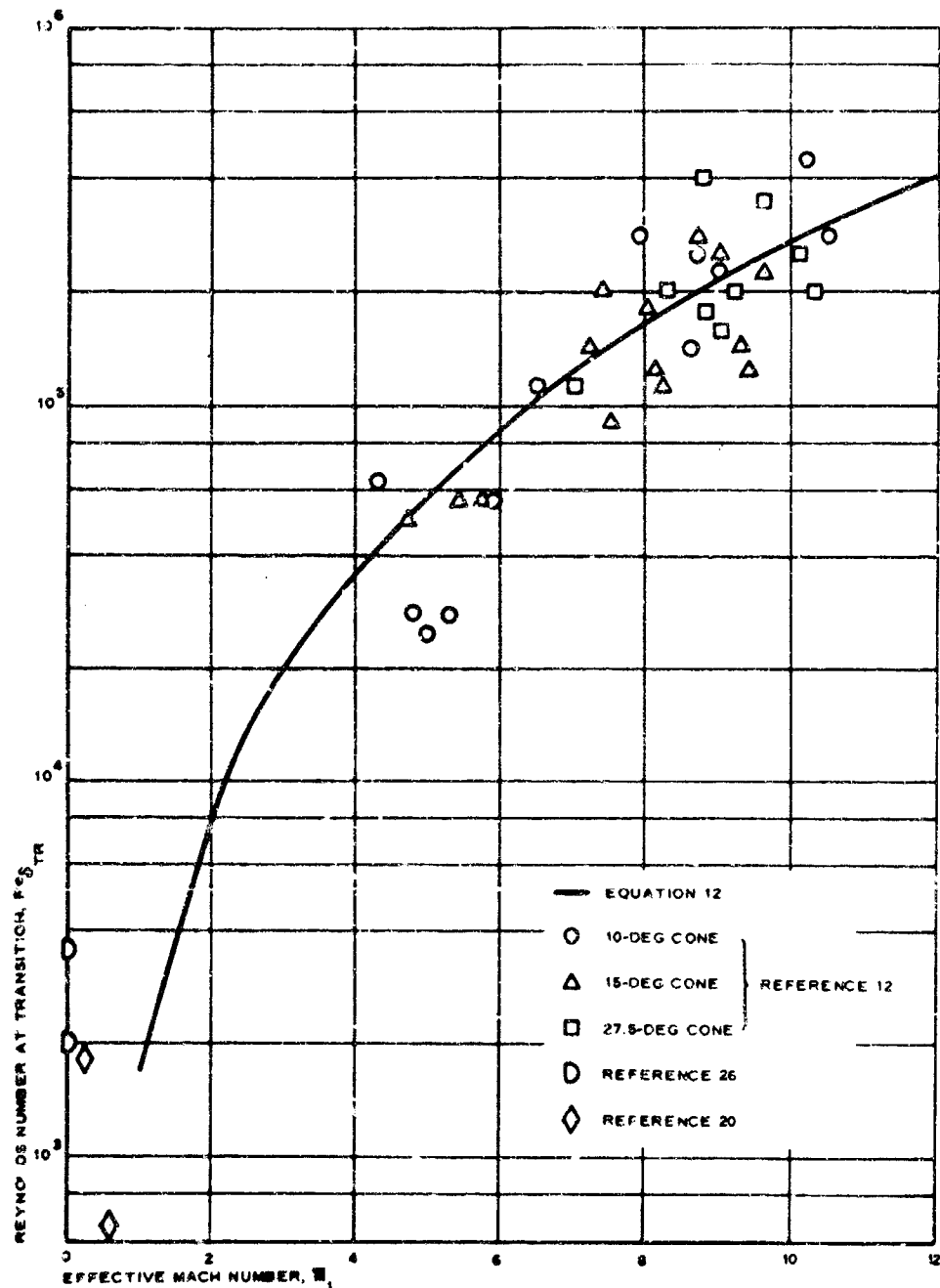
Figure 24 - Experimental Measurements of Wake
Transition Reynolds Number

In order to facilitate calculations using the correlation of Pallone, Erdos, and Eckerman, an approximate curve has been fitted to the data in Figure 24. This approximation is

$$\mathrm{Re}_{\delta_{D_{TR}}} = 1700\,\bar{M}_1^{2.2} \, . \tag{12}$$

This curve also is shown in Figure 24, and reasonable agreement may be see to exist.

In applying Equation 12 to a laminar cylindrical wake, u_0 will be zero due to no-slip condition on the tow cable or riser line. Thus, $\mathrm{Re}_{D_{TR}}$ and $\bar{M}_1$ become a somewhat more conventional "looking" Reynolds number and Mach number based on local edge conditions. Furthermore, for a constant pressure wake region, $\mathrm{Re}_{\delta_{D_{TR}}}$ and $\bar{M}_1$ will not vary with X/D. The viscous wake in the presence of a riser line or tow cable, attaching an aerodynamic decelerator, will be either wholly laminar or wholly turbulent.

e. Near Wake Characteristics

The general characteristics of the near wake were illustrated earlier in Figure 1. This region is made up of the free shear layer, the base region recirculating flow, and the beginnings of the viscous inner wake at the rear stagnation point and on down through the neck; when considered in total, it is a rather complex fluid mechanic phenomena.

As Reeves and Lees have pointed out, and also provided in Reference 15, a relatively clear picture of the structure of the near wake now exists as a result of the many experimental studies that have been reported in the literature (see, for example, Reference 16 through 19). However, theoretically, the state of the art has not progressed as far. As has been pointed out by Webb, et al in Reference 20, the near wake is characterized by two length scales corresponding to the existence of separate regions of high shear and of low velocity. Because of this aspect of the problem, the resulting governing equations are nonsimilar in form and do not reduce to ordinary differential equations when properly transformed. This may be contrasted with the far wake problem in which similar solutions are obtainable.

In order to circumvent this complexity, Lees and Reeves, and later Lees working with Webb and others at TRW Systems (References 20 through 22), have been developing multimoment integral methods of solution for the near wake problem. Weiss in Reference 23, on the other hand, has taken an approach that though inherently more complex offers the hope of a more exact solution of the near wake problem. He obtains a solution by dividing the near wake flow into three regions: (1) a rotational outer flow resulting from the inviscid expansion of the forebody boundary layer at the base, (2) a thin viscous "boundary" layer above the dividing streamline, and (3) the recirculation region itself. The first of these regions is solved for by using the method of characteristics; the second, using a modified Oseen solution of the boundary layer equations; and finally, the third region, by a finite difference

solution to the full Navier-Stokes equations. By coupling these regions together through the matching of boundary conditions at their interfaces and using an iterative method, complete solutions up to the rear stagnation point have been carried out. Although this method has not yet been extended to axisymmetric bodies, it would appear to be the type of approach that could lead to a satisfactory solution of the near wake problem.

For the present investigation, neglecting the near wake details by equating the momentum defect at the base of the forebody to that of the viscous wake downstream of the near wake region appears to be a satisfactory approximation in the development of an engineering solution for the viscous wake characteristics since the free shear layer energy transfer to the recirculation region has been found to be on the order of 10 percent of the total energy transfer from the borebody to the viscous wake. However, even this loss can be accounted for in the solution by use of an empirical constant as will be shown later in this section.

As part of the integral wake solution, it is necessary to specify the location of the rear stagnation point in order to properly relate the wake development to the forebody.

Although the rear stagnation point has been chosen in this instance as the starting point for the viscous wake solution, any other suitable reference location (e.g.) wake neck or sonic point may be used if sufficient data exist to specify its location. Use of the wake neck as the starting point of the solution could yield an improvement in the wake prediction method due to the fact that by starting at the rear stagnation point, the strong gradients in the wake flow are ignored. Further examination of the starting point reference should be considered as future program improvements.

In Figure 25 most of the available data in the literature on the location of the rear stagnation point, x_0, behind bodies at supersonic speeds are shown. Included are data from both two-dimensional and axisymmetric bodies, Mach numbers from 4 through 16, and for a wide range of Reynolds numbers. Also shown is an approximate fit to the data for both the laminar and turbulent flow regimes. As indicated for laminar flow, the rear stagnation point moves closer to the base as the Reynolds number increases. This movement is based obviously on certain allowance for the wide data scatter and even wider discrepancy for a few individual points; the same trend also is noted in Reference 11.

However, this movement is not in agreement with information extracted from available theoretical results. For example, Reeves and Lees predict that the rear stagnation point moves away from the body with increasing Reynolds number for the adiabatic wall case ($h_w = H_1$) and the cold wall case ($h_w = 0.2 H_1$). They further predict that the rear stagnation point will be closer to the body for the cold wall case than for the adiabatic wall case and that this former case will have a very weak Reynolds number dependence. This picture of the near wake perhaps can be reconciled to the data of Figure 25 by noting that the higher data points are in general wind tunnel data (e.g., Reference 17 and 22) and thus correspond more closely to the adiabatic wall case, while the lower data points are in general from ballistic range and shock-tunnel
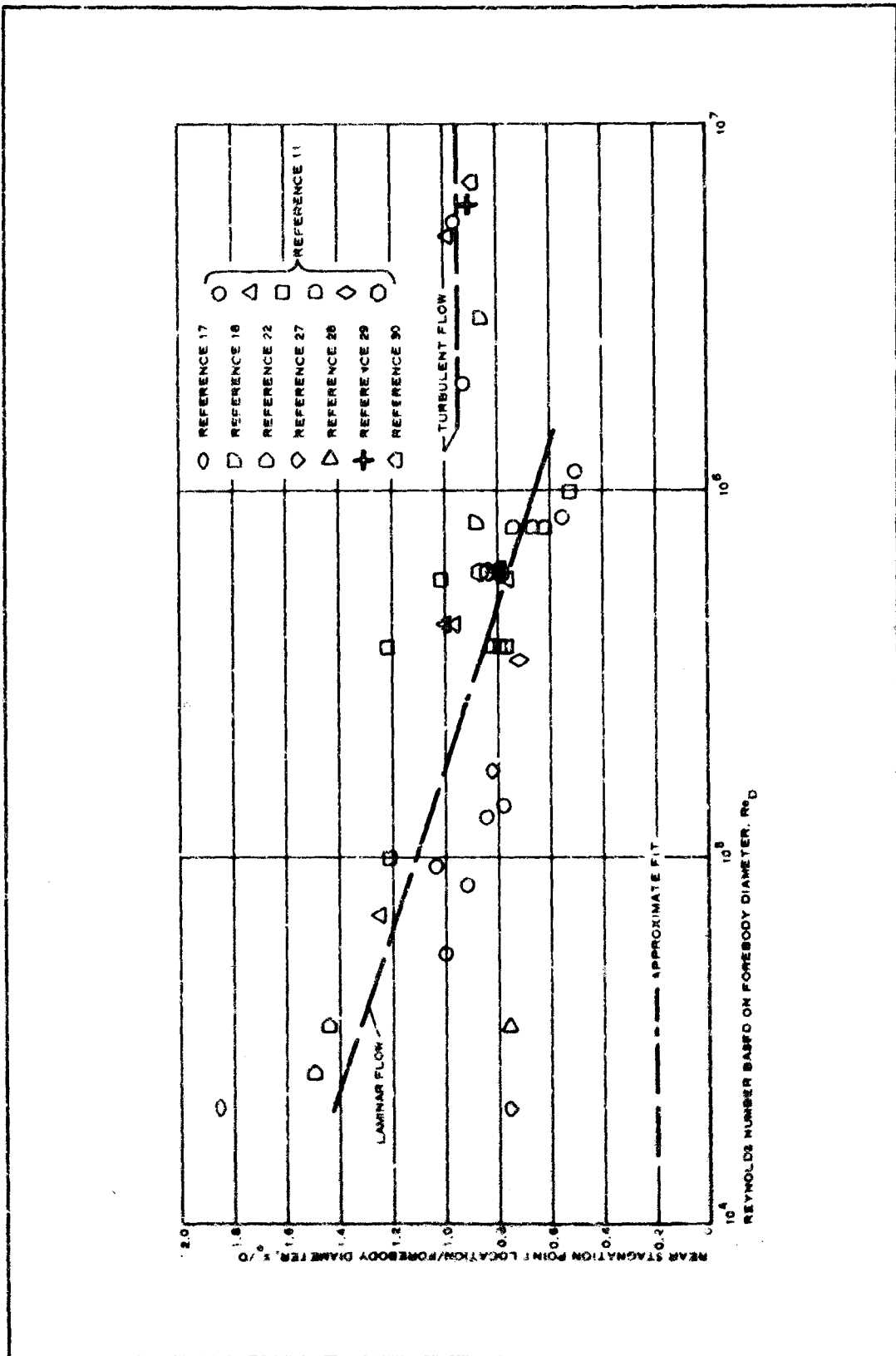
Figure 25 - Experimental Measurements of Rear Stagnation Point Location

experiments and closely approximate the cold wall case. This, however, does not completely explain the discrepancy since the data point from Reference 18 also was obtained in a wind tunnel.

Obviously, the "exact" prediction of the location of the rear stagnation point is more complicated for laminar flow than presented in Figure 25. Still, the approximate fit in Figure 25 should prove useful for engineering calculations. Furthermore, for cylindrical wake calculations, the rear stagnation point location, x_o, is not needed. This is due to the complete similarity in profiles for different X/D stations. Also shown in Figure 25 are measurements of the location of the rear stagnation point at conditions where the boundary layer at the base of the forebody was turbulent. Although there are only a limited number of measurements for this case of turbulent flow, an approximate fit,

$$\frac{x_o}{D} \approx 0.94 \quad , \tag{13}$$

does appear to correlate well with the data. As can be seen, in this case there is no apparent dependence on Reynolds number.

As indicated earlier, it is also of interest to compare the prediction of the rear stagnation point enthalpy with available experimental data. By combining Equations 77 and 80 of Appendix IV, the expression for the rear stagnation point enthalpy is

$$\frac{H_o}{H_1} (\xi = 24) = 1 - (1 - \frac{h_w}{H_1}) \frac{u_B}{u_1} \quad . \tag{14}$$

Equation 14 is based on the equating of the momentum and total enthalpy defects of the wake to the respective quantities of the forebody boundary layer. If it is furthermore assumed that $u_B = u_1$; the simple result then is

$$\frac{H_o (\xi = 24)}{H_1} = \frac{h_w}{H_1} \tag{15}$$

at the rear stagnation point. Equation 15 is compared with available experimental data for laminar flow in Figure 26. The measured values lie slightly higher than that predicted by Equation 15.

In order to correct the present theory such that the predicted rear stagnation point enthalpy will be in agreement with experiment, Equation 4 and Equation 80, Appendix IV, are rewritten as

$$\rho_1 u_1^2 (\pi \theta_1^2) = K_1 \rho_B u_B^2 (\pi \theta_B D)$$

and

$$\rho_1 u_1 H_1 (\pi \theta_{T_1}^2) = K_2 \rho_B u_B H_B (\pi \theta_{T_B} D)$$
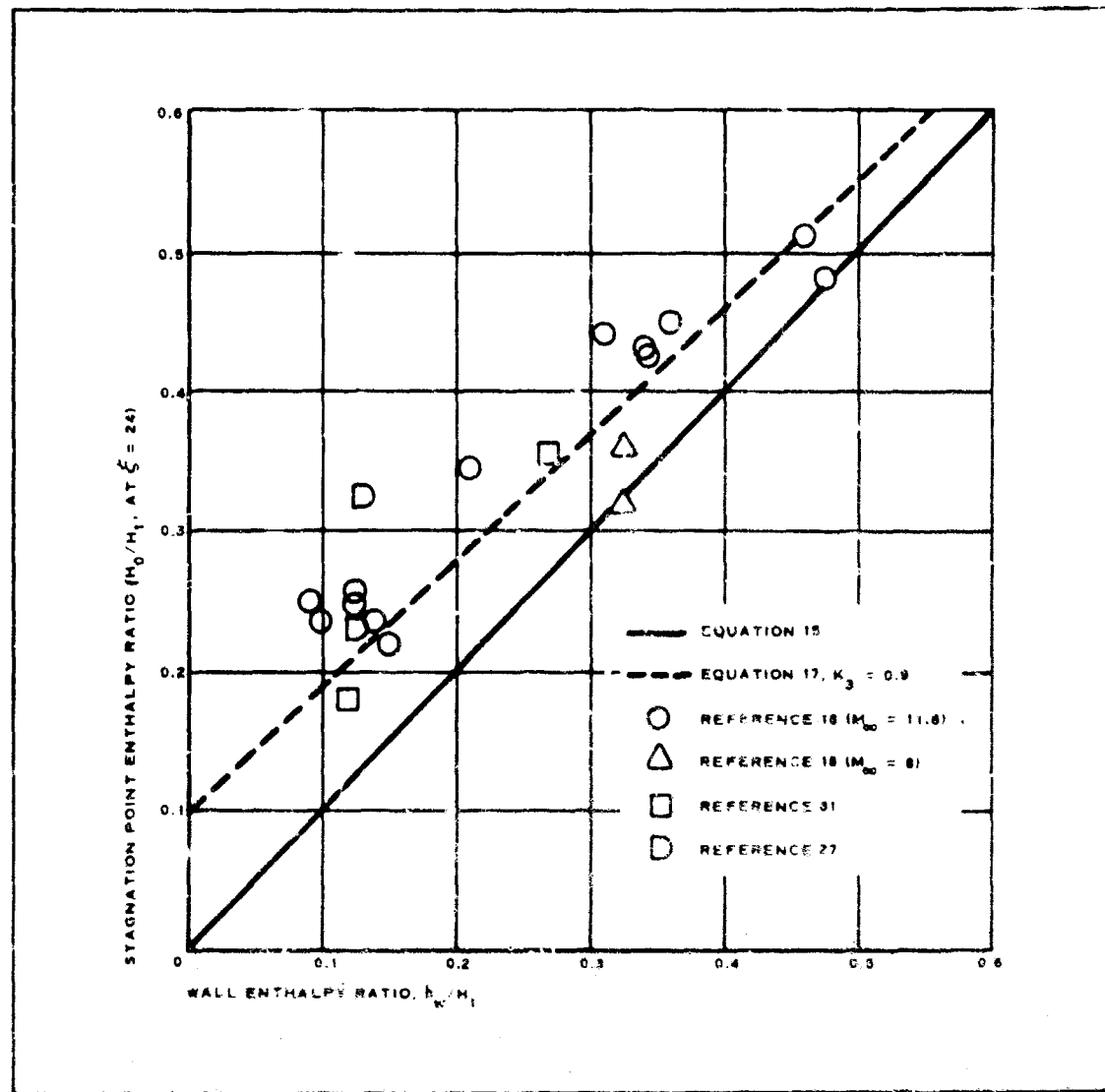
Figure 26 - Experimental Measurements of Rear Stagnation
Point Enthalpy for Laminar Wake Flow

Here, K_1 and K_2 are constants that would be expected to be greater than
or equal to one since they are representative of the fractional increase
in the momentum and energy defects due to the transport of these quanti-
ties across the dividing streamline. Combining the above two equations
with Equation 79, it follows that

$$\frac{\theta_T^2}{\theta_1^2} = \frac{K_2}{K_1} \left(1 - \frac{h_w}{H_1}\right) \cdot \frac{u_1}{u_b} \tag{16}$$

This may be substituted into Equation 77 with the result that

45

$$\frac{H_o \ (\xi = 24)}{H_1} = 1 - K_3 \ (1 - \frac{h_v}{H_1}) \qquad (17)$$

where $K_3 = K_2 u_1 / K_1 u_B$.

Equation 17 has been approximately fitted to the laminar experimental data using a value of $K_3 = 0.9$ and is shown in Figure 26. Although this value of K_3 is strictly based on experiment and has no real theoretical basis, its use in Equation 17 for laminar wake calculations should prove useful.

For turbulent near wake flow, there is only a smattering of data that may be found in the literature. These limited number of data points, however, are compared with Equations 15 and 17 for both $K_3 = 0.9$ and $K_3 = 0.65$, in Figure 27. The latter value of K_3 does give agreement with the data. The limited amount of data prevents any real recommendation for the use of $K_3 = 0.65$ for turbulent wake calculations, and it is obvious that more data and more comparisons of data with theory are necessary before any degree of confidence can be placed in Equation 17 and on the use of an effective K_3 for either laminar or turbulent flow. In Appendix IV where a method for viscous wake calculations is outlined, the constant K_3 is left as an input.

As was noted in Item 3, the present integral theory would not be expected to give accurate results in the near wake region. Thus, the lack of
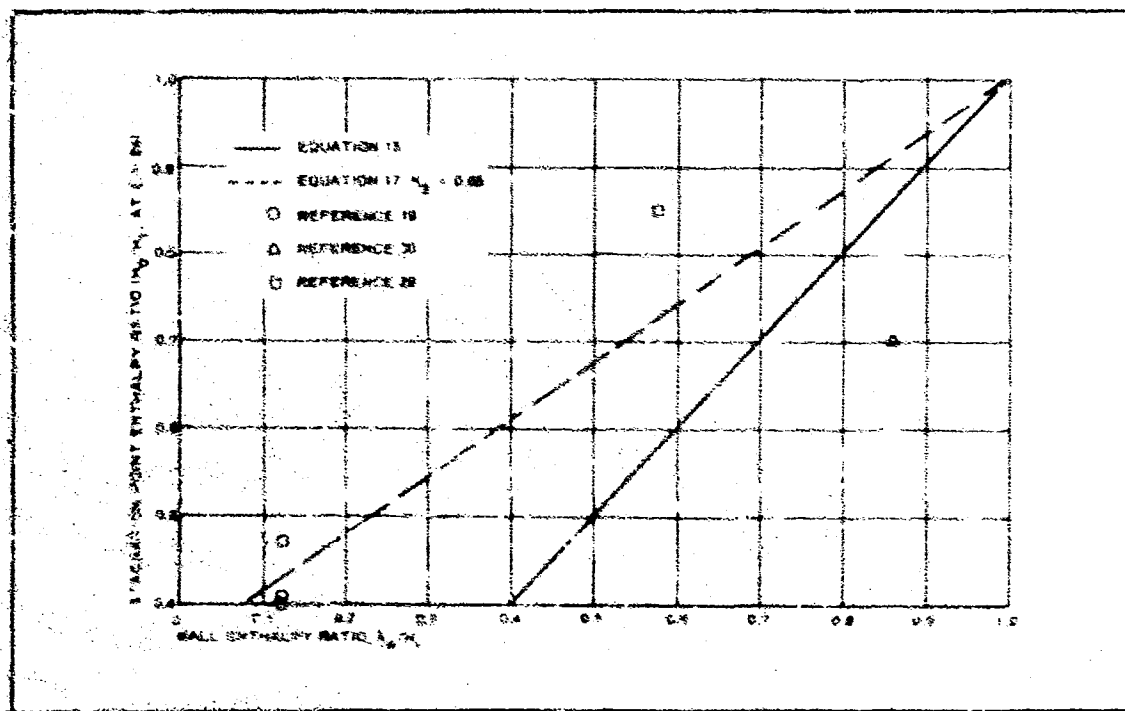

Figure 27 - Experimental Measurements of Rear Stagnation Point Enthalpy for Turbulent Wake Flow

agreement in Figures 26 and 27 is not surprising, and the introduction
of an empirical constant, K_3, into Equation 17 only represents an attempt
to improve the accuracy of the present solution in a region where it other-
wise would not be expected to hold. However, in spite of the failings of
the present method in predicting the rear stagnation point enthalpy, com-
parisons with experimental data have shown that in the prediction of neck
diameter for a laminar wake the method in Item 3, b of this section is
quite satisfactory.

Before leaving this discussion of the near wake, one last comment
should be made with regard to the nature of the flow. It has been found
experimentally that the near wake is very sensitive to the base geometry
of the vehicle and also to the injection of any fluid at the base into the
near wake. This latter effect is obviously of concern in wind tunnel ex-
periments where instrumentation may be supported from the base of the
forebody. However, it also opens up the possibility of somewhat control-
ling the wake characteristics of a vehicle through fluid injection. It is
also of interest in the decelerator problem where due to the manner of
decelerator deployment the problem of interest may in fact be one in
which there is fluid injection.

In Reference 24 Bauer presents measurements that show a 50-percent
change in the location of the rear stagnation point due to a nitrogen in-
jection mass flow rate that is only 2 percent of that of the free stream
based on base area of the forebody. Furthermore, in Reference 25
Bauer shows that a 3-percent injection rate using helium causes the
wake recompression shock to completely disappear.

This sensitivity of the near wake to almost any external influence casts
doubt on the applicability of any wake data obtained under conditions
where components of the model support system, e.g., struts, wires, or
a sting, interfere with the flow. Thus, future efforts should include
wind tunnel studies where such interference effects are not present.

4. INVISCID WAKE ANALYSIS

a. Inviscid Wake Characteristics

In order to fully describe the trailing wake behind a supersonic body,
both the viscous inner wake and inviscid outer wake characteristics,
e.g., velocity, density, and temperature profiles, must be known. The
calculation of the viscous inner wake depends on the forebody boundary
layer, and methods for handling both of these types of fluid mechanic
phenomena have been previously described for both laminar and turbu-
lent flow and including transition. The inviscid outer wake characteris-
tics, on the other hand, depend on forebody bow shock wave strength and
shape and the subsequent expansion over the aft portion of the body.

b. Analysis

For the purpose of analysis, the wake of a supersonic vehicle is consi-
dered where it is assumed that the vehicle bow shock wave shape and
the pressure distribution along the wake axis is known from either ex-
periment or theory. For blunt bodies at hypersonic speeds, blast wave

theory may be used to approximate both the bow shock shape and the pressure distribution on the wake axis. For supersonic speeds, however, the pressure in the wake may be approximated as being equal to P_∞, the free stream pressure.

From conservation of mass, a mass balance may be written that relates the mass flow in the free stream at the shock through a disk of radius R_s with the mass flow in the inviscid wake through a disk region of radius r. This relation is

$$\rho_\infty V_\infty \pi R_s^2 = 2\pi \int_{\delta^*}^r \rho u r dr \quad . \tag{18}$$

The integration on the right-hand side of Equation 18 starts at δ^*, the wake displacement thickness instead of zero in order to account for the displacing of streamlines by the viscous wake phenomena. The wake displacement thickness is defined by the relation

$$\rho_i u_1 \delta^{*2} \pi = 2\pi \int_0^\delta (\rho_1 u_1 - \rho u) r dr \tag{19}$$

and may be determined using the viscous wake results.

Equation 18 may be considered to be a relation between properties on a streamline passing through a point on the bow shock at a shock radius R_s and properties on the same streamline downstream of the body at a point A, a distance r from the axis of the wake. With the bow shock shape known, then a specific value of R_s corresponds to specific properties immediately behind the bow shock for the streamline passing through that point. If it is assumed that the flow is isentropic in expanding from the shock wave on downstream to point A, then Equation 18 is a relation between two points with the same entropy, or, in other words, the same total pressure. The assumption of isentropic flow behind the bow shock means that any secondary shocks (i.e., wake recompression shock and forebody flare shock) produce negligible changes in entropy. Although this assumption is possibly open to question, it simplifies the calculation of the inviscid wake properties and is in line with the other assumptions employed.

Equation 18 thus provides a means for calculating the total pressure or entropy at point A, a distance r from the wake axis. Furthermore, the total enthalpy is known since the inviscid flow may be considered adiabatic. Finally, with the pressure distribution along the axis of the wake known, an estimate of the static pressure in the inviscid wake can be made by assuming that there are no pressure gradients radially in the wake region i.e., dp/dr = 0. The complete state of the gas at a point A in the inviscid wake thus is completely specified in terms of the total pressure, the total enthalpy, and the static pressure. In order to facilitate calculations using the above analysis, the following transformation is introduced:

$$\mathrm{urdr} = \rho_\infty V_\infty \mathrm{ndn} \quad , \tag{20}$$

and

$$x_1 = x \quad .$$

Equation 18 then may be rewritten as

$$\rho_\infty V_\infty \pi R_s^2 = 2\pi \int_{\delta_n^*}^{n} V \, \mathrm{ndn} \quad ,$$

or

$$R_s^2 = n^2 - (\delta_n^*)^2 \quad , \tag{21}$$

where δ_n^* is the transformed displacement thickness, and

$$\rho_1 u_1 (\delta^*)^2 \quad \rho_\infty V_\infty (\delta_n^*)^2 \quad . \tag{22}$$

Thus, from Equations 21 and 22 and assuming δ^* known from an analysis of the viscous wake, the entropy and total pressure at a point A, lying a distance n from the axis in the transformed plane, may be determined as being equal to that immediately behind the bow shock wave at a radius R_s. With the total pressure or entropy known for the streamline, and with an estimate of the static pressure, the local Mach number at point A may be determined. This, together with the total enthalpy, gives the static enthalpy or temperature. The complete state of the gas, including the velocity and density, at such a point is thus specified, and the variation in fluid properties in the transformed (n, x_1) plane may thus be determined. In order to transform the results back into the (X, r) plane, Equation 20 may be used with the result that r and n are related by the equation,

$$\int_{\delta^*}^{r} \mathrm{rdr} = \int_{\delta_n^*}^{n} \frac{\rho_\infty V_\infty}{\rho u} \mathrm{ndn} \quad . \tag{23}$$

Since $\rho_\infty V_\infty / \rho u$ is known as a function of n, this calculation may be readily carried out using numerical techniques for the integration. The variation of such fluid properties as velocity, Mach number, and temperature thus may be calculated as a function of r, the radial distance from the axis of symmetry.

Using this inviscid wake prediction method with the shock shape as determined from wind tunnel tests of an Arapahc C with nose cone forebody as an input, a good correlation between theory and experimental results has been obtained. Figures 8 through 23 show both the experimental

velocity data points obtained by reducing the measured pressure data
and the inviscid wake theoretical predictions for Mach numbers of 2, 3,
4, and 5 for two Reynolds number conditions and for X/D values between
3 and 11. The starting point for the inviscid wake prediction is noted
in the figures, and in all instances the theory is within 10 percent of the
experimental values. Thus, the degree of correlation is certainly ac-
ceptable for engineering calculations.

The accuracy of the inviscid wake theory will be limited to some extent
by the accuracy of the inputted shock shape. In performing the mass flow
balance, theory does not consider the embedded shock produced by the
forebody flare or the recompression shock wave formed in the wake neck
region due to the added complexity required to include those considera-
tions.

Although there is some data scatter and also some difference between
Y/D plane experimental values and the Z/D plane experimental values
due in part to the fact that the Z/D values were measured in the plane
of the strut, the extent of the correlation between theory and experiment
is sufficient for engineering calculations in the wake. The accuracy of
the correlation improves for larger values of X/D. In the region of
X/D = 3 that is quite near the wake neck and the recompression wake
shock, the wake prediction method, while still adequate, is less accurate.

5. ITERATIVE WAKE SOLUTION

In order to completely describe the characteristics of the viscous and
inviscid wake, an iterative solution was performed to compute the viscous
wake profiles. This was done in order to obtain continuous profiles of
the wake properties across the total wake (viscous + inviscid) since the
viscous wake edge conditions were originally calculated based on the flow
through the normal portion of the bow shock wave (as per boundary layer
analysis) and did not match the edge value obtained from the mass flow
balance performed in the inviscid wake.

The iteration procedure, which has been programmed, computes the
viscous wake properties based on a revised value of Mach number, M_1,
at the edge of the viscous wake. The revised value of M_1 is obtained
from the mass flow balance performed in the inviscid wake analysis and
is that value of M_1 predicted by the mass flow balance corresponding to
the edge location predicted by the initial viscous wake run. This new M_1
value is used as an input for a second pass (first iteration) through the
viscous wake program and the inviscid wake program. Although the
above procedure could be repeated an indefinite number of times, initial
results have shown that no more than three iterations are necessary to
obtain complete matching of the viscous wake-inviscid wake edge.

The results based on this iterative solution are shown in Figures 8
through 23. The best correlation for these turbulent viscous wake cases
were obtained using Model 3 with a viscosity coefficient equal to 0.005.
A correlation for laminar viscous wake has not been made using the
iterative solution. This value of K = 0.005 is below the range of values
(0.02 to 0.06) indicated in the literature as shown in Item 3, c. However,
those values were obtained from standard boundary layer type solutions.

By performing the iteration solution that changes the consideration of the flow through the normal shock as in standard boundary layer theory to flow through a locally oblique shock as used on this program, the value of K yielding a satisfactory correlation has been changed. Prior to the use of the iterative solution with the viscous wake, reasonable correlations between experiment and theory were obtained for values of $K = 0.025$ with Models 3 and/or 4. Until more experimental data become available on the effects of other parameters (such as the wake neck as a starting point rather than rear stagnation point mentioned in Item 3, e of this section, on the results of the predictive method, an acceptable range of K values cannot be exactly determined. Thus, it is believed that the current use of $K = 0.005$ with the iterated solution is acceptable as an engineering solution insofar as achieving and maintaining a general theoretical approach to the wake description.

6. **FLOW FIELD COMPUTER PROGRAM**

An integrated computer program has been developed and programmed in FORTRAN IV for use on the IBM 360-40 and IBM 7094 computers. The program is based on the forebody program of Section II and the wake analyses of Section III.

The computer program can determine the properties of the inviscid and viscous wake preceding a decelerator and consists of the following sub-programs:

1. Forebody flow field (M_L, T_L, and P_{T_L})

2. Boundary layer, laminar and turbulent (θ, M^*)

3. Viscous wake, laminar and turbulent (M_L, P_L, and T_L)

4. Inviscid wake (M_L, P_L, and T_L)

5. Iteration (on Items 3 and 4 above)

The following inputs must be specified to utilize the integrated program:

1. Free stream conditions

2. Forebody geometry and wall temperature

3. Bow shock shape

4. Boundary layer constant, K (0 or 1)

5. Wake constants, K and K_3

6. Number of iterations to be performed

Optional inputs (which will be calculated in the program if not specified) include:

1. Boundary layer transition Reynolds number or transition point location

2. Forebody flow field (M_L, P_L, and P_{T_L})

Copies of this computer program may be obtained from AFFDL(FDFR), WPAFB, Ohio 45433 by request.

SECTION IV

PARASONIC PARACHUTE PERFORMANCE

1. PERFORMANCE FACTORS

The performance of PARASONIC parachutes is described according to two basic criteria: drag and stability. The primary factors that influence the performance are listed below.

1. Canopy shape

2. Canopy porosity

3. Free stream Mach number

4. Free stream Reynolds number

5. Forebody shape

6. Downstream location of the canopy inlet (X/D)

7. Ratio of canopy area to forebody base area (A_c/A_b)

The first two parameters, canopy shape and porosity, were held constant in this performance evaluation. All parachute testing was conducted with PARASONIC parachutes, thereby constraining the canopy shape. The selection of PARASONIC parachutes was made based on the high degree of inflation stability and structural integrity exhibited by these parachutes. The PARASONIC parachutes are members of the Hyperflo family of supersonic parachutes and are distinguished from standard Hyperflo parachutes by comparison of canopy profiles. The PARASONIC parachutes are constructed with an uninflated shape which approximates the fully inflated shape of a standard Hyperflo parachute (see Figure 28). When inflated, the PARASONIC canopy is free from excess material, thereby reducing "flagging" loads which have been found to lead to premature canopy failure. The porosity was held constant for all parachutes to further limit the number of variables.

An experimental test program was conducted to determine the effects of the remaining parameters on the PARASONIC parachute performance. The analysis of the effects of these parameters is presented herein. The experimental test program is discussed in detail in Appendix V.

2. WIND-TUNNEL TEST SUMMARY

The PARASONIC parachutes described above were deployed behind the three forebody configurations shown in Figure 29. The basic Arapaho C forebody is a 0.182-scale model of the Arapaho C free-flight test vehicle and consists of a probe nose; a cylindrical centerbody; and a symmetrical, flared afterbody. The Arapaho C with nose cone forebody has a centerbody and afterbody identical to the basic Arapaho C; however, the probe nose was replaced with a conical nose with a spherical tip. The third

1 — RISER LINE

2 — RADIAL/SUSPENSION LINES

3 — INLET REINFORCING WEB

4 — SKIRT GORE PANEL

5 — CENTERLINE ROOF-TO-SKIRT SEAM

6 — ROOF GORE PANEL

7 — ROOF CAP

8 — SWIVEL

9 — CONFLUENCE RING
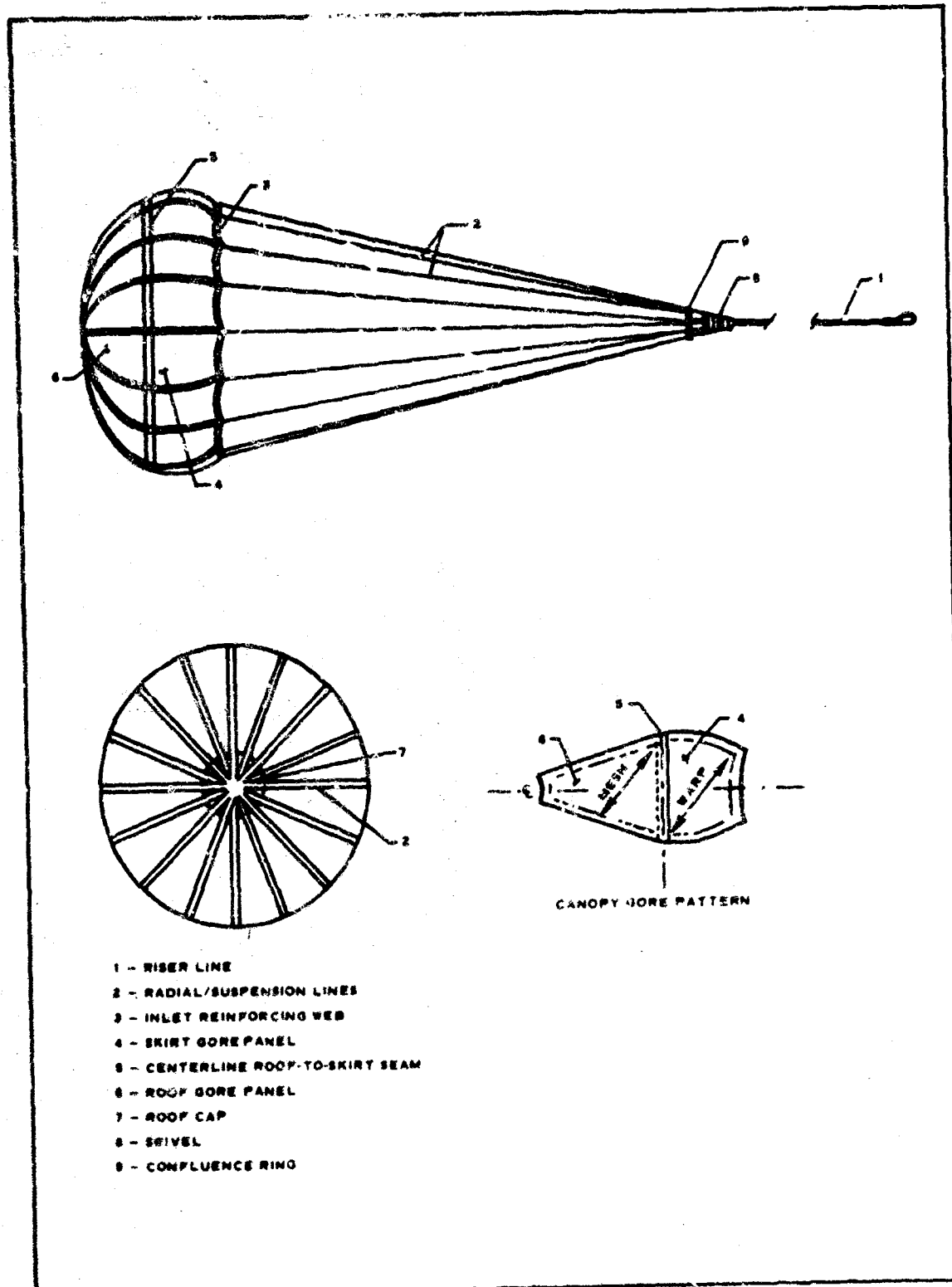
Figure 28 - PARASONIC Decelerator Terminology
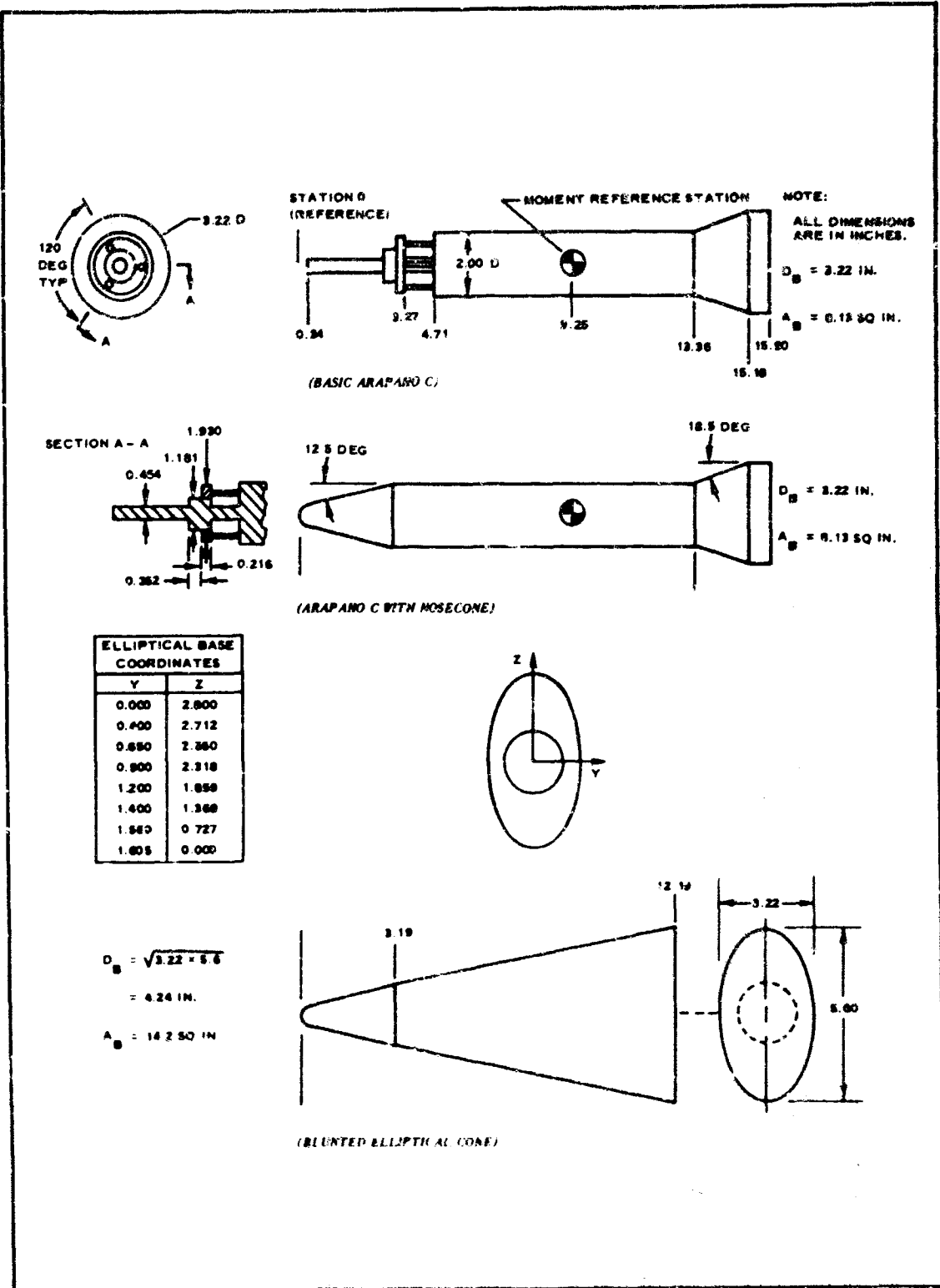
Figure 29 - Forebody Model Details

forebody consisted of a blunted elliptical cone with a nose shape identical to the nose used on the second forebody.

Two types of PARASONIC canopies were tested. One type was constructed with a prewoven Nomex fine-mesh cloth as the roof material, and the second type was constructed with a hand-woven coarse-mesh roof. Two canopy sizes were tested so that a canopy area to forebody base area ratio of 3.425 could be obtained for all forebodies. As stated earlier, all canopies were constructed with the same total aerodynamic porosity. The construction details for the parachute models are shown in Appendix V.

Two series of parachute performance tests were conducted under this program. The first series of tests (WT-IIB) was of sufficient scope to produce enough data to determine the effects of the aforementioned parameters on the parachute performance. The second series of performance tests (WT-VI) was conducted using a redesigned drag measurement system to obtain data having a higher degree of accuracy as the comparative basis for the drag predictive method discussed in Section V. The results of this series of tests were also used to validate the results of the first series of tests. A summary of the test conditions for both series of tests is shown in Table IV.

Results obtained from the parachute performance tests are presented in Appendix V. Both drag and stability parameters were determined. The base pressure to free stream static pressure (P_b/P_∞) values were recorded to indicate the degree of modification of the forebody wake due to the proximity of the attached decelerator. Table V lists the P_b/P_∞ ratios for the three forebodies without a decelerator immersed in the inner wake.

Comparison of the values in Tables V with the results presented in Appendix V gives an indication of the degree of wake modification. The remaining parameters listed in Appendix V describe the stability and drag characteristics of the parachute. General stability comments are discussed in Item 8, below.

3. MACH NUMBER EFFECTS

Figures 30 and 31 illustrate the effects of the free stream Mach number on the drag coefficient of PARASONIC models behind the Arapaho C with nose cone and the blunted elliptical cone forebodies. The trend of decreasing drag coefficient with increasing Mach number shown in these figures is typical of supersonic parachute performance. The Mach number effect, however, is interrelated with forebody shapes, parachute axial location (X/D), and canopy to forebody base area ratio (A_c/A_b). The major interrelationship of interest is the combination of Mach number, X/D, and A_c/A_b values at which severe modification of the forebody wake is encountered. It has been found that for a given forebody-parachute combination, the axial location at which severe modification is encountered increases as the free stream Mach number increases. Further discussion of the interrelation of the free stream Mach number and other influencing parameters is presented in applicable sections.

TABLE IV - PARACHUTE PERFORMANCE TEST

CONDITIONS SUMMARY

Forebody	Mesh	A_c/A_b	M_∞	q_∞ (psi) Min	Max	X/D Min	Max
WT-IIB							
Basic Arapaho C	Small	3.425	2, 3, 4, 5	0.5	1.5	4.5	8
	Large	3.425	2, 3, 4, 5	0.5	1.5	4.5	8
	Small	5.9	3, 4	0.5	1.5	6.0	9
	Large	5.9	3, 4	0.5	1.5	6.0	8
Blunted elliptical cone	Small	1.99	2, 3, 4, 5	0.5	1.5	4.0	8
	Large	1.99	3, 4	0.5	1.	4.0	8
	Small	3.425	2, 3, 4, 5	0.5	1.5	4.5	8
	Large	3.425	2, 3, 4, 5	0.5	1.5	4.5	8
Arapaho C with nose cone	Small	3.425	2, 3, 4, 5	0.5	1.0	4.5	8
	Large	3.425	2, 3, 4, 5	0.5	1.0	4.5	8
	Small	5.9	3, 4	0.5	1.0	6.0	10
	Large	5.9	3, 4	0.5	1.0	6.0	10
WT-VI							
Arapaho C with nose cone	Small	3.425	2, 3, 4, 5	1.0	1.0	5.0	7
	Large	3.425	2, 3, 4, 5	1.0	1.0	5.0	7
Blunted elliptical cone	Small	3.425	2, 3, 4, 5	0.5	0.5	5.0	7
	Large	3.425	2, 3, 4, 5	1.5	0.5	5.0	7

TABLE V - FOREBODY P_b/P_∞ RATIOS

Forebody	P_b/P_∞ $M_\infty = 2$	$M_\infty = 3$	$M_\infty = 4$	$M_\infty = 5$
Basic Arapaho C	0.56	0.25	0.23	0.24
Arapaho C with nose cone	0.50	0.24	0.19	0.17
Blunted elliptical cone	0.49	0.29	0.17	0.15
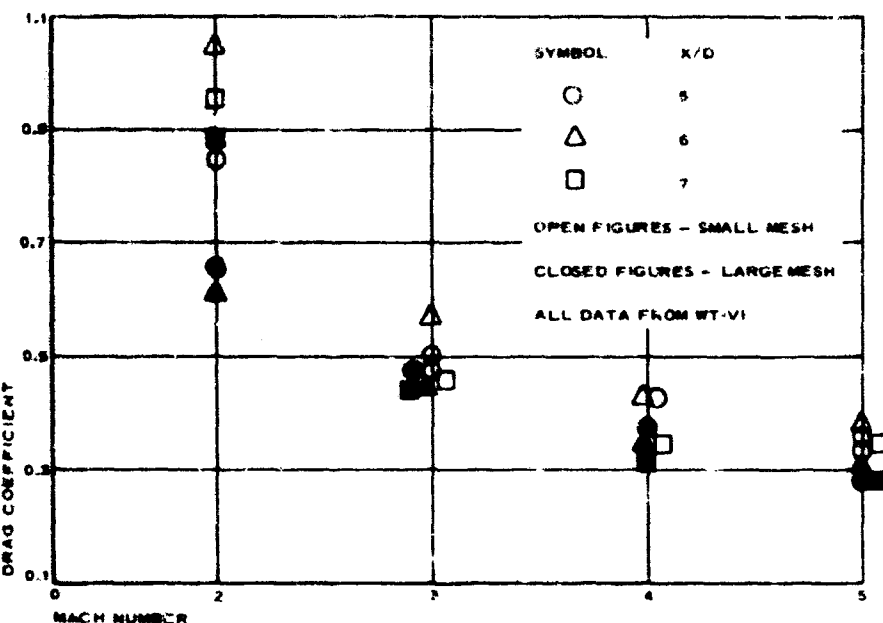
Figure 30 - Drag Coefficient versus Mach Number, Arapaho C with Nose Cone Forebody, $A_c/A_b = 3.425$
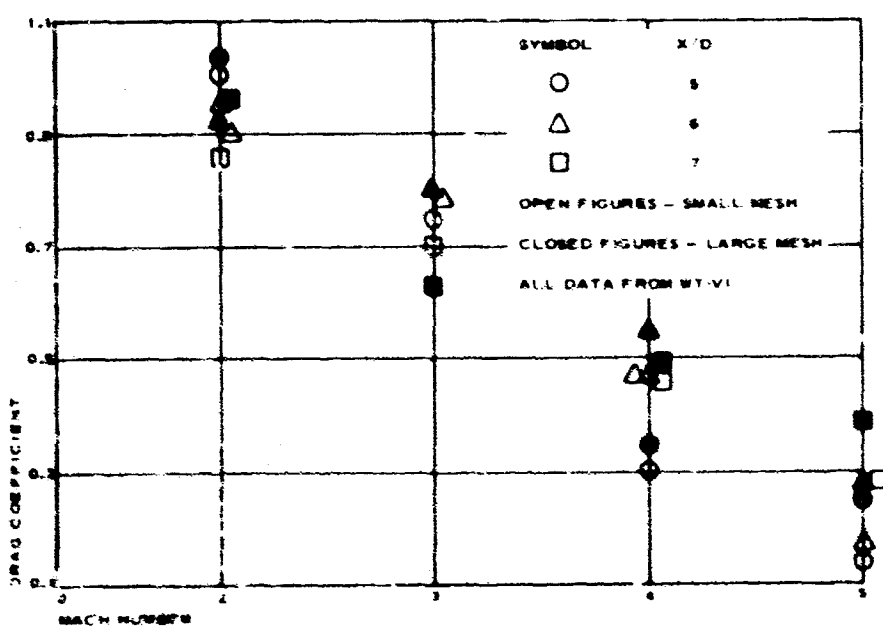
Figure 31 - Drag Coefficient versus Mach Number, Blunted Elliptical Cone Forebody $A_c/A_b = 3.425$

4. REYNOLDS NUMBER EFFECTS

In all cases during the parachute performance tests, the Reynolds numbers were such that the boundary layer at the base of the forebody was turbulent; the viscous portion of the wake was, therefore, also turbulent. Any variations in parachute drag due to operation in a laminar viscous wake could not, therefore, be determined.

The variation of parachute drag behind a given forebody depends on the profile of the flow field entering the parachute. A slight variation of velocity profiles with a variation in total pressure can be seen in Figures 8 through 15. For the wake survey tests, the temperatures were held constant at each Mach number; the variation of Reynolds number can be directly related with the variation of total pressure. Considering that the Reynolds number variation for the parachute tests was approximately half the variation for the wake survey tests, and that the wake profiles shown in Figures 8 through 15 do not indicate significant variations with Reynolds number, it can be safely assumed that the changes in parachute drag over the range of Reynolds numbers tested will be very slight.

From the wind-tunnel test results of WT-IIB, a slight correlation between variations of Reynolds number and variations of drag coefficient magnitude was observed. However, inaccuracies of the drag measurement system may have affected the repeatability of these slight trends. Figures 32 through 35 illustrate the effect of the free stream Reynolds
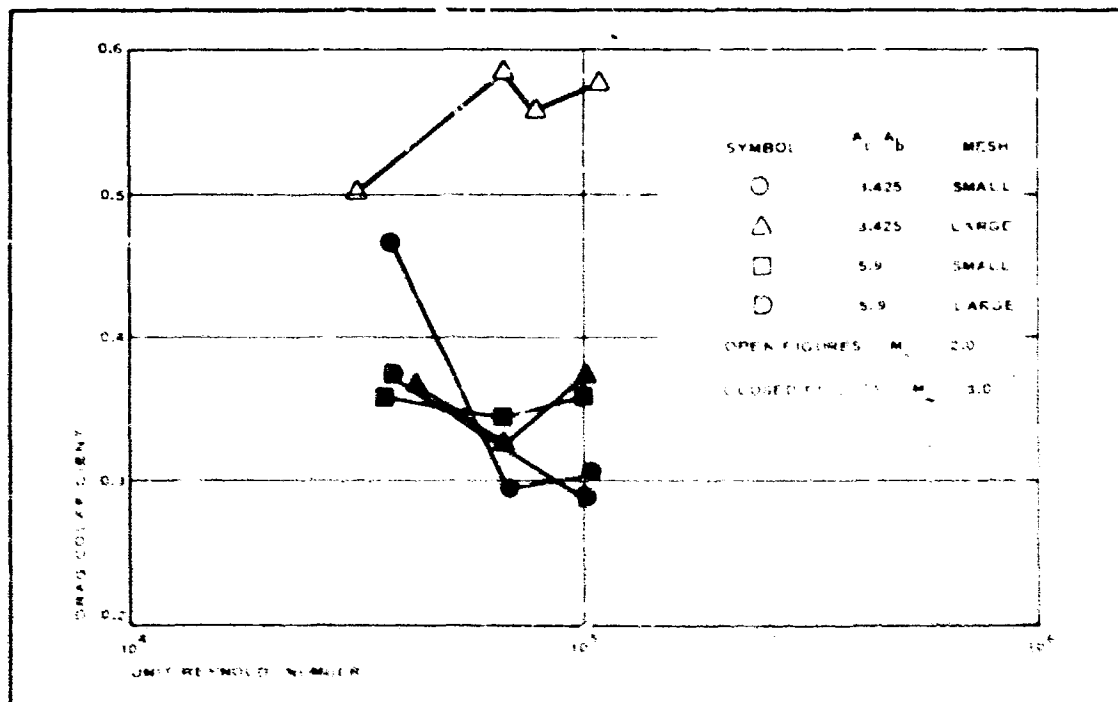
Figure 32 - Drag Coefficient versus Unit Reynolds Number, Basic Arapaho C Forebody (M_∞ = 2 and 3)
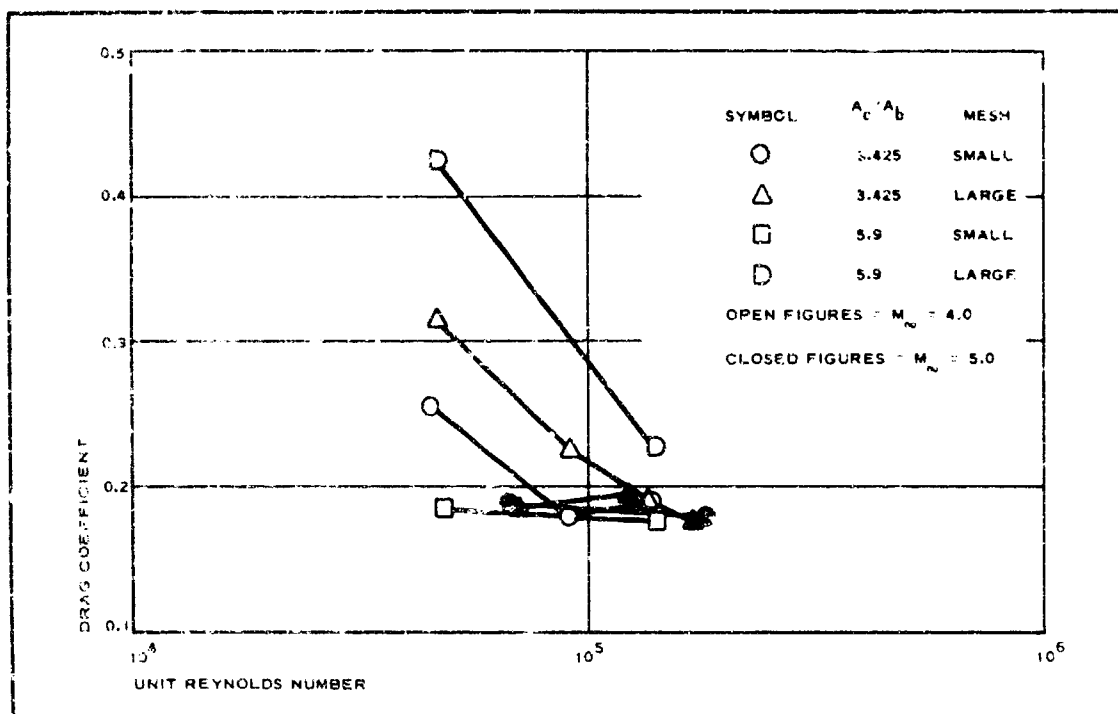
Figure 33 - Drag Coefficient versus Unit Reynolds Number, Basic
Arapaho C Forebody (M_∞ = 4 and 5)
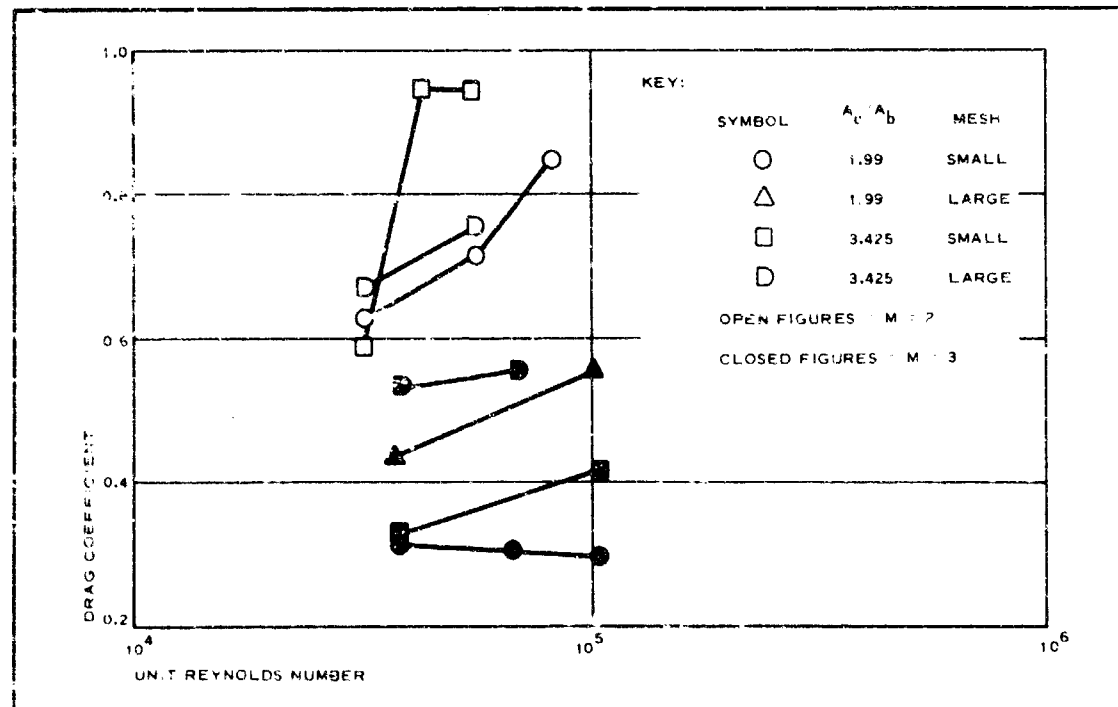
Figure 34 - Drag Coefficient versus Unit Reynolds Number, Blunted
Elliptical Cone Forebody (M_∞ = 2 and 3)
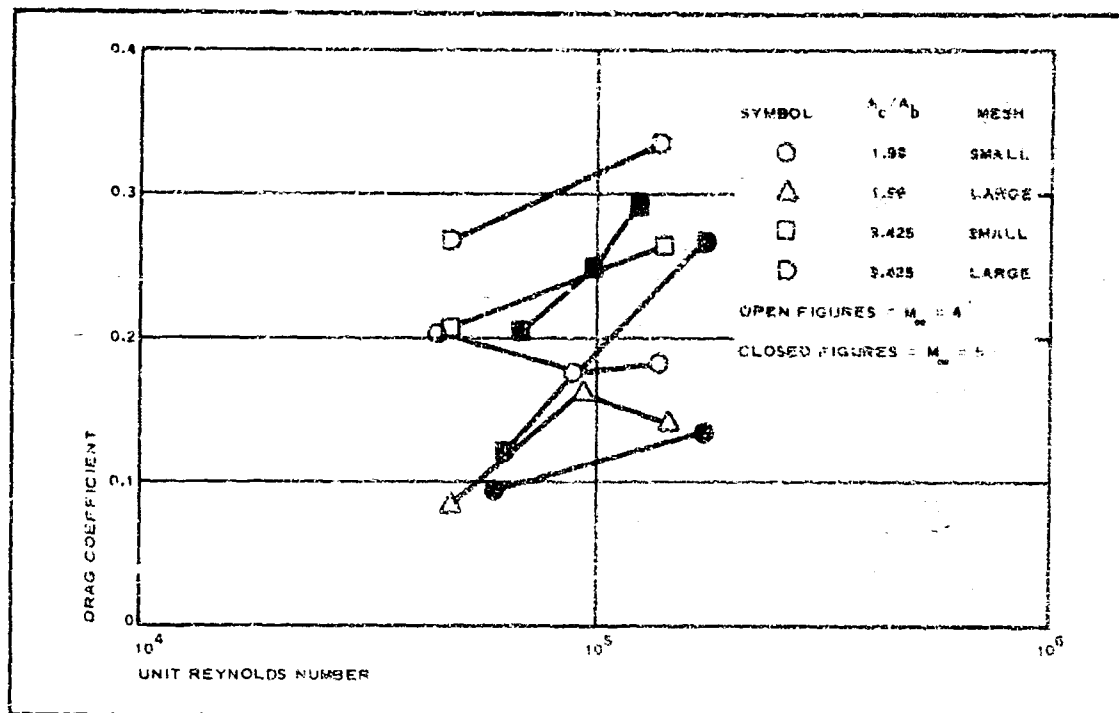
Figure 35 - Drag Coefficient versus Unit Reynolds Number, Blunted
Elliptical Cone Forebody (M_∞ = 4 and 5)

number on various forebody-parachute combinations. The canopy loca-
tion of X/D = 6 was chosen because of the near optimum performance
exhibited by the parachutes at this location.

The figures indicate that, behind the blunted elliptical cone model, there
is a slight increase in drag coefficient with an increase of Reynolds num-
ber. However the Reynolds number trends appear to be reversed for
the axisymmetric forebody. An explanation of this trend reversal has
not been determined.

5. FOREBODY EFFECTS

Of the three forebody models used in the parachute performance testing,
two (the basic Arapaho C and the Arapaho C with nose cone forebodies)
were axisymmetric; the third (blunted elliptical cone) had an elliptical
cross section at the base. The third model was tested to simulate the
wake of a lifting re-entry body.

The forebody effects on drag coefficient magnitudes are shown in Fig-
ure 36. The data shown on this figure were obtained from the second
series of tests (WT-VI) and reflect a high degree of accuracy. The
data indicate the effects of forebody asymmetry on parachute perfor-
mance. The PARASONIC performance appears to have a higher degree
of Mach number sensitivity in the wake of the asymmetric forebody as
opposed to the axisymmetric forebody. The forebody effect is most

61
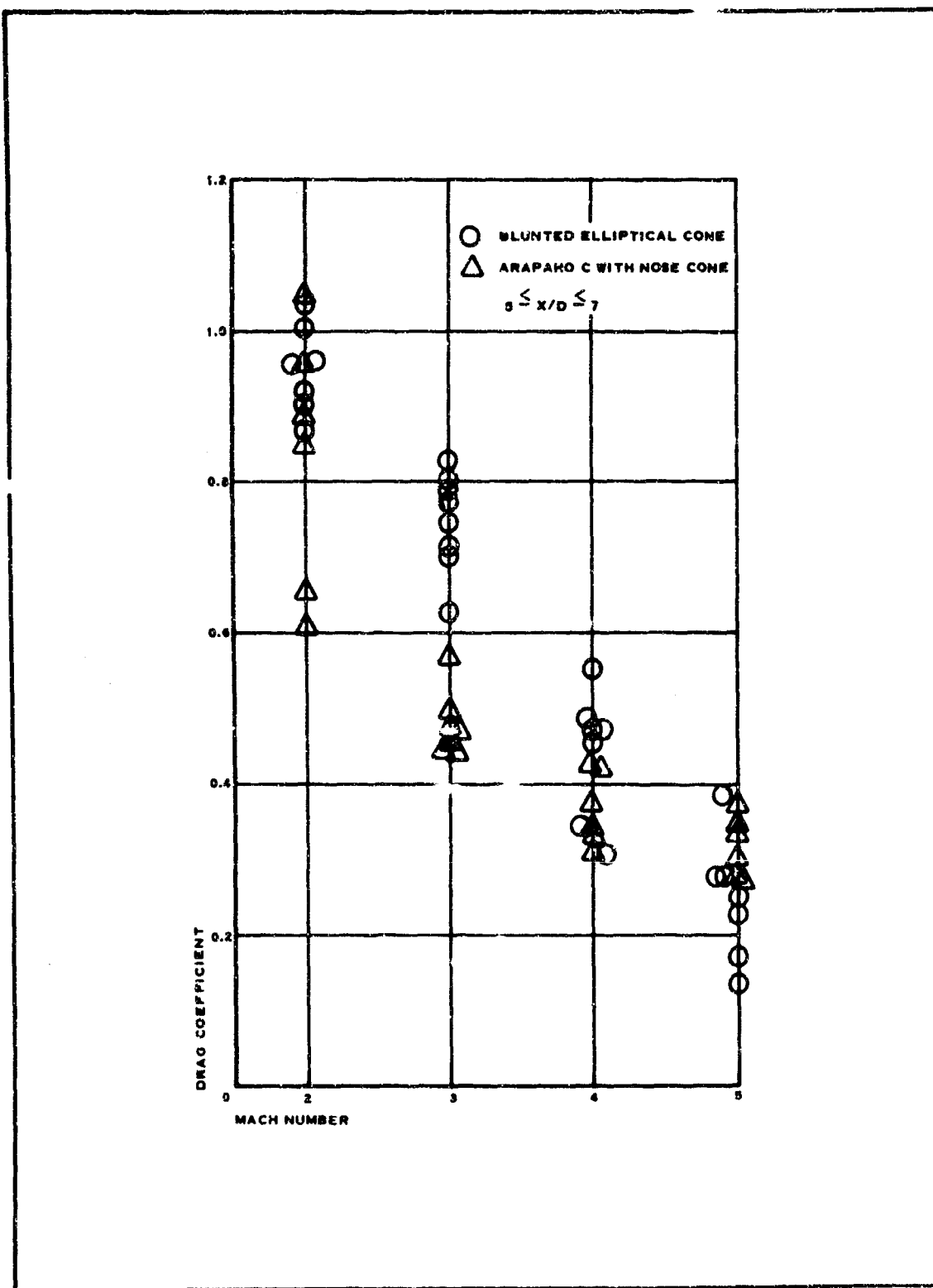
Figure 36 - Drag Coefficient versus Mach Number, Blunted Elliptical
Cone and Arapaho C with Nose Cone Forebodies

apparent at M_∞ = 3. At M_∞ = 2, the effect is not quite as apparent;
however, the M_∞ = 2 data for the axisymmetric forebody may be in
error due to slight damage of the canopy suspension line. This damage
is discussed further in Item 6, below. At M_∞ = 5, the low drag coeffi-
cient values for the blunted elliptical cone data are attributed to severe
wake modification. This also is discussed further in Item 6.

6. CANOPY AXIAL LOCATION EFFECTS

The axial location of the canopy aft of the forebody was found to become
critical at the extreme ends of the X/D range tested. At the near X/D
locations (X/D = 4 to 4.5), the proximity of the canopy to the forebody
base resulted in severe wake deformations. In some cases, the modi-
fication was of such severity that the wake was considered to be "blown;"
i.e., flow leaving the forebody base separates and passes around, rather than
through, the canopy. In the blown wake conditions the flow field entering
the canopy is subsonic and an extremely low drag coefficient results.
At canopy inlet locations greater than X/D = 7, the oscillation stability
was found to be very time dependent and, at times, the oscillations be-
came divergent in nature. The breathing action of the parachute also
appeared to be X/D dependent, with the magnitude of the breathing in-
creasing with decreasing distance between canopy and forebody base.
From a stability standpoint, therefore, the optimum location of the
canopy inlet was found to be at approximately X/D = 6.

Figure 30 indicates that at the X/D = 6 canopy inlet position, the drag
coefficient is also optimized. When the Mach number 2 data (which do
not follow this trend) are examined in more detail, and specifically the
oscillation angles associated with these data points, it can be shown that
the upper two data points exhibited oscillation angles varying from 10 deg
to 13 deg; the middle two data points, angles from 6 deg to 8 deg; and
the lower two data points, no oscillations. The three data points for the
small-mesh parachutes at the Mach 2 conditions were affected by a near
failure of the parachute. Immediately after completion of the Mach 2
points, inspection of the small-mesh parachute indicated some slippage
of the suspension lines at the point of attachment to the swivel. The slip-
page of the suspension lines was such that the parachute inlet was no longer
normal to the flow.

The drag coefficient data presented in Figure 35 for the blunted elliptical
cone model also indicates a near optimum canopy location at X/D = 6
except for the Mach number 5 conditions. For X/D's = 5 and 6 at M_∞ =
5, and X/D = 5 at M_∞ = 4, the modification of the wake was such that
the parachute inflated with an elliptical shape normal to the flow with the
major axis of the elliptical canopy in the same plane as the major axis
of the elliptical forebody base. The degree of ellipticity was most severe
at the M_∞ = 5, X/D = 5 test point. At these test points, the canopy was
virtually motionless.

7. PARACHUTE TO FOREBODY BASE AREA RATIO EFFECTS

The parachute to forebody base area ratios (A_c/A_b) varied only during
the first series of parachute performance tests (WT-IIB), and the data
accuracy may have influenced any slight trends. The A_c/A_b effects can

be seen on Figures 32 to 35. It does appear that the smaller A_c/A_b ratios exhibit slightly smaller drag coefficient values for the blunted elliptical cone data. For the smaller area ratio (1.99), the viscous portion of the wake is considered to have a noticeable effect on the drag coefficient value. The trend of smaller drag coefficient values with the smaller area ratio is not apparent in the Basic Arapaho C data. In this case, the smaller area ratio (3.425) is great enough that the viscous portion of the wake has little effect on the drag coefficient.

The primary effect of A_c/A_b, as discussed previously, is associated with the canopy location at which wake modification is encountered. Reference 32 indicates that the X/D position of the parachute behind the forebody at which wake modification occurs is directly proportional to the ratio of the parachute size to the forebody size. The results of the wind-tunnel tests conducted under this program tend to substantiate this statement. At the $M_\infty = 5$, X/D = 6 conditions (WT-IIB) for the blunted elliptical cone tests, severe canopy breathing and wake modification were encountered for the $A_c/A_b = 3.425$ test points. However, for $A_c/A_b = 1.99$ at the same Mach number, no adverse effects were encountered at X/D = 6, and only slight wake modification observed at X/D = 5. Similar effects were observed with the axisymmetric forebodies; however, the effects were not nearly so severe.

8. GENERAL STABILITY

It was observed that with the decelerator positioned at a large X/D location, the oscillations induced in the parachute became divergent in nature, and axial repositioning was required.

The observations led to the conclusion that a near optimum X/D position should exist where the minimum inflation-oscillation instability is present. This near optimum X/D position was observed to be at X/D = 6.

The drag oscillation frequency (f_f) does not appear to be Mach-number dependent within the range tested. The canopy oscillation angles (α) and oscillation frequencies (f_o) show a decrease in magnitude with increasing Mach number. The breathing frequencies (f_b) did not appear to be Mach-number dependent. However, behind the blunted elliptical cone, the breathing pulsations were time dependent and usually of small magnitude so that breathing frequencies could not be determined. This indicates that although the drag coefficient experiences degradation with increasing Mach number, the stability is enhanced.

The canopy oscillations were of different form behind the two forebodies. Behind the basic Arapaho C, the oscillations were predominately of the coning type in which any point on the riser line follows a circular path in a plane normal to the direction of flow. Behind the blunted elliptical cone, few coning oscillations were observed. Oscillations behind the blunted elliptical cone were predominantly in the vertical plane. However, in some cases at far X/D positions, the oscillations in the vertical plane were combined with higher frequency oscillations in the horizontal plane. A point on the riser line, then, traces a zig-zag path. Unfortunately, frequencies and amplitudes could not be determined for oscillations in the horizontal plane.

Inflation stability for parachutes operating behind the blunted elliptical cone was highly X/D sensitive. In most all cases with the large-diameter parachute positioned at X/ 1.5, severe canopy breathing pulsations and wake deformations were encountered. Behind the basic Arapaho C, at the same X/D, A_c/A_b r and with the same roof mesh, canopy breathing pulsations and wake deformities were less severe.

Throughout the tunnel tests, on-line observations indicated that the canopy was assuming an elliptical shape normal to the direction of flow while operating behind the blunted elliptical cone. The degree of ellipticity increased with increasing Mach number and decreasing canopy X/D location. This ellipticity could not, however, be determined from the photographic coverage.

The type of roof mesh was found to have little effect on oscillation amplitudes or frequency, but to have an effect on inflation stability (breathing pulsations). The large-mesh canopies, being much more rigid than the small-mesh canopies, did not exhibit the high-frequency, low-amplitude canopy flutter observed with the small-mesh canopies. The large-magnitude canopy pulsations, referred to as breathing, were encountered with both canopies.

SECTION V

DRAG PREDICTION

1. GENERAL

This section presents a method for calculating the pressure drag of
PARASONIC parachutes operating in supersonic axisymmetric wakes.
The method uses the local wake profiles as the flow environment and the
flow through a curved shock wave to determine pressure distribution on
the parachute canopy. This is a great improvement over previous meth-
ods (Reference 33), which assume flow conditions at the parachute inlet
equal to the free stream conditions ahead of the forebody and a normal
shock standing at the parachute inlet. The canopy flow field in this
analysis is determined using the following basic assumptions:

1. A detached, curved, shock is present ahead of the
   canopy inlet.

2. The presence of the canopy in the wake produces
   negligible distortions of the wake flow field.

3. The flow is sonic through the roof grid.

4. The flow stagnates at solid portions of the canopy
   roof.

5. Secondary effects due to separated flow and skin
   friction can be largely ignored.

2. FLOW FIELD ANALYSIS

The flow analysis begins with the determination of the local flow para-
meter profiles in the wake. The most important parameters required
for this analysis are the local Mach number (M_L), static pressure (P_L),
pitot pressure (P_{t_L}), and dynamic pressure (q_L). These profiles,
obtained either from experimental tests or suitable analytical prediction
as described in Section III of this report, represent wake profiles that
are free from any adverse effects caused by the presence of a trailing
body in the wake flow field. The "free" wake profiles, therefore, cannot
be considered valid for the cases in which the trailing parachutes have
been known to modify the wake structure radically. Figures 37 and 38,
traced directly from schlieren photographs obtained during wind-tunnel
tests (Section IV), illustrate the effect of the parachute axial positioning
on the wake flow structure. The flow-field modification is quite evident
with the parachute inlet positioned at $X/D = 4.5$. With the parachute in-
let positioned at $X/D = 8$, however, the wake trailing shock does not
appear to be deformed. The position of the trailing shock indicates,
however, that the presence of the parachute causes a slight widening of
the wake neck. This slight modification of the wake is not considered
in the drag prediction analysis.
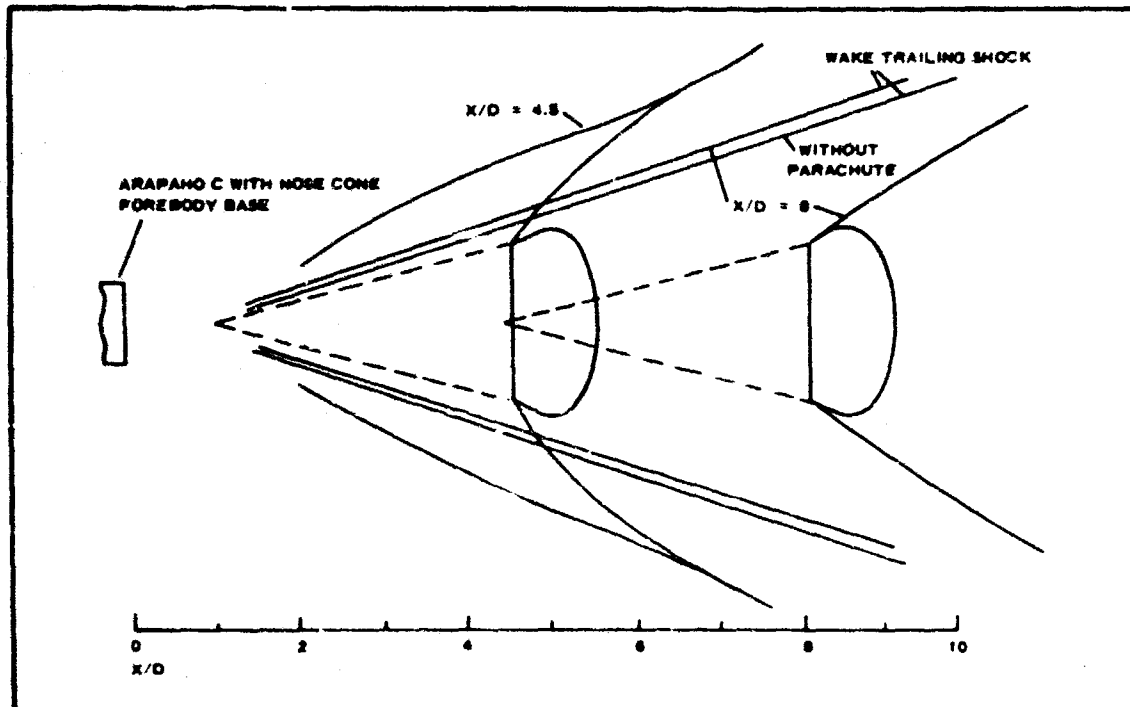
Figure 37 - Wake and Parachute Shock Structure ($M_\infty = 3$)
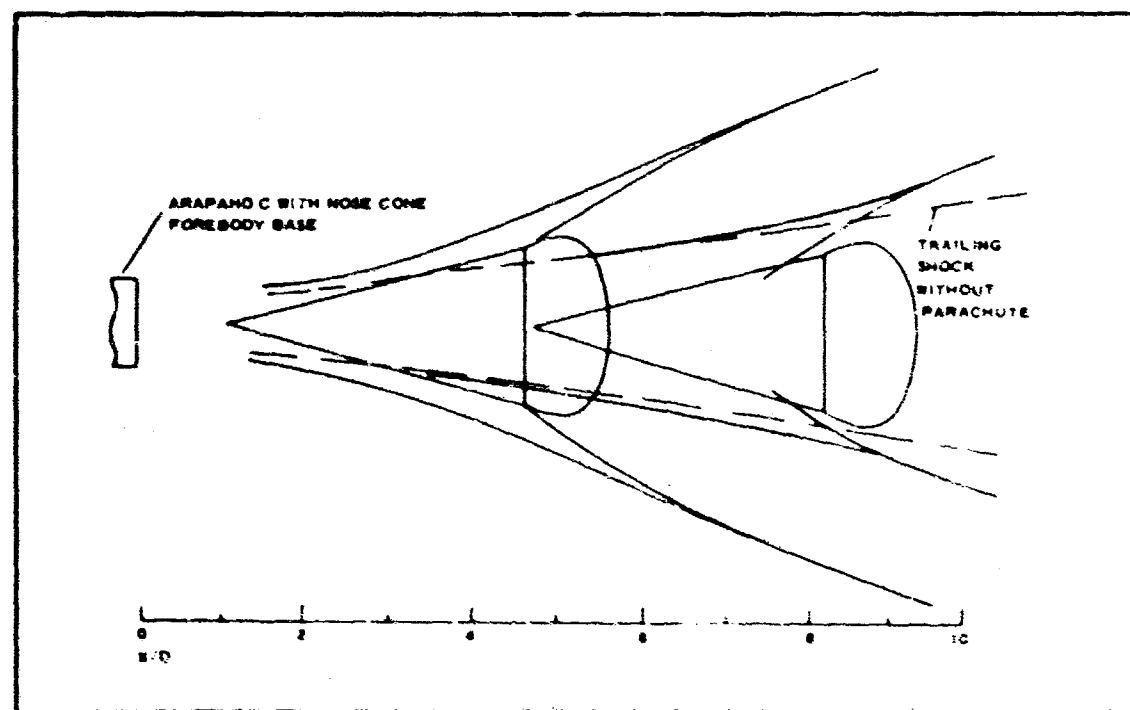
Figure 38 - Wake and Parachute Shock Structure ($M_\infty = 5$)

On the assumption that the wake profiles have been determined, the next step in the flow analysis is to select profiles at an axial station immediately ahead of the canopy oblique shock. When this procedure is used, the influence of the parachute confluence point and suspension lines on the flow field is neglected. This simplifies the analysis but may influence the accuracy of the predictive method.

Analyses of schlieren photos show that two general types of shocks appear around the supersonic parachute: detached inline shocks and attached shocks at the canopy inlet. The shape and stand-off distance of the inline shock is determined by the local Mach number profile and the aerodynamic porosity of the canopy (Reference 34). The shape of the attached shock is determined by the shape of the canopy and by the Mach number profile behind the parachute inline shock and is present only when the flow at the inlet edge is supersonic. The shape of the attached inlet shock need not be known for the drag prediction analysis. The shape of the inline shock must, however, be known in order to determine the pressure distribution inside the canopy. The shape of the inline shock, unfortunately, is not easily predicted. The shock wave oscillations encountered with relatively low-porosity canopies (Reference 34) along with the interaction of the shock wave and the flexible suspension lines result in a very unstable inline shock and, therefore, a nonsteady flow field entering the canopy inlet. Inflation and oscillation stability also affect the stability of the inline shock. The flow analysis, then, assumes the canopy to be motionless and the inline shock to be quasi-steady.

Analysis of the schlieren photos indicate one other interesting phenomenon associated with the canopy inline shock. In some cases a seemingly intense and steady inline shock would lose its identity at the very center. This "hole" in the center of the shock indicates subsonic flow conditions at the wake centerline. The subsonic core at the wake centerline is most probably caused by the formation of a wake by the parachute attachment swivel and confluence ring. In cases where the forebody wake centerline velocity is at low supersonic velocities, further deceleration of the flow by the swivel and confluence ring then results in a subsonic core of air entering the parachute inlet.

3. CANOPY PRESSURE DISTRIBUTION

The pressure distribution on the supersonic parachute canopy is determined by two flow paths: internal, through the canopy, and external, around the canopy. The flow field in which the canopy is engulfed is influenced by the detached oblique shock ahead of the canopy. With free stream profiles obtained from experiment or from the method described in Section III and a detached shock wave shape determined from either experiment or some applicable predictive method, flow parameters aft of the detached shock wave may be determined by the use of oblique shock relations. Both the total and static pressures are required to determine the pressure distribution on the canopy. In the absence of further perturbations aft of the shock waves, the parameters are combined within stream layers. If the shock is discontinuous at the wake centerline region, the flow is still considered isentropic and is treated as one-dimensional and compressible.

The axial velocities in the stream layers are assumed to stagnate on the solid portions of the canopy mesh and on the canopy roof cap (see Figure 39). The surfaces of the canopy skirt, however, are assumed to be acted upon by the static pressure of the stream layer entering the parachute at the inlet edge. The parachute canopy acts as a supersonic diffuser in that the flow inside is decelerated, and the kinetic energy of the flow is converted to a pressure rise. At each mesh opening the flow is assumed to be sonic; the static pressure in the opening is then

$$P_e = 0.528 \, P_{t_e} \, .$$

The external flow influence on the canopy is divided into two regions. The first region is skirt surface, beginning at the inlet edge and ending at the juncture of the skirt material and the roof mesh. From the leading edge of the skirt to the point of maximum camber, the skirt is assumed to have a constant slope, and the pressures on this surface are assumed to follow conical flow theory. Along the skirt surface aft of the point of maximum camber, the flow expands and is assumed to be analogous to the flow over a ring-type airfoil, whereon the pressure coefficient along the upper surface may determined from Reference 35 as

$$C_P = \frac{2}{\beta} \left(\frac{a}{b} - \alpha_0 \right) \, .$$

4. PRESSURE DRAG COEFFICIENT EVALUATION

The pressure drag associated with a supersonic parachute is the major drag component, and its analytically determined magnitude is an accurate estimation of the total drag of the parachute. Determination of secondary drag components is beyond the scope of this analysis. The pressure drag is evaluated using the method described below.

The pressure drag is evaluated by a summation of the axial components of the pressure differential acting on the parachute canopy (see Figure 40).

Examining a ring of radius r, and width ds, the tangent at point A intersects the parachute centerline at an angle ϕ. The surface area of the ring is then

$$dA_{surf} = 2\pi r ds \, ,$$

but

$$ds = dr \csc \phi \, ,$$

therefore,

$$dA_{surf} = 2\pi \csc \phi \, r dr \, .$$

The pressure differential acting on the ring is

$$\Delta P = P_{int} - P_{ext} \, .$$
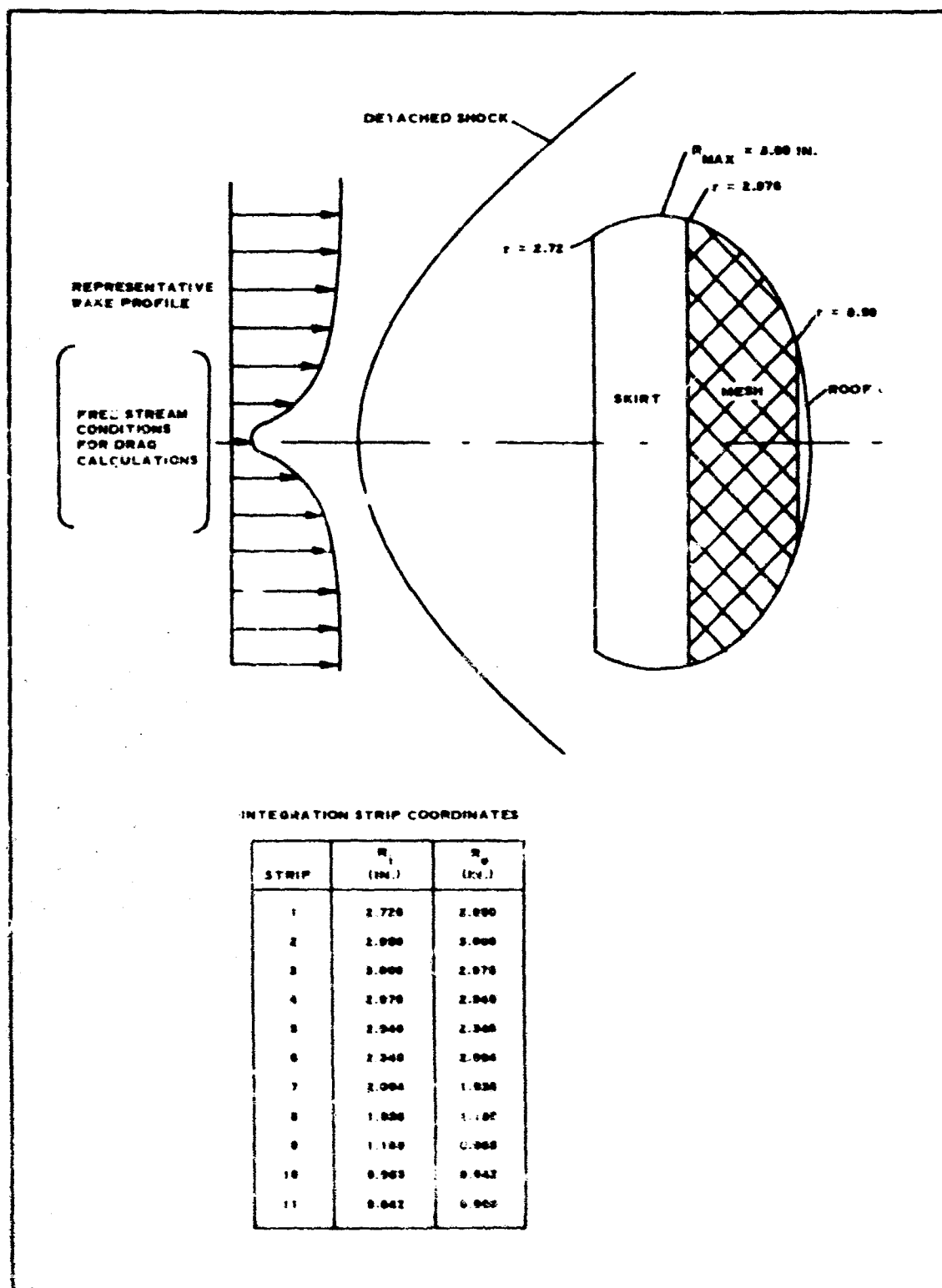
Figure 39 - Parachute Flow Environment
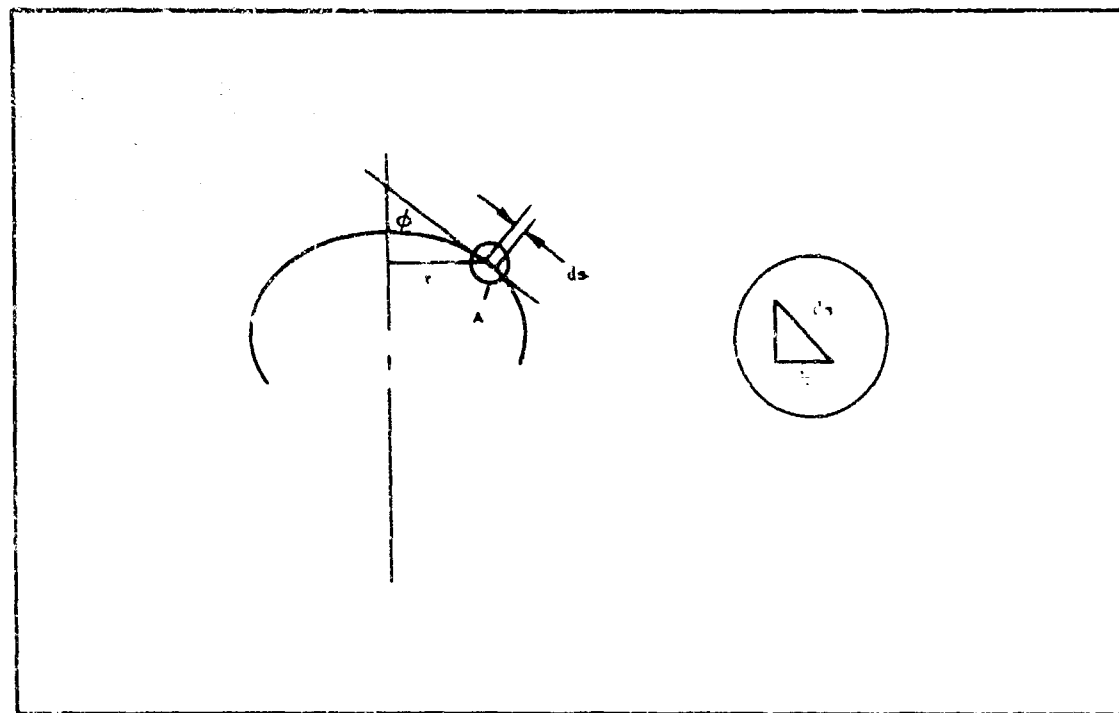
Figure 40 - Canopy Cross Section

and the force perpendicular to the surface is the pressure differential
multiplied by the surface area. The component of the force parallel to
the parachute centerline is the axial drag force and can be expressed as

$$dD = \Delta P d\lambda_{surf} \sin \phi$$

$$= \pi \Delta P \csc \phi \sin \phi \, r dr$$

$$= 2\pi \Delta P \, r dr \quad .$$

The pressure drag of the canopy is equal to

$$D_P = q_\infty C_{D_P} A = 2\pi \int_{r_o}^{r_i} \Delta P_i \, dr \quad ,$$

and the drag coefficient is then

$$C_{DP} = \frac{2\pi}{q_\infty (\pi R^2)} \int_{r_o}^{r_i} \Delta P r dr \quad .$$

Simplified and put in nondimentional form, the radii are

$$C_{DP} = \int_{\frac{r_o}{R}}^{\frac{r_i}{R}} \frac{\Delta P}{q_\infty} \, d\left(\frac{r}{R}\right)^2 \quad .$$

For regions of constant pressure differential, the incremental pressure drag coefficient can be expressed as

$$\Delta C_{DP} = \frac{\Delta P}{q_\infty} \left[\left(\frac{r_i}{R}\right)^2 - \left(\frac{r_o}{R}\right)^2 \right] \quad .$$

To simplify the calculation procedure, this equation may be rewritten as

$$\Delta C_{DP} = (C_{P\ internal} - C_{P\ external}) \left[\left(\frac{r_i}{R}\right)^2 - \left(\frac{r_o}{R}\right)^2 \right]$$

or

$$\Delta C_{DP} = \Delta C_P \left[\left(\frac{r_i}{R}\right)^2 - \left(\frac{r_o}{R}\right)^2 \right] \quad .$$

The total pressure-drag coefficient is then

$$C_{DP} = \sum_{i=1}^{n} \Delta C_{DP_i} \quad .$$

5. RESULTS

Using the methods described in Item 4 above, several sample calculations were made and compared to drag coefficient values obtained in experimental tests (Appendix V). For the sample calculations, the parachute canopy was broken up into 11 annular rings, each assumed to have a uniform pressure differential across its surface. The location and size of these integration strips was based on the construction of the parachute models tested and on the pressure distribution on the canopy. Figure 39 shows the canopy construction and the coordinates of the integration strips.

Strips 1 through 3 make up the total skirt surface. Strips 4 through 9 comprise the mesh portion of the canopy roof. These strips are divided into open and closed areas. Strips 4 and 6 are the open strips and equal the total open area of the canopy. Strips 10 and 11 correspond to the non-porous cap on the canopy roof. The choice of 11 integration strips was deemed sufficient for obtaining reasonable results from the initial calculations.

The wall profiles used for the initial calculations were obtained from

wind-tunnel tests (Appendix V). The wake profiles were obtained in both
horizontal and vertical planes during the wind-tunnel tests. However,
the forebody mounting strut was in the horizontal plane, and the wake
measurements in that plane were considered to be influenced by the wake
of the strut. The wake profiles in the vertical plane were then used and
were assumed to be axisymmetric. The shock shapes were obtained
directly from schlieren photographs of the test items. From the shock
shape and wake profiles, the conditions aft of the shock were determined.
A first assumption was that the streamlines aft of the shock remain
parallel to the wake axis. The results of computations made using this
assumption indicated that accounting for any radial transposition of the
streamlines would not substantially increase the accuracy of the calcu-
lation method.

Table VI lists the conditions and calculated values for one of the test
cases. In Figure 41, results obtained using the drag predictive method
are compared with experimental wind-tunnel data (Section IV). Table VII
presents the same data in tabular form. The selection of canopy axial
positioning at each Mach number was based on parachute stability and
the availability of a well defined shock shape from schlieren photographs.
As can be seen, there is good correlation between the calculated and
experimental values. In most of the test cases the calculated values
have smaller magnitudes than the corresponding experimental data. The
accuracy of the method does not appear to be highly Mach-number de-
pendent; however, as the Mach number increases, the possibility of wake
modification due to proximity of decelerator and forebody becomes greater.

TABLE VI - SAMPLE CALCULATION DATA

						Wake profile parameters*					
Y/D	P_1 (psf)	M_1	θ	$M_1 \sin\theta$	P_2 (psf)	P_{t2} (psf)	C_{p2}	C_{pt2}	C_{pe}	$C_{p\,conical}$[+]	$C_{p\,ext}$[‡]
0	28.40	0.70	· · ·	· · ·	· · ·	30.4	· · ·	.0756	· · ·	· · ·	· · ·
0.2	28.40	1.70	44°	1.18	41.4	66.9	.0904	.267	.048	· · ·	· · ·
0.3	27.60	1.92	40°	1.23	44.0	68.8	.114	.286	.055	· · ·	· · ·
0.5	28.80	2.70	38°	1.66	87.8	116.8	.410	.610	.228	· · ·	· · ·
0.6	28.20	2.76	38°	1.70	90.4	119.0	.431	.630	.241	.360	.017

*These data were calculated at the following free stream conditions: (1) para-
chute - $M_\infty = 3.00$, $q_\infty = 0.98$ psi, $Re/in = .069 \times 10^6$, $X/D = 6.0$, $P_{t\infty} = $
5.7 psi; and (2) wake measurements - $M_\infty = 3.00$, $q_\infty = 1.01$ psi, $Re/in. = $
$.069 \times 10^6$, $X/D = 3.$ $P_{t\infty} = 5.9$ psi.

[+] Conical flow theory

[‡] Ring airfoil theory
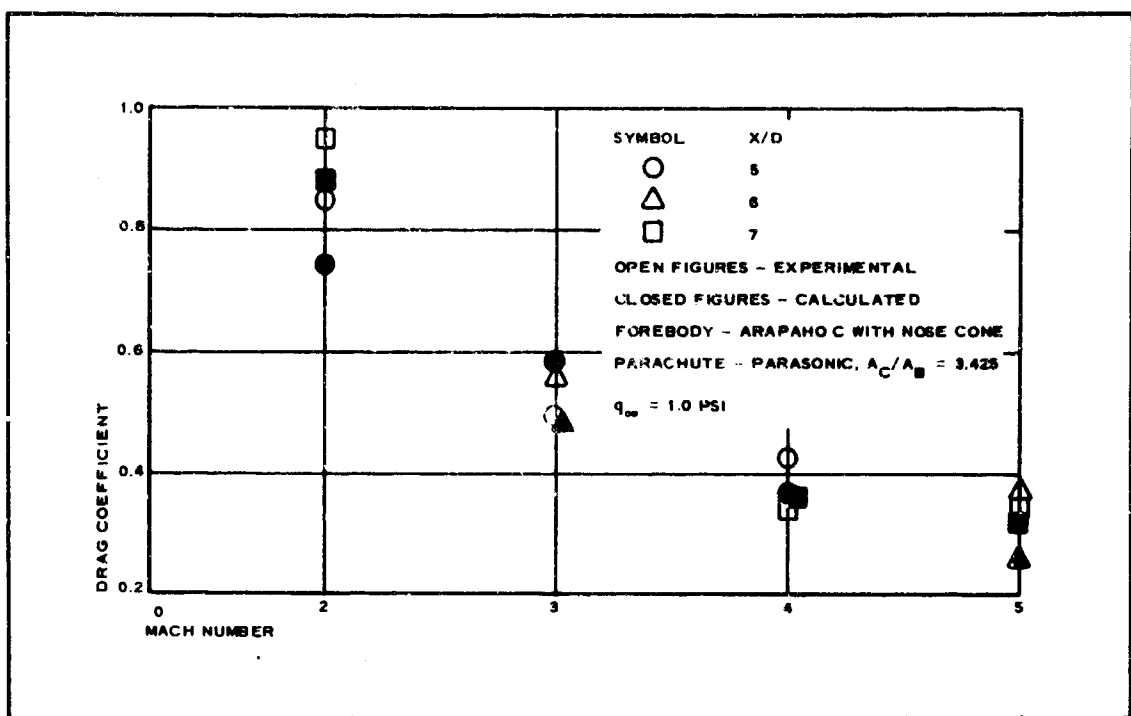
Figure 41 - Correlation of Experimental and Calculated C_D Values

TABLE VII - EXPERIMENTAL AND CALCULATED DRAG

COEFFICIENT VALUES

M_∞	X/D	C_{DP}	$(C_D)_{exp}$	$C_{DP}/(C_D)_{exp} \times 100$
2	5	0.734	0.850	86.4
	7	0.873	0.950	92.0
3	5	0.585	0.494	118.3
	6	0.482	0.563	85.7
4	5	0.369	0.423	87.3
	7	0.361	0.340	106.0
5	6	0.260	0.376	69.2
	7	0.320	0.342	93.5

75

The pressure drag is the major drag component, and the theoretically determined drag magnitude is an excellent indication of the supersonic parachute performance. Evaluation of other drag-influencing parameters listed below could possibly enhance the accuracy of the predictive method.

1. Skin friction

2. Separated flow effects

3. Confluence point and suspension line effects

4. Effective porosity variation due to flow compressibility

Calculation of drag components attributed to these phenomena does not appear practical from an engineering standpoint; therefore, only trends are discussed.

The skin-friction drag can be neglected without sacrificing appreciable accuracy. The drag component attributed to separated flow effects may have a slight effect on the accuracy; however, evaluation of this component does not appear practical. The influence of the confluence point and suspension lines has been studied (Reference 34), and results indicate that the number of suspension lines does affect the internal pressure distribution on the canopy. The effect of the confluence point and suspension lines has been taken into account somewhat in that the shock shapes used for the initial calculations were obtained in the presence of the confluence point and suspension lines. The variation of effective porosity with Mach number does not appear to be an appreciable factor when dealing with the low porosities associated with supersonic parachutes.

Recommendations for future work are included in Section VII.

SECTION VI

CONCLUSIONS

1. A method of solution was developed to predict the flow field properties
    as well as the boundary layer momentum thickness and momentum de-
    fect over axisymmetric, asymmetric, and two-dimensional forebodies.

2. A method of solution was developed to predict the properties of the wake
    flow field behind an axisymmetric forebody in a supersonic free stream.

3. These methods have been programmed in FORTRAN IV. Results using
    this program have shown good agreement with experimental wake re-
    sults over a large range of free-stream Mach numbers and axial loca-
    tions aft of the forebody base.

4. A method for calculating supersonic parachute drag using wake profiles
    as free-stream conditions was developed.

5. Results using the parachute drag predictive method have been compared
    with experimental data and good agreement has been shown.

6. The results of the PARASONIC parachute performance tests indicate
    that, although the drag coefficient decreases with increasing Mach num-
    ber, stability generally is enhanced. The effects of wake asymmetry on
    parachute performance became more pronounced as the Mach number
    increased. The drag coefficient values did not show any repeatable
    trends associated with Reynolds number or type of roof mesh.

SECTION VII

RECOMMENDATIONS

The following tasks are recommended as desirable improvements to the forebody, wake, and decelerator analyses:

1. Forebody analysis .- Improve the turbulent boundary layer momentum defect calculation by using advanced methods for determining body friction coefficients

2. Viscous wake analysis
   a. Better determine the starting point for the wake calculation and consider modification of the starting point from the rear stagnation point to the viscous wake neck

   b. Extend the analysis to flows with Prandtl number not equal to 1

   c. Include the effect of axial pressure gradient (this would increase the complexity of the analysis)

   d. Develop a solution for the near wake region (this would require a major effort).

3. Inviscid wake analysis
   a. Include the effect of radial pressure gradients

   b. Account for the effect of embedded oblique shock wakes (wake recompression shock and flare shock) on the inviscid wake profiles

4. Wake solution
   a. Investigate methods for matching the viscous wake and inviscid wake edge conditions

   b. Apply the wake solution to additional experimental data to determine the choice of viscosity model and viscosity coefficient that best correlates theory and experiment

   c. Perform a sensitivity analysis to determine which modifications to the analysis method will improve the solution the most

5. Drag prediction

   a. Extend the drag predictive analyses to apply to non-porous decelerators

   b. Conduct experimental tests on rigid decelerator models of simple geometry (for example, cores and spheres) and correlate with analytical results

(Reverse is blank)
79

APPENDIX I

BOUNDARY LAYER THEORY

1. LAMINAR BOUNDARY LAYER THEORY

For the methods developed by Kemp, Rose, and Detra (Reference 1) for calculating boundary layer properties and, in particular, calculating momentum thickness (θ), Stetson (Reference 6) has presented an empirical correlation of the results of the numerical solutions for θ, which is given by

$$\theta = \frac{\sqrt{2\xi}}{\rho_e u_e r^k} (0.491)(1 - 0.090\beta^{0.4})(\rho_e \mu_e / \rho_w \mu_w)^{0.386} . \tag{24}$$

Here,

$$\xi = \int_0^s \rho_w \mu_w u_e r^{2k} ds$$

and s is the distance from the stagnation point as measured along the surface of the body: $k = 0$ for two-dimensional flow, and $k = 1$ for axisymmetric flow. For nonaxisymmetric flow, one of these two cases must be used as a suitable approximation. For example, a flat delta of small thickness ratio is best approximated as a two-dimensional body, while an elliptical body with its major and minor axes on the same order of magnitude is more suitably approximated as a quasiaxisymmetric body ($k = 1$).

In the above equations, the subscript e denotes local conditions at the edge of the boundary layer, while w denotes local gas conditions at the wall. The effect of β, the pressure gradient parameter, is small in Equation 24. This can be seen since β ranges from one at a two-dimensional stagnation point to zero in a zero pressure gradient region; thus, a typical value for β represents no more than a 10 percent correction.

In Equation 24, ξ represents an effective surface distance that considers the prior boundary layer history. For purposes of calculation, can be rewritten as

$$\xi(s) = P_s V_\infty \frac{\mu_w}{R_1 T_w} R^{2k + 1} \xi^* , \tag{26}$$

where

$$\xi^* = \int_0^{s/R} \frac{P_e}{P_s} \frac{u_e}{V_\infty} \left(\frac{r}{R}\right)^{2k} d\left(\frac{s}{R}\right) . \tag{27}$$

P_s is the forebody nose stagnation pressure, V_∞ the free-stream velocity, and R the base radius for an axisymmetric body or an effective base radius for a nonaxisymmetric body, assuming μ/RT = constant.

The boundary layer momentum thickness, θ, can be rewritten in terms of ξ^*. The result is

$$\frac{\theta}{R} = \frac{\sqrt{2}\,(0.491)\left(1 - 0.090\beta^{0.4}\right)\xi^{*\frac{1}{2}}}{\left(\dfrac{\rho_e u_e R}{\mu_e}\right)^{1/2}\left(\dfrac{u_e}{V_\infty}\right)^{1/2}\left(\dfrac{P_e}{P_s}\right)^{1/2}\left(\dfrac{r}{R}\right)^k\left(\dfrac{\rho_e \mu_e}{\rho_w \mu_w}\right)^{0.114}} \ . \qquad (28)$$

Here, β can be evaluated from

$$\beta = 2\,\frac{\xi^*}{u_e}\left(\frac{\partial u_e}{\partial \xi^*}\right)\phi = \text{const} . \qquad (29)$$

When the local boundary layer momentum is known, M can be evaluated from

$$M = \int_{\text{circumference}} \rho_e u_e^2 \theta\, ds \qquad (30)$$

where ds is a circumferential increment of length. From Equation 28, $\rho_e u_e^2 \theta$ can be written as

$$\rho_e u_e^2 \theta = \frac{\rho_\infty V_\infty^2 R \sqrt{2}\,(0.491)(1 - 0.090\beta^{0.4})\xi^{*1/2}}{\left(\dfrac{\rho_\infty V_\infty R}{\mu_\infty}\right)^{1/2}\left(\dfrac{\mu_\infty}{\mu_w}\right)^{1/2}\left(\dfrac{r}{R}\right)^k\left(\dfrac{\rho_w \mu_w}{\rho_e \mu_e}\right)^{0.386}}\,\frac{u_e}{V_\infty}\left(\frac{\rho_s}{\rho_\infty}\right)^{1/2}\left(\frac{T_s}{T_w}\right)^{1/2} \ .$$

$$(31)$$

Thus, the integral in Equation 30 can be evaluated readily once the local flow properties have been used to evaluate ξ^*, θ/R, and $\rho_e u_e^2 \theta$. For a circular body and by evaluating the integral at the base,

$$M = \pi D\left(\rho_e u_e^2 \theta\right)_{\text{base}} \ , \qquad (32)$$

For a body with an elliptical cross section, M can be expressed as

$$M = 4 \int_0^{\pi/2} \rho_e u_e^2 \frac{\theta}{R} G_1 R^2\, d\phi \ . \qquad (33)$$

where, because of the symmetry, it is only necessary to integrate over one quadrant, and where

$$
G_1 = \frac{1}{R}\frac{ds}{d\phi} \frac{\left[1 + \frac{\sin^2\phi \, \cos^2\phi}{\left(\frac{\sin^2\phi}{b^2} + \frac{\cos^2\phi}{a^2}\right)^2}\left(\frac{1}{b^2} - \frac{1}{a^2}\right)^2 \right]^{1/2}}{\left[ab\left(\frac{\sin^2\phi}{b^2} + \frac{\cos^2\phi}{a^2}\right) \right]^{1/2}} . \tag{24}
$$

Here, b and a are the semiaxes of the ellipse. G_1 is unity for a cylindrical body.

Once the inviscid flow properties along the edge of the body boundary layer are known, and assuming the wall temperature is known or can be estimated, then the boundary layer momentum thickness and integrated momentum defect can be evaluated using Equations 28 and 30.

2. TURBULENT BOUNDARY LAYER THEORY

Unfortunately, the state of knowledge regarding turbulent boundary layers is not so well developed as in the laminar case. Thus, although there have been many approximate treatments of turbulent flow, most of which can be supported to some extent by using existing experimental data, there are no "exact" theoretical solutions (such as those of Kemp, Rose, and Detra) for laminar flow.

One approximate solution, the results of which lend themselves to the present problem, is that of Reshotko and Tucker (Reference 7). This solution uses the momentum integral and moment-of-momentum equations as simplified using Stewartson's transformation. To solve these two equations, a skin friction relation must be used; Reshotko and Tucker chose the Ludwieg-Tillman relation in a form suitable for compressible flow with heat transfer through applying the reference enthalpy concept. The above equations were simplified further by using an approximate shear stress distribution and the power law velocity profile.

The moment-of-momentum equation is needed to account for pressure gradient effects on the boundary layer velocity profile. The method of Reshotko and Tucker, as applied to insulated surfaces, is quite well founded. However, for noninsulated or nonadiabatic wall cases the method, though qualitatively correct, is based on some speculative assumptions. It is still anticipated, however, that for such cases the method will yield reasonable quantitative results. The method certainly is representative of the best that can be done within the present status of turbulent flow theory.

Reshotko and Tucker in Reference 7 present their results for momentum thickness in terms of a transformed momentum thickness, θ_{tr}. The transformed momentum thickness, θ_{tr}, can be related to the actual momentum thickness, θ, by

$$\theta = \theta_{tr}\left(1 + \frac{\gamma - 1}{2} M_e^2\right)^3 . \tag{35}$$

The solution for θ_{tr} is

$$\theta_{tr} = \left[\theta_{tr}\left(\frac{M_e a_o \theta_{tr}}{\nu_o}\right)^{0.2155} M_e^B R^{1.2155k}\right]_s - \left[\theta_{tr}\left(\frac{M_e a_o \theta_{tr}}{\nu_o}\right)^{0.2155} M_e^B R^{1.2155k}\right]_{s_1}$$

$$+ 0.01173 \int_{s_1}^{s} \frac{M_e^B\left(\dfrac{T_e}{T_{ref}}\right)^{0.732} R^{1.2155k} ds}{\left(\dfrac{T_o}{T_e}\right)^{3.268}} . \tag{36}$$

Here, a_o and ν_o are the velocity of sound and the kinematic viscosity evaluated at the stagnation conditions of the local external stream, respectively. The exponent B can be expressed approximately as

$$B = 4.2 + 1.58\left(\frac{T_w}{T_o}\right) - 1 . \tag{37}$$

where T_o is the inviscid stagnation temperature. The reference temperature, T_{ref}, is given as

$$T_{ref} = 0.50\,(T_w + T_e) + 0.22\,(T_{aw} - T_e) . \tag{38}$$

where T_{aw} is the adiabatic wall or recovery temperature

$$T_{aw} = T_e\left(1 + \frac{\gamma - 1}{2} M_e^2 Pr^{1/3}\right) . \tag{39}$$

The distance, s_1, in Equation 36 is the starting point of the calculation. If the boundary layer is turbulent over the entire body, then $s_1 = 0$, and the calculation starts at the forward stagnation point. However, if the boundary layer is initially laminar, then the calculation starts at $s = s_1$, the transition point. At that point,

$$\theta\text{(turbulent)} = \theta\text{(laminar)} . \tag{40}$$

The previously noted equation for a compressible turbulent boundary layer (Equation 36), can be recast in terms of a turbulent distance parameter, ξ_T, where

$$\xi_T^* = \frac{1}{M_e^B \left(\frac{r}{R}\right)^{1.2155k}} \int_{\frac{s_1}{R}}^{s/R} \frac{M_e^B \left(\frac{r}{R}\right)^{1.2155k}}{\left(\frac{T_{ref}}{T_e}\right)^{0.732} \left(\frac{T_o}{T_e}\right)^{3.268}} d\frac{s}{R} . \quad (41)$$

The transformed momentum thickness, θ_{tr}, then can be expressed as

$$\left(\frac{\theta_{tr}}{R}\right)^{1.2155} = \left[\frac{\theta_{tr}(TR)}{R}\right]^{1.2155} \left[\frac{P_o(TR)}{P_o}\right]^{0.2155} \left[\frac{M_e(TR)}{M_e}\right]^{0.2155 + B} \times$$

$$\frac{\left[\frac{r(TR)}{R}\right]^{1.2155k}}{\left(\frac{r}{R}\right)^{1.2155k}} \cdot \frac{0.01173 \, \xi_T^*}{\left(\frac{M_e Ra}{\mu_o/\rho_o}\right)^{0.2155}} . \quad (42)$$

TR indicates that the property is to be evaluated at the transition point.

When θ_{tr} is known, the actual momentum thickness, θ, can be evaluated as can Re_θ, $\rho_e u_e^2 \theta$, and M. For this latter quantity, Equations 32 through 34 are applicable. Thus, calculations can be carried out for the important boundary layer properties once the properties at the edge of the boundary layer are known.

APPENDIX II

FORLBODY FLOW FIELD PROGRAM

The forebody geometry is stored as a table to allow all necessary geometric properties to be determined by simple calculation from the geometric coordinates. The storage system defines the body profile as a series of points that are the values of the distance r from the forebody axis to its surface and as a function of the axial distance x from the nose of the body. Thirteen profiles are stored on 13 planes formed by rotating the vertical plane containing the forebody axis about this axis 90 deg in 7.5-deg increments. Mirror symmetry is assumed about the vertical and horizontal planes.

The one geometric input required by the boundary layer program is the value of r/R, where R is average base radius. The value, r, is found as a function of x along any one ϕ by linear interpolation between the points stored in the table.

For the pressure distribution subroutine, the angle of the forebody surface in each ϕ plane with the body axis must be known. To calculate this,

$$\theta_{i, \phi} = \arctan \frac{r_{i+1, \phi} - r_{i, \phi}}{x_{i+1, \phi} - x_{i, \phi}} . \tag{43}$$

The application of the Newtonian or tangent-cone method for estimating the static pressure distribution is governed by the following logic. The free-system Mach number and the static pressure (M_∞ and p_∞) are inputs to the pressure distribution subroutine. For each ϕ profile, the following checks and decisions are made.

The nose angle is calculated from the stored geometry,

$$\theta_{0, \phi} = \arctan \frac{r_{1, \phi} - r_{0, \phi}}{x_{1, \phi} - x_{0, \phi}} . \tag{44}$$

This value then is compared with a stored curve of θ_c versus M_∞, where θ_c is the critical cone angle between conical flow with an attached conical shock and flow with a detached shock.

Case A

$$\theta_{0, \phi} \geq \theta_c .$$

If $\theta_{0, \phi}$ is equal to or larger than θ_c, then the shock wave is detached from the nose, and static pressure is estimated by the Newtonian flow

$$p_e = p_s \sin^2 \theta_{0, \phi} ,$$

where p_s is the nose total pressure. Since there is a detached shock, p_s is the free-stream impact pressure.

$$P_s = \left[p \frac{(\gamma + 1)M_\infty^2}{2} \right]^{\frac{\gamma}{\gamma - 1}} \left[\frac{\gamma + 1}{2\gamma M^2 - (\gamma - 1)} \right]^{\frac{1}{\gamma - 1}} . \qquad (45)$$

<u>Case B</u>

$$\theta_0, \phi < \theta_c .$$

If θ_0, ϕ is less than θ_c, then an attached conical shock exists, and both the static and nose total pressure are evaluated from the conical flow subroutine. For both cases, the local Mach number is given by

$$M_e = \sqrt{ \frac{2}{\gamma - 1} \left[\left(\frac{p_o}{p_e} \right)^{\frac{\gamma - 1}{\gamma}} - 1 \right] } .$$

where p_o is the local total pressure. In this region, $p_o = p_s$.

This solution is carried out at each point on the body profile. As long as $\theta_{i, \phi} > \theta_{i + 1, \phi}$, the local total pressure is equal to the nose total pressure for both cases. If the shock wave is detached, the static pressure is obtained by the Newtonian method until $\theta_{i, \phi} < \theta_c$, after which the conical flow solution is used.

If, however, $\theta_{i, \phi} < \theta_{i + 1, \phi}$, a corner shock forms, and the local total pressure changes. To evaluate this condition, the flow properties in the region $x_{i - 1}$ to x_i are used, and the angle $\overline{\theta} = \theta_{i + 1, \phi} - \theta_{i, \phi}$ is the conical semiangle of interest. As before, there are two possible cases. For Case A where $\overline{\theta} \geq \theta_c$ for M_{e_i},

$$p_{e_{i + 1}} = p_{o_{i + 1}} \sin^2 \overline{\theta} .$$

where $p_{o_{i + 1}}$ = local total pressure behind a detached (normal) shock. This pressure is given by

$$P_{o_{i + 1}} = p_s \left[\frac{(\gamma + 1)M_{e_i}^2}{(\gamma - 1)M_{e_i}^2 + 2} \right]^{\frac{\gamma}{\gamma - 1}} \left[\frac{\gamma + 1}{2\gamma M_{e_i}^2 - (\gamma - 1)} \right]^{\frac{1}{\gamma - 1}} .$$

For Case B where $\overline{\theta}$ is less than θ_c for $M_{e_{i - 1}}$, the static and total pressures are taken from the conical flow routine using the local properties at point i as inputs. Again, the Mach number is given in either case by

$$M_e = \sqrt{\frac{2}{\gamma - 1}\left[\left(\frac{P_{o_i} + 1}{P_c}\right)^{\frac{\gamma - 1}{\gamma}} - 1\right]} \tag{46}$$

APPENDIX III

BOUNDARY LAYER TRANSITION PREDICTION

1. **GENERAL**

A criteria for boundary layer transition was established that could be incorporated into a general laminar-turbulent boundary layer calculation program. Any such criteria must, because of what is known regarding transition and turbulent flow, be considered as leading to only an approximate estimate.

In developing transition prediction criteria, recognition must first be made of the factors that influence transition, the parameters in terms of which transition correlations usually are made, and which of these factors are important and can be considered realistically. In general, boundary layer transition depends on the Reynolds number of the flow, surface roughness, free-stream turbulence, noise, compressibility effects and/or pressure gradient effects, and whether the boundary layer is being heated or cooled. Except for effects due to surface roughness and free-stream turbulence, one might think that the other effects are of such a nature that methods of predicting their associated influence on transition could be developed. However, the effects of roughness and turbulence each may couple with the other factors, thus making any attempt to separate one effect from another extremely difficult.

As an example, the effect of surface roughness depends on the thickness of the boundary layer, but the thickness of the boundary layer depends on the compressibility of the fluid (as manifested through the local Mach number) and whether the boundary layer is being heated or cooled, as well as many other factors. The free-stream turbulence also may vary with tunnel conditions. Thus, the individual factors do couple with one another.

In evaluating factors affecting transition (see Figure 42), Low, in Reference 36, presents a curve showing the effect of free-stream turbulence on transition.

Gazley (Reference 37) found that laminar boundary layer oscillations and their damping or amplification could be detected only when the free-stream turbulence was less than 0.001. For greater turbulence values, the boundary layer oscillations became difficult to identify because of the near coincidence of their appearance with the point of transition to turbulence. Gazley also reported that the effects of free-stream turbulence tend to mask out the effects of other variables. This may explain the disagreement between Stainback (Reference 38) and Gazley. Stainback's results tended to confirm the invariance of transition Reynolds number with Mach number up to Mach 8; Gazley's results indicated an increase of transition Reynolds number with increasing Mach number.

Both Deem (Reference 39) and Stewart (Reference 40) indicate an increase of transition Reynolds number with an increase of unit Reynolds number. Deem also observed a transition reversal phenomenon due to changes in wall to adiabatic wall temperature ratios.
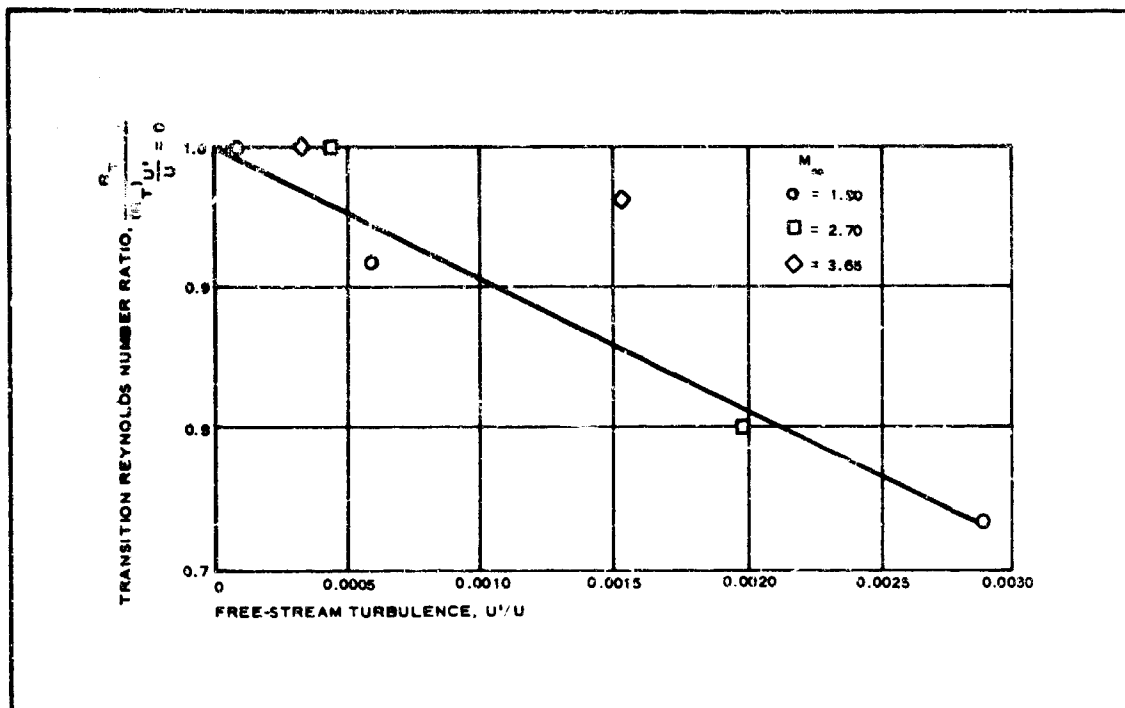
Figure 42 - Free Stream Turbulence, U'/U

Correlations cf boundary layer transition usually are presented in the
form of a transition Reynolds number as a function of other flow simi-
larity parameters. Although experimental data frequently are presented
using the free-stream Reynolds number based on X (Re_X), Reynolds
numbers based on momentum thickness and displacement thickness also
are used. If the transition process itself is viewed as originating
through local boundary layer separation occurring because of a local
momentum deficiency, then the local Reynolds number based on mo-
mentum thickness, Re_θ, would seem to be the appropriate dependent
variable. For an incompressible, flat-plate boundary layer, the critical
value of Re_θ corresponding to the boundary layer becoming unstable to
small disturbances (e.g., Tollmien-Schlicting waves) is 163 (Reference
41). On the other hand, the transition value may range as high as 1300,
depending on the exact surface roughness and free-stream turbulence,
both of which tend to decrease the value of the transition Reynolds num-
ber. For compressible flows, the Mach number and the ratio of the wall
enthalpy to the adiabatic wall enthalpy also become important.

Pressure gradient effects (a favorable gradient stabilizes the boundary
layer while an unfavorable gradient destabilizes it), although important,
are much more difficult to consider. The unit Reynolds number also is
included in many correlations of transition data. Originally, this para-
meter may have been related to wind-tunnel produced disturbances.
However, there is now some evidence that it also is an important effect
in correlating ballistic range and flight data. Its role, however, is not
understood from a physical viewpoint.

2.   ANALYSIS

In developing a rather simple correlation for the transition Reynolds number based on momentum thickness, only the effects of Mach number and h_w/h_{aw} are considered directly. Since the present boundary layer computer program calculated Re_θ, it is convenient to treat the transition problem in terms of this parameter. Furthermore, the free-stream Mach number range of interest in this study is from 2 to 5. For a blunt nose body, this means local Mach numbers of less than 3.5.

For wind-tunnel tests on Project EUREKA, the wall conditions were such that $h_w \approx h_{aw}$. For free-flight calculations, h_w/h_{aw} could range as low as 0.12, based on an upper limit of 6 for M_∞. Effects due to surface roughness and free-stream turbulence will not be included.

In general, the effect of the local Mach number on the transition Reynolds number in terms of X can be represented as shown in the following sketch (Reference 42 and 43).
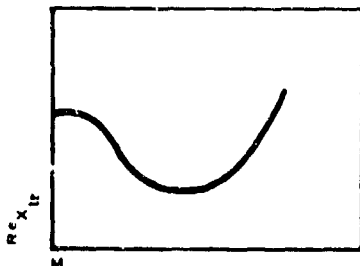
A curve of this type can be represented by a power series of the form

$$Re_{X_{tr}} = \left(Re_{X_{TR}}\right)_{inc} \sum_{n=0}^{m} a_n M^n \qquad (47)$$

If only the first four terms in the power series are used, the following boundary conditions can be applied:

1. $M = 0$, $Re_{X_{tr}} = \left(Re_{X_{tr}}\right)_{inc}$ (a value of 2.5×10^6 was chosen)

2. $M = 0$, $dRe_{X_{tr}}/dM = 0$

3. $M = M_1$, $dRe_{X_{tr}}/dM = 0$ (M_1 based on experimental data)

4. $M = M_1$, $Re_{X_{tr}}/\left(Re_{X_{tr}}\right)_{inc}$ (matched with experimental data)

If boundary conditions 3 and 4 are selected based on References 43 and 44, Equation 47 then becomes:

$$Re_{X_{tr}} = 2.5 \times 10^6 (1 - 0.12 M^2 + 0.023 M^3) \quad . \tag{48}$$

Since $Re_\theta \approx 0.664 Re_X^{1/2}$, (Reference 41), then

$$Re_{\theta_{tr}} \approx 1000 (1 - 0.12 M^2 + 0.023 M^3)^{1/2} \quad . \tag{49}$$

The effect of h_w/h_{aw} is illustrated in the following sketch:
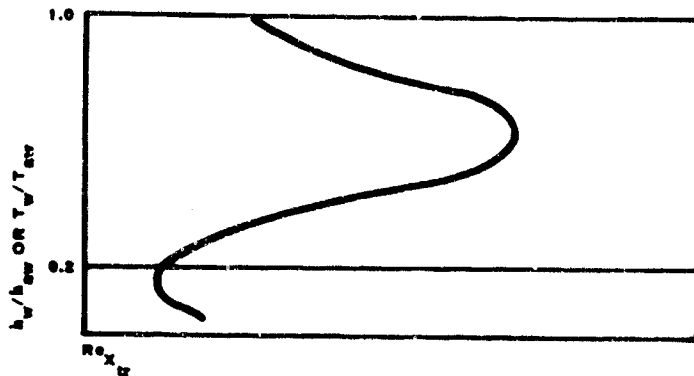
This curve can be represented by a power series of the form

$$Re_{X_{tr}} = \left(Re_{X_{tr}}\right)_{T_w = T_{aw}} \sum_{n=0}^{m} b_n \left(\frac{h_w}{h_{aw}}\right)^n \quad . \tag{50}$$

which can be fitted to available experimental data. When the range, $0.2 \leq h_w/h_{aw} \leq 1.0$, is considered, the boundary conditions become

1. $h_w/h_{aw} = 1$, $Re_{X_{tr}} = \left(Re_{X_{tr}}\right) T_w = T_{aw}$

2. $h_w/h_{aw} = \bar{h}_1$, $Re_{X_{tr}}$ (matched with experimental data)

3. $h_w/h_{aw} = \bar{h}_1$, $dRe_{X_{tr}}/dh_w = 0$

4. $h_w/h_{aw} = 0.2$, $Re_{X_{tr}}$ (matched with experimental data)

and where $Re_\theta \propto Re_X^{1/2}$, the correlation of Equation 49 becomes

$$Re_{\theta_{tr}} \approx 1000 \, (1 - 0.12 \, M^2 + 0.023 \, M^3)^{1/2} \, x$$

$$(-2.29 + 17.38 \, \bar{h} - 18 \, \bar{h}^2 + 3.91 \, \bar{h}^3)^{1/2} \qquad (51)$$

where $\bar{h} = h_w/h_{aw}$. Here, the effects due to h_w/h_{aw} are based on the experimental data of References 45 through 47.

The nature of this correlation is that transition reversal is included. However, the second transition reversal frequently found at values of h_w/h_{aw} of approximately 0.2 is not included. The correlation (Equation 51) thus is limited to $h_w/h_{aw} > 0.2$. Reshotko (Reference 48) has qualitatively explained both transition reversal phenomena. However, a general agreement among the available experimental data does not exist; the correlation, though qualitatively correct, is quantitatively only an approximation.

In representing the effects of Mach number and h_w/h_{aw} using power series, the coefficients in these series should be treated as functions of surface roughness and free-stream turbulence.

Pressure gradient effects, as noted before, also may be important. On this project, the primary bodies of interest are such that, excluding the nose region, the body is divided into regions of zero pressure gradient. This should be a reasonable approximation, even in the prediction of transition, with the one exception being at the junction of the cylindrical afterbody and the flare at the base of the body. The adverse pressure gradient there may produce transition if the Reynolds number is greater than the critical value. Thus, it was suggested that, in programming the boundary layer calculations, Re_θ at the initiation of the flare be checked against $(Re_\theta)_{CRIT}$ as given below:

$$(Re_\theta)_{CRIT} \approx 163 \, (1 - 0.12 \, M^2 + 0.023 \, M^3)^{1/2} \, x$$

$$(-2.29 + 17.38 \, \bar{h} - 18 \, \bar{h}^2 + 3.91 \, \bar{h}^3)^{1/2} \qquad (52)$$

This equation is merely Equation 51 with the incompressible transition value of a 1000 replaced by critical value 163). If at the flare, $Re_\theta \geq Re_{\theta_{CRIT}}$, then transition is assumed to occur. If $Re_\theta < Re_{\theta_{CRIT}}$, then the boundary layer remains laminar. With the inclusion of this criterion in the program boundary layer transition should at least be accounted for in a quantitatively correct manner.

The present correlation, Equation 52, has been compared with experimental results from Reference 40 on the effect of T_w/T_{aw} obtained at $M_\infty = 3.1$. Approximate agreement has been found to exist. The results of Stetson and Rushton (Reference 49) also have been compared; these results were obtained on blunt cones at a free-stream Mach number of

$M_\infty = 5.5$ (see Figure 43). Here, X_T is the transition distance, X_{sw} is the distance for the high entropy layer to be swallowed, and Re_{θ_T} is the transition Reynolds number based on momentum thickness. The prediction based on the present method is shown only for one condition; however, reasonable agreement exists.

Equations 51 and 52 have been programmed as a part of the boundary layer program and are used to determine the approximate location of transition if the exact location of transition is not specified as an input.
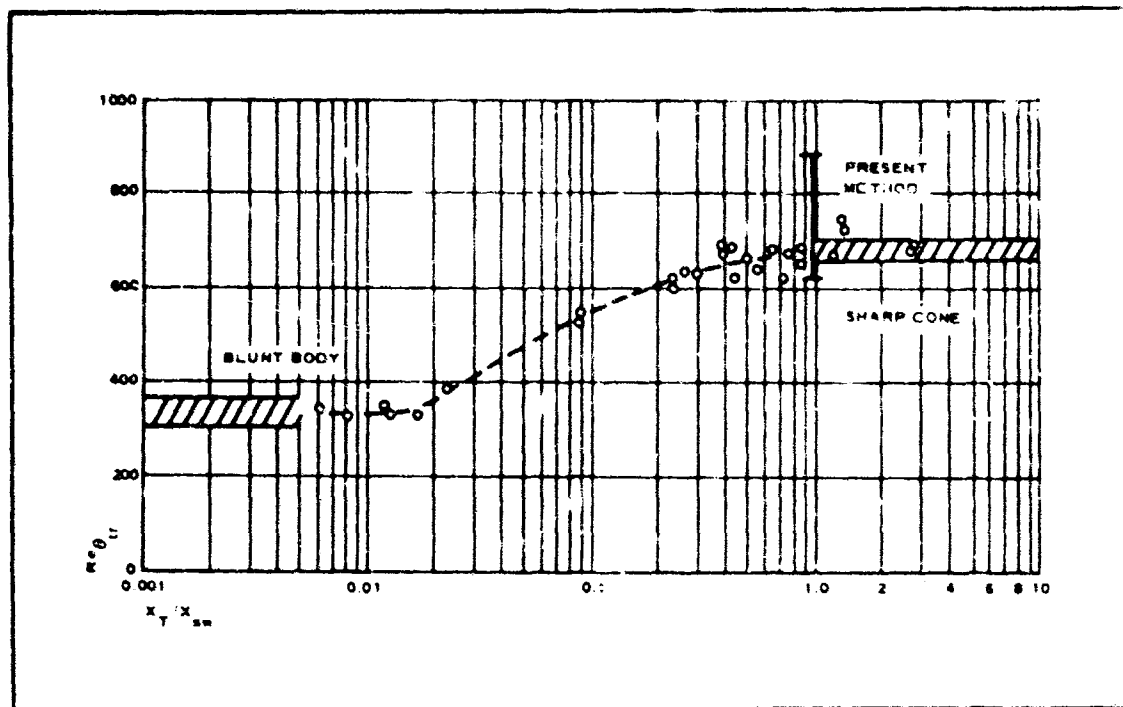
Figure 43 - Boundary Layer Transition on a Blunt Cone at $M_\infty = 5.5$

APPENDIX IV

VISCOUS WAKE ANALYSIS

1. GENERAL

An integral method of solution was applied to the problem of determining
the properties of both laminar and turbulent viscous wakes, particularly
to the problem of the wake flow preceding a trailing aerodynamic de-
celerator. The important assumptions contained in the theory are as
follows:

1. The fluid is thermally and calorically perfect,
   and there are no chemical reactions or other real
   gas phenomena.

2. Prandtl number is unity ($Pr = 1$).

3. Prandtl's concept of viscous flow phenomena is
   valid for the high-speed compressible wake in
   such a way that gradients in the streamwise or
   axial direction are much smaller than those nor-
   mal to the wake axis, and boundary layer type
   equations can be used.

4. The details of the base flow and free shear layer
   regions can be largely ignored. Thus, the region
   of validity for the present analysis must be con-
   sidered to extend from somewhere in the vicinity
   of the wake neck or further downstream and on
   down into the far wake.

5. Effects due to the existence of an external pressure
   gradient are negligible.

By using these five assumptions, the momentum integral equation can be
written as

$$\rho_1 u_1^2 (\pi \theta_1^2) = 2\pi \int_0^\delta \rho u(u_1 - u) r dr = \text{constant with respect to X} . \quad (53)$$

Here, θ is the momentum thickness; Equation 53 simply states that the
wake momentum defect is constant in the axial direction.

By ignoring the details of the base flow and shear layer regions and as-
suming that no external work is done on the wake fluid in these regions,
then the constant in Equation 53 can be evaluated by equating the mo-
mentum defect of the boundary layer at the base of the forebody to the
momentum defect of the wake. This can be stated mathematically as

$$\rho_B u_B^2 (\pi \theta_B D) = \rho_1 u_1^2 (\pi \theta_1^2) , \quad (54)$$

where the subscript 1 refers to properties associated with the outer edge of the wake, and the subscript B refers to properties at the base of the vehicle, where the boundary layer separates. p_B and u_B are inviscid properties, while D is the forebody base diameter.

The continuity and momentum equations governing this laminar axisymmetric high-speed wake problem are

$$\frac{1}{r}\frac{\partial}{\partial r}(\rho r v) + \frac{\partial}{\partial X}(\rho u) = 0$$

$$\rho u \frac{\partial u}{\partial X} + \rho v \frac{\partial u}{\partial r} = \frac{1}{r}\frac{\partial}{\partial r}(r\mu \frac{\partial u}{\partial r})$$

$$\frac{\partial p}{\partial r} = 0 . \tag{55}$$

Here, v is the velocity in the radial direction, r; u is the velocity in the axial direction, X. For laminar flow, the properties in Equation 55 are the conventional local properties. For turbulent flow u, v, p, and ρ must be interpreted as time-averaged quantities (as opposed to the fluctuating component of each of these properties). The viscosity, μ, takes a different form for laminar flow than for turbulent flow. The axial direction momentum equation can be expanded and expressed as

$$\rho u \frac{\partial u}{\partial X} + \rho v \frac{\partial u}{\partial r} = \frac{\partial}{\partial r}(\mu \frac{\partial u}{\partial r}) + \frac{1}{r}\mu \frac{\partial u}{\partial r} . \tag{56}$$

To solve this equation, the Dorodnitzyn transformation is introduced where

$$n dn = \frac{\rho}{\rho_1} r dr . \tag{57}$$

In this new X, n coordinate system, the transformed wake thickness Δ is found through integration so that

$$\Delta^2 = 2\int_0^\delta \frac{\rho}{\rho_1} r dr . \tag{58}$$

Δ is termed the wake thickness but is really the wake radius. A non-dimensional variable, $\eta = n/\Delta$, then can be introduced so that $\eta = 0$ at the center of the wake and $\eta = 1$ at the outer edge where $Y = \delta$. In the X, η coordinate system, it is assumed that the velocity profile can be expressed as

$$\frac{u}{u_1} = \sum_{i=0}^{4} a_i \eta^i . \tag{59}$$

The boundary conditions to be used then are as follows.

1. At the centerline of the wake, $Y = \eta = 0$ and $u = u_0$.

2. At the centerline of the wake, $Y = \eta = 0$ and $\dfrac{\partial u}{\partial Y} = \dfrac{\partial u}{\partial \eta} = 0$.

3. At the outer edge of the wake, $Y = \delta$ or $\eta = 1$, $u = u_1$.

4. At the outer edge of the wake, $Y = \delta$ or $\eta = 1$, $\dfrac{\partial u}{\partial Y} = \dfrac{\partial u}{\partial \eta} = 0$.

5. At the centerline, the axial direction momentum equation applies.

6. At the outer edge of the wake, $Y = \delta$ or $\eta = 1$, $\dfrac{\partial^2 u}{\partial Y^2} = \dfrac{\partial^2 u}{\partial \eta^2} = 0$.

The first boundary condition yields

$$a_0 = \frac{u_0}{u_1}.$$

Boundary conditions 2 through 4 yield

$$a_1 = 0$$

$$a_0 + a_1 + a_2 + a_3 + a_4 = 1$$

$$2a_2 + 3a_3 + 4a_4 = 0 \tag{60}$$

Boundary condition 5 can be evaluated only after the axial direction momentum equation is transformed. This leads to

$$\rho u \frac{\partial u}{\partial X} + \rho v \left(\frac{\rho}{\rho_1} \frac{r}{n} \right) \frac{\partial u}{\partial n} = \frac{\rho u_1}{\rho_1} \frac{r}{n} \frac{\partial}{\partial n} \left(\frac{\rho \mu}{\rho_1 u_1} \frac{r}{n} \frac{\partial u}{\partial n} \right) + \frac{1}{n} \frac{\rho u}{\rho_1} \frac{\partial u}{\partial n} .$$

Because of the symmetry of the problem, all gradients in the radial direction are zero on the wake centerline; thus, on the centerline the relation

$$\frac{dn}{dr} = \frac{\rho}{\rho_1} \frac{r}{n}$$

leads to

$$n^2 = \frac{\rho_0}{\rho_1} r^2 .$$

Evaluating the above momentum equation at the wake centerline results in

$$\rho_1 u_0 \frac{du_0}{dX} = \mu_1 \frac{\rho_1}{\rho_0} \frac{\partial}{\partial n}\left(\frac{\rho\mu}{\rho_1\mu_1} \frac{\partial u}{\partial n}\right) + \mu_1 \frac{\rho_1}{\rho_0}\left(\frac{\rho\mu}{\rho_1\mu_1}\right)\frac{1}{n}\frac{\partial u}{\partial n}$$

or

$$\rho_1 u_0 \frac{du_0}{dX} = \mu_1 \frac{\rho_1}{\rho_0}\left(\frac{\rho\mu}{\rho_1\mu_1}\right)_0 \left[\frac{\partial^2 u}{\partial n^2} + \left(\frac{1}{n}\frac{\partial u}{\partial n}\right)\right]_0 .$$

Substituting from Equation 59 results in

$$\rho_1 u_0 \frac{du_0}{dX} = \frac{\mu_0 u_1}{\Delta^2} 4a_2 . \tag{61}$$

Thus,

$$4a_2 = \frac{u_0}{u_1}(\Delta^2) \left(\frac{\rho_1}{\mu_0}\right)\frac{du_0}{dX} ,$$

and a_2 can be expressed as

$$a_2 = \frac{\xi}{4} . \tag{62}$$

where

$$\xi = \frac{u_0}{u_1}(\Delta^2) \left(\frac{\rho_1}{\mu_0}\right)\frac{du_0}{dX} . \tag{63}$$

The first five boundary conditions thus yield the following values for the coefficients a_0, a_1, . . .

$$a_0 = \frac{u_0}{u_1}$$

$$a_1 = 0$$

$$a_2 = \frac{\xi}{4}$$

$$a_3 = 4\left(1 - \frac{u_0}{u_1}\right) - \frac{\xi}{2} = -\frac{\xi}{3}$$

$$a_4 = -2\left(1 - \frac{u_0}{u_1}\right) + \frac{\xi}{4} = \frac{\xi}{8} . \tag{64}$$

The velocity profile in the transformed plane then becomes

$$\frac{u - u_0}{u_1} = \frac{\xi}{4}(\eta^2 - 2\eta^3 + \eta^4) + (1 - \frac{u_0}{u_1})(4\eta^3 - 3\eta^4) .$$

When boundary condition 6 is used, it can be shown that

$$\frac{\xi}{24} = \left(1 - \frac{u_0}{u_1}\right) ,$$

The velocity profile then becomes

$$\frac{u}{u_1} = (6\eta^2 - 8\eta^3 + 3\eta^4 - 1)\frac{\xi}{24} + 1 . \tag{65}$$

For $\xi = 24$, then $u_0 = 0$ and $X = 0$; for $\xi = 0$, then $u_0 = 1$ and $X = \infty$.

With the velocity profile now known as a function of ξ, the next step is to relate ξ and X. This can be done by using Equation 63. However, to do this a form for the viscosity coefficient, μ_0, must be specified. Its form will depend on whether the flow is laminar or turbulent; the evaluation of the relationship between ξ and X will be discussed in the next section, where the various special cases are treated.

It is of interest though, before turning to the solution of the energy equation, to consider the relationship between θ and Δ. This can be done by transforming Equation 53 so that

$$\frac{\theta^2}{\Delta^2} = 2 \int_0^1 \frac{u}{u_1}\left(1 - \frac{u}{u_1}\right)\eta\, d\eta . \tag{66}$$

Substituting for $\frac{u}{u_1}$ in terms of η and ξ, there results upon integration

$$\frac{\theta^2}{\Delta^2} = \frac{\xi}{120} - \frac{11\xi^2}{60,480} \approx \frac{\xi}{120} - \frac{\xi^2}{5500} . \tag{67}$$

Where there is no pressure gradient in the wake, θ is constant and can be evaluated from Equation 64; then Equation 67 is a relationship between Δ and ξ. The location of the wake neck can be sought by differentiating Equation 67 with respect to X. This results in

$$-2 \frac{\theta^2}{\Delta^3} \frac{d\Delta}{dX} = \left(\frac{1}{120} - \frac{2\xi}{5500}\right)\frac{d\xi}{dX} .$$

At the wake neck,

$$\frac{d\Delta}{dX} = 0.$$

However, $d\xi/dX \neq 0$; thus, the location of wake neck is determined from the condition

$$\frac{2\xi}{5500} = \frac{1}{120} \text{ or } \xi = 22.9. \tag{68}$$

At this location, the centerline velocity then will be

$$\frac{u_0}{u_1} = 0.045, \tag{69}$$

and the wake thickness or radius is

$$\left(\frac{\Delta}{\theta}\right)_{neck} = 3.24. \tag{70}$$

Although the above results are of interest, they are only approximate since in the neck region the effects of pressure gradient, in both the normal and axial directions, may be important.

In the energy equation, the high-speed compressible wake can be written as

$$\rho u \frac{\partial h}{\partial X} + \rho v \frac{\partial h}{\partial r} = \frac{1}{r} \frac{\partial}{\partial r}\left(\frac{k}{c_p} r \frac{\partial h}{\partial r}\right) + \mu \left(\frac{\partial u}{\partial r}\right)^2 . \tag{71}$$

Multiplying the axial direction momentum equation by u and adding it to the above results in

$$\rho u \frac{\partial H}{\partial X} + \rho v \frac{\partial H}{\partial r} = \frac{1}{r} \frac{\partial}{\partial r}\left(\frac{\mu}{Pr} r \frac{\partial H}{\partial r}\right) + \frac{1}{r} \frac{\partial}{\partial r}\left[\left(1 - \frac{1}{Pr}\right)\mu u r \frac{\partial u}{\partial r}\right]. \tag{72}$$

In either one of these equations, the properties must be considered as local fluid properties for laminar flow and as time-averaged properties for turbulent flow.

For $Pr = 1$, a solution to the above energy equation in terms of total enthalpy is

$$H = c_1 u + c_2,$$

where the constants c_1 and c_2 are determined from the boundary conditions

$$u = u_1, \quad H = H_1$$

$$u = u_0, \quad H = H_0 \tag{73}$$

The total enthalpy profile thus can be expressed as

$$H_1 - H = (H_1 - H_0) \frac{u_1 - u}{u_1 - u_0}$$

or

$$\frac{H_1 - H}{H_1 - H_0} = \frac{1 - \dfrac{u}{u_1}}{1 - \dfrac{u_0}{u_1}}. \tag{74}$$

H_0 can be determined from the condition that the total enthalpy defect is constant in the wake and is equal to that of the vehicle boundary layer at its base. For the wake, the total enthalpy defect is

$$\rho_1 u_1 H_1 \left(\pi \theta_{T_1}^2 \right) = 2\pi \int_0^\delta \rho u (H_1 - H) r \, dr \tag{75}$$

or transforming

$$\frac{\theta_{T_1}^2}{\Delta^2} = 2 \int_0^1 \frac{u}{u_1} \left(1 - \frac{H}{H_1} \right) \eta \, d\eta. \tag{76}$$

Substituting from Equation 74 and integrating leads to

$$\theta^2_{T_1} = \frac{1 - \dfrac{H_0}{H_1}}{1 - \dfrac{u_0}{u_1}} \theta^2_1$$

or

$$\frac{H_0}{H_1} = 1 - \frac{\theta^2_{T_1}}{\theta^2_1} \left(1 - \frac{u_0}{u_1} \right). \tag{77}$$

For the vehicle boundary layer, the total enthalpy defect is

$$\rho_s u_s H_s \left(\pi D \theta_{T_s} \right) = \pi D \int_0^{\delta_s} \rho u (H_s - H) dY, \tag{78}$$

and for $Pr = 1$, this can be reduced to

$$\theta_{T_s} = \left(1 - \frac{h_w}{H_1} \right) \theta_s, \tag{79}$$

where h_w is based on the forebody skin temperature at the base. If the total enthalpy defect of the wake is equated to that of the vehicle boundary layer at the base,

$$\rho_1 u_1 H_1 \left(\pi \theta^2_{T_1} \right) = \rho_s u_s H_s \left(\pi D \theta_{T_s} \right) .$$

If Equations 54, 77, and 79 are substituted, then it follows that

$$\frac{\theta^2_{T_1}}{\theta^2_1} = \left(1 - \frac{h_w}{H_1} \right) \left(\frac{u_1}{u_B} \right). \tag{80}$$

Thus, knowing the velocity profile (Equation 65), the total enthalpy profile can be determined using Equations 74, 77, and 80. The static enthalpy profile readily follows.

To transform the results back into the physical X, Y coordinate system, use must be made of the expression

$$\frac{r^2}{\Delta^2} = 2\int_0^\eta \frac{\rho_1}{\rho}\eta d\eta = 2\int_0^\eta \frac{h}{h_1}\eta d\eta. \tag{81}$$

Substituting for the enthalpy profile and integrating results in

$$\frac{r^2}{\Delta^2} = 2\left\{\frac{H_1 - H_0}{h_1\left(1 - \frac{u_0}{u_1}\right)}\left[\left(\frac{3}{2}\eta^4 - \frac{8}{5}\eta^5 + \frac{1}{2}\eta^6 - \frac{\eta^2}{2}\right)\frac{\xi}{24} + \frac{\eta^2}{2}\right] + \right.$$

$$\left[\frac{H_1}{h_1} - \frac{H_1 - H_0}{h_1\left(1 - \frac{u_0}{u_1}\right)}\right]\frac{\eta^2}{2} - \frac{u_1^2}{2h_1}\left[\frac{\eta^2}{2} + \frac{\xi}{12}\left(\frac{3}{2}\eta^4 - \frac{8}{5}\eta^5 + \frac{\eta^6}{2} - \frac{\eta^2}{2}\right)\right] -$$

$$\left. \frac{u_1^2}{2h_1}\left[\frac{\xi^2}{24^2}\left(\frac{\eta^2}{2} - 3\eta^4 + \frac{16}{5}\eta^5 + 5\eta^6 - \frac{96}{7}\eta^7 + \frac{100}{8}\eta^8 - \frac{48}{9}\eta^9 + \frac{9}{10}\eta^{10}\right)\right]\right\}. \tag{82}$$

Thus, except for the relationship between ξ and X, the necessary equations for determining the properties of a high-speed compressible wake have been derived using an integral technique and the Dorodnitzyn transformation. For a given X/D, the velocity and total enthalpy profiles in the transformed coordinate system are given by Equations 65 and 74 in terms of H_0, the centerline total enthalpy, and ξ, a form parameter. H_0 can be determined from Equations 77 and 80 and ξ as will be discussed in the next section. The transformed wake thickness or radius can be determined from Equation 67 and the physical coordinate r from Equation 82. To obtain numerical results, it is only necessary that the inviscid flow field be specified, and that an estimate be made of the vehicle boundary layer momentum thickness. Although some of the derived equations may seem rather cumbersome in terms of carrying out numerical calculations, the results are of an algebraic nature and in principle can be readily applied.

It should be re-emphasized, however, that the preceding analysis has ignored the details of the free shear layer and base flow regions. The results obtained thus must be considered as approximate; their range of applicability is certainly limited to the region downstream of the wake neck.

2. CONVENTIONAL LAMINAR WAKE

To evaluate Equation 63 and to obtain ξ as a function of X, it is necessary to specify a relation for the viscosity coefficient. For laminar flow, the viscosity can be assumed to have a linear dependence on the fluid temperature, i.e., $\mu/RT = $ constant. Since in this analysis the radial pressure gradient is assumed to be zero, then from the equation of state it can be

shown that $\rho\mu$ is constant with respect to r and that $\rho\mu = \rho_1\mu_1$. Equation 63 then can be written as

$$\xi = \frac{u_0}{u_1}(\Delta^2)\left(\frac{\rho_0}{\mu_1}\right)\frac{du_0}{dX} \tag{83}$$

Since

$$\frac{u_0}{u_1} = 1 - \frac{\xi}{24}$$

then

$$\frac{du_0}{dX} = -\frac{u_1}{24}\frac{d\xi}{dX} .$$

Furthermore, the relationship between Δ^2 and ξ is known from Equation 67. Substituting these results into Equation 83 results in

$$\frac{\xi^2}{120} - \frac{\xi^3}{5500} = -\left(1 - \frac{\xi}{24}\right)\frac{\rho_0}{\mu_1}\frac{u_1}{24}\theta^2\frac{d\xi}{dX} . \tag{84}$$

Since ρ_0 has not been specified in terms of ξ or X, these two variables are not yet uniquely related to each other. To do this, attention must be given to solving the energy equation.

Now the centerline density, ρ_0, can be expressed as

$$\rho_0 = \frac{P_1}{RT_0} = \frac{\gamma}{\gamma_{-1}}\frac{P_1}{h_0} .$$

The static enthalpy can be related to the total enthalpy as

$$h_0 = H_0 - \frac{u_0^2}{2} .$$

When Equation 77 is used, ρ_0 can be expressed as

$$\rho_0 = \frac{\gamma}{\gamma - 1}\frac{P_1}{H_1 - \frac{\theta_{T_1}^2}{\theta_1^2}H_1\left(1 - \frac{u_0}{u_1}\right) - \frac{u_0^2}{2}} . \tag{85}$$

Since the relationship between u_0/u_1 and ξ is known, then Equation 84 takes the form

$$\frac{\xi^2}{120} - \frac{\xi^3}{5500} = -\left(1 - \frac{\xi}{24}\right)\frac{u_1}{24}\frac{\theta_1^2 P_1}{\mu_1}\frac{\gamma}{\gamma - 1}\frac{\frac{d\xi}{dX}}{H_1 - \frac{\theta_{T_1}^2}{\theta_1^2}\frac{\xi}{24}H_1 - \frac{u_1^2}{2}\left(1 - \frac{\xi}{24}\right)^2}.$$

After rearrangement, this takes the form

$$X = -\int_{24}^{\xi}\frac{\left[\left(1 - \frac{\xi}{24}\right)\frac{u_1}{\mu_1}\right]\left(\frac{P_1\theta_1^2}{24}\right)\left(\frac{\gamma}{\gamma - 1}\right)}{\left(\frac{\xi^2}{120} - \frac{\xi^3}{5500}\right)\left[H_1 - \frac{\theta_{T_1}^2}{\theta_1^2}H_1\frac{\xi}{24} - \frac{u_1^2}{2}\left(1 - \frac{\xi}{24}\right)^2\right]}d\xi. \quad (86)$$

Here, X is measured from where physically the wake centerline velocity is zero, i.e., the rear stagnation point. For known flow conditions, Equation 86 gives the variation of ξ with X. When the results of Item 1 are used, a complete solution for the wake flow can be obtained.

Equation 36 can be recast in form by noting that the bracketed term in the denominator can be written as

$$H_1\left[1 - \frac{\theta_{T_1}^2}{\theta_1^2}\frac{\xi}{24} - \left(1 + \frac{\gamma - 1}{2}M_1^2\right)^{-1}\left(\frac{\gamma - 1}{2}M_1^2\right)\left(1 - \frac{\xi}{24}\right)^2\right],$$

and that

$$\frac{u_1 P_1}{\mu_1}\frac{1}{H_1}\frac{\gamma}{\gamma - 1} = \frac{\rho_1 u_1}{\mu_1}\left(\frac{h_1}{H_1}\right).$$

The following then results:

$$\frac{X}{\theta}\left(\frac{1}{R^{\circ}\theta}\right) =$$

$$-\int_{24}^{\xi}\frac{\frac{1}{24}\left(1 - \frac{\xi}{24}\right)}{\frac{\xi^2}{120} - \frac{\xi^3}{5500}\left[\left(1 + \frac{\gamma - 1}{2}M_1^2\right)\left(1 - \frac{\theta_{T_1}^2}{\theta_1^2}\frac{\xi}{24}\right) - \frac{\gamma - 1}{2}M_1^2\left(1 - \frac{\xi}{24}\right)^2\right]}d\xi.$$

$$(87)$$

where

$$Re_\theta = \frac{\rho_1 u_1 \theta}{\mu_1}$$

and is based on wake edge conditions.

Two special cases are of interest. One is that of an adiabatic forebody wall such that $\theta_{T_1}^2 / \theta_T^2 = 0$. In that case, Equation 87 becomes

$$\frac{Re_X}{Re_\theta^2} = -\int_{24}^{\xi} \frac{\frac{1}{24}\left(1 - \frac{\xi}{24}\right)}{\left(\frac{\xi^2}{120} - \frac{\xi^3}{5500}\right)\left(1 + \frac{\gamma-1}{2} M_1^2 \frac{\xi}{12} - \frac{\gamma-1}{2} M_1^2 \frac{\xi^2}{576}\right)} \, d\xi. \qquad (88)$$

The second case is that for a cold wall where

$$\frac{\theta_{T_1}^2}{\theta_T^2} = 1.$$

Here, Equation 87 becomes

$$\frac{Re_X}{Re_\theta^2} = -\int_{24}^{\xi} \frac{1}{\left(\frac{\xi^2}{120} - \frac{\xi^3}{5500}\right)\left(1 + \frac{\gamma-1}{2} M_1^2 \frac{\xi}{24}\right)} \frac{d\xi}{24}. \qquad (89)$$

Equations 88 and 89 indicate that for ξ small, then

$$X \propto \xi^{-1}.$$

Since $\delta \approx \Delta$ for ξ small and similarly

$$\Delta^2 \propto \xi^{-1}.$$

Then,

$$\delta \propto X^{\frac{1}{2}}. \qquad (90)$$

ξ small corresponds to the far wake region, and this square root dependence on X is in agreement with experimental data (Reference 13). It similarly can be shown that

$$1 - \frac{u_0}{u_1} \propto X^{-1}, \tag{91}$$

and

$$1 - \frac{H_0}{H_1} \propto X^{-1}. \tag{92}$$

This also is in agreement with experimental data.

3. CYLINDRICAL LAMINAR WAKE

The nature of the laminar axisymmetric wake in the presence of a small diameter wire or cable at its centerline is such that the wake will be approximately cylindrical (or at least will grow very slowly) and will have a zero centerline velocity caused by the no-slip condition at the cable.

An approximate solution corresponding to this case can be obtained from the results of Item 1 by noting that u_0/u_1 equal to zero is equivalent to ξ equal to 24. Thus, the properties of a cylindrical wake can be obtained by setting ξ equal to 24 in the previously derived equations. ξ will not depend on X for this simplified case since there will be complete similarity between the radial profiles at all X direction stations. For this case, the wake velocity profile is given by

$$\frac{u}{u_1} = 6\eta^2 - 8\eta^3 + 3\eta^4, \tag{93}$$

and the transformed wake thickness, by

$$\frac{\Delta}{\theta} = 3.24, \tag{94}$$

where θ is determined from equating $\rho_1 u_1^2 \theta_1$ to the momentum defect of the forebody boundary layer. For a slender body with a zero axial pressure gradient in the wake region, θ_1 is constant, and thus Δ also is a constant. The wake thus has a constant diameter and is cylindrically shaped. If there is a favorable pressure gradient, then the wake diameter will increase in the downstream direction due to the decreasing gas density. Here, the momentum defect, $\rho_1 u_1^2 \theta_1$, is constant with axial position, and Δ increases as $\rho_1 u_1^2$ decreases.

For such a cylindrical wake, the solution to the energy equation (Pr = 1) is similar to that given in Item 1 and can be written as

$$\frac{H}{H_1} = \left(1 - \frac{h_w}{H_1}\right) \frac{u}{u_i} + \frac{h_w}{H_1}, \tag{95}$$

where h_w is the enthalpy of the gas at a temperature equal to that of the tow cable or riser line. With the velocity and enthalpy profiles known, the wake characteristics can be completely determined. The transformed and physical coordinates then can be related using Equation 82 for $\xi = 24$ with the result that

$$\frac{r^2}{\Delta^2} = 2\left[\frac{(H_1 - h_w)}{h_1}\left(\frac{3}{2}\eta^4 - \frac{8}{5}\eta^5 + \frac{1}{2}\eta^6\right) + \frac{1}{2}\frac{h_w}{h_1}\eta^2 - \frac{u_1^2}{2h_1}\left(6\eta^6 - \frac{96}{7}\eta^7 + \frac{100}{8}\eta^8 - \frac{48}{9}\eta^9 + \frac{9}{10}\eta^{10}\right)\right]. \tag{96}$$

When the above equation is applied at $\eta = 1$, the actual wake radius or thickness can be related to the transformed thickness such that

$$\frac{\delta^2}{\Delta^2} = 0.72 + 0.08\frac{H_1}{h_1} + 0.20\frac{h_w}{h_1}. \tag{97}$$

With the use of Equation 54, it can be further shown that

$$\left(\frac{\delta}{D}\right)^2 = 7.56\left(1 + 0.111\frac{H_1}{h_1} + 0.278\frac{h_w}{h_1}\right)\frac{\theta_s}{D}\frac{\rho_s u_s^2}{\rho_1 u_1^2}. \tag{98}$$

With Equations 93 through 98, the solution is complete with the properties being clearly specified in terms of the forebody boundary layer characteristics and the inviscid properties at the edge of the viscous wake. In this approximate solution, the variation in properties with X is controlled by the change in the inviscid flow field with X since the solution is effectively a constant ξ solution, and there is no meaningful relationship between ξ and X (except that ξ is constant).

4. TURBULENT WAKE

In Item 1, the solution for the viscous wake profiles was obtained except for relating ξ, the form parameter, to X. Starting with the equation for the turbulent viscosity coefficient

$$\mu_0 = K\Delta\rho_1 u_1\left(\frac{\rho_0}{\rho_1}\right)^m\left[1 - n - (-1)n\left(\frac{\rho_0}{\rho_1}\right)^p\left(\frac{u_0}{u_1}\right)\right], \tag{99}$$

as given in Section III, Item 3c, and where m, n, and p are defined for the various viscosity models (see Table VIII).

TABLE VIII - RELATIONSHIP OF

VARIOUS VISCOSITY MODELS

Viscosity model	μ_0	m	n	p
1	$K\Delta \rho_0 u_0$	1	1	0
2	$K\Delta(\rho_1 u_1 - \rho_0 u_0)$	0	0	1
3	$K\Delta \rho_1(u_1 - u_0)$	0	0	0
4	$K\Delta \rho_0(u_1 - u_0)$	1	0	0

Substituting Equation 99 into Equation 63 results in

$$\xi = \frac{u_0}{u_1} \Delta \frac{1}{K\left(\frac{\rho_0}{\rho_1}\right)^m \left[1 - n - (-1)^n \left(\frac{\rho_0}{\rho_1}\right)^p \left(\frac{u_0}{u_1}\right)\right]} d\frac{u_0}{u_1}.$$

Introducing the relationship between u_0/u_1 and ξ leads to

$$\xi = \left(1 - \frac{\xi}{24}\right)\Delta \frac{1}{K\left(\frac{\rho_0}{\rho_1}\right)^m \left[1 - n - (-1)^n \left(\frac{\rho_0}{\rho_1}\right)^p \left(1 - \frac{\xi}{24}\right)\right]} - \frac{1}{24}\frac{d}{dX}.$$

When Δ is replaced through the relationship between Δ and θ, it follows that

$$\xi = -\frac{\theta}{K}\frac{1}{24}\frac{\left(1 - \frac{\xi}{24}\right)}{\sqrt{\frac{\xi}{120} - \frac{\xi^2}{5500}}} \frac{1}{\left(\frac{\rho_0}{\rho_1}\right)^m \left[1 - n - (-1)^n \left(\frac{\rho_0}{\rho_1}\right)^p \left(1 - \frac{\xi}{24}\right)\right]} \frac{d\xi}{dX}.$$

After rearrangement, the integrable form is finally obtained:

$$\frac{K}{\theta} dX = -\frac{1}{24}\frac{\left(1 - \frac{\xi}{24}\right)}{\sqrt{\frac{\xi}{120} - \frac{\xi^2}{5500}}} \frac{\left(\frac{\rho_1}{\rho_0}\right)^{m+p}}{\left[(1 - n)\left(\frac{\rho_1}{\rho_0}\right)^p - (-1)^n\left(1 - \frac{\xi}{24}\right)\right]} \frac{d\xi}{\xi}. \quad (100)$$

Integration is particularly simple for turbulent viscosity coefficient Model 1 where $m = n = p = 0$. The above then becomes

$$\frac{K}{\theta} \int_{X_0}^{X} dX = - \int_{\xi_0}^{\xi} \frac{\left(1 - \frac{\xi}{24}\right)}{\xi^2 \sqrt{\frac{\xi}{120} - \frac{\xi^2}{5500}}} \, d\xi .$$ (101)

Here, X_0 is the point where the turbulent wake begins, and ξ_0 is the value of ξ at that point. If the wake is initially laminar, then X_0 is the physical location of the transition point, and ξ_0 equals $\xi_{laminar}$ at transition. Integrating Equation 101 results in

$$\frac{K}{\theta} (x - x_0) = \left(\frac{80}{\xi^2} - \frac{6.5}{\xi} \right) \sqrt{\frac{\xi}{120} - \frac{\xi^2}{5500}} \Bigg|_{\xi_0}^{\xi} .$$ (102)

Since θ was considered constant in Equations 101 and 102, then these equations are limited to regions of zero-pressure gradient. Equation 101 is not so limited.

Another case of interest is when Model 4 is used for the turbulent viscosity coefficient. This is the same model used by Less and Hromas (Reference 50). In this case, $n = p = 0$ but $m = 1$, and it is necessary to evaluate ρ_1 / ρ_0 before ξ and X can be related. The value of ρ_0 is given by Equation 85. This equation can be rewritten as

$$\frac{\rho_0}{\rho_1} = \frac{\gamma}{\gamma - 1} \frac{1}{\frac{\gamma}{\gamma - 1} \frac{T_{0_1}}{T_1} - \frac{\theta_{T_1}^2}{\theta_1^2} \frac{\gamma}{\gamma - 1} \frac{T_{0_1}}{T_1} \frac{\xi}{24} - \frac{\gamma}{2} M_1^2 \left(1 - \frac{\xi}{24}\right)^2} .$$ (103)

Thus,

$$\frac{\rho_1}{\rho_0} = 1 + \frac{\gamma - 1}{2} M_1^2 - \left(1 + \frac{\gamma - 1}{2} M_1^2\right) \frac{\theta_{T_1}^2}{\theta_1^2} \frac{\xi}{24} - \frac{(\gamma - 1)}{2} M_1^2 \left(1 - \frac{\xi}{24}\right)^2 .$$ (104)

When this value is substituted in Equation 100, there results for this case, i.e., using Model 4

$$\frac{K}{\theta} dX =$$

$$-\frac{\left(1 - \frac{\xi}{24}\right)}{\sqrt{\frac{\xi}{120} - \frac{\xi^2}{5500}}}\left[1 + \frac{\gamma - 1}{2} M_1^2 - \left(1 + \frac{\gamma - 1}{2} M_1^2\right)\frac{\theta_{T_1}^2}{\theta_1^2}\frac{\xi}{24} - \frac{(\gamma - 1)}{2} M_1^2\left(1 - \frac{\xi}{24}\right)^2\right]\frac{d\xi}{\xi^2}.$$

(105)

For an adiabatic forebody wall, $\theta_{T_1}^2$ equals zero; upon integration, the above equation becomes

$$\frac{K}{\theta}(X - X_0) = -\int_{\xi_0}^{\xi}\frac{\left(1 - \frac{\xi}{24}\right)}{\sqrt{\frac{\xi}{120} - \frac{\xi^2}{5500}}}\left[1 + \frac{\gamma - 1}{2} M_1^2\left(\frac{\xi}{12} - \frac{\gamma - 1}{2} M_1^2 \frac{\xi^2}{576}\right)\right]\frac{d\xi}{\xi^2}, \quad (106)$$

where again θ has been assumed constant, and X_0 and ξ_0 are as previously defined for turbulent flow.

Another limiting condition is that of a cold wall where $\theta_{T_1}^2 = \theta_1^2$. Using this assumption, Equation 100 takes a final form upon integration of

$$\frac{K}{\theta}(X - X_0) = -\int_{\xi_0}^{\xi}\frac{\left(1 - \frac{\xi}{24}\right)}{\sqrt{\frac{\xi}{120} - \frac{\xi^2}{5500}}}\left[1 - \frac{\xi}{24} + \frac{\gamma - 1}{2} M_1^2\left(\frac{\xi}{24} - \frac{\xi^2}{576}\right)\right]\frac{d\xi}{\xi^2},$$

(107)

where θ also has been considered a constant.

For Model 3 and ξ small, the relationship between X and ξ (Equation 75) takes the limiting form

$$X \propto \xi^{-\frac{3}{2}}.$$

Since for ξ small

$$\Delta^2 \propto \xi^{-1}$$

and

$$\delta \approx \Delta,$$

then it can be shown that

$$\delta \propto X^{\frac{1}{3}}.\tag{108}$$

This is in the limit of small ξ or large X, i. e., the far wake.

With Models 2 and 4, it can be shown that for ξ small and $\rho_0 \approx \rho_1$

$$dX \propto \frac{d\xi}{\xi^{\frac{5}{2}}}.$$

Then,

$$X \propto \xi^{-\frac{3}{2}}.$$

In a similar manner, the limiting form of

$$\delta \propto X^{\frac{1}{3}}\tag{109}$$

is arrived at for the far wake region. Furthermore, for Models 2 through 4, it also can be shown that for ξ small

$$1 - \frac{u_0}{u_1} \propto X^{-\frac{2}{3}}\tag{110}$$

and

$$1 - \frac{H_0}{H_1} \propto X^{-\frac{2}{3}}.\tag{111}$$

These also are in agreement with other investigations of the far wake.

Only in the case of Model 1 is a deviation noted from the proper asymptotic behavior as indicated by experimental data. With Model 1,

$$dX \propto \frac{d\xi}{\xi^{\frac{3}{2}}},$$

and thus

$$X \propto \xi^{-\frac{1}{2}}.$$

for ξ small. It then follows that

$$\delta \propto X^{\frac{1}{2}}, \qquad \qquad (112)$$

that

$$1 - \frac{u_0}{u_1} \propto X^{-\frac{1}{2}},$$

and that

$$1 - \frac{H_0}{H_1} \propto X^{-\frac{1}{2}}. \qquad (113)$$

This lack of a proper behavior in the limit of large X casts some doubt on the suitability of Model 1.

APPENDIX V

WIND-TUNNEL TESTING AND DATA REDUCTION

1. **GENERAL**

    All wind-tunnel tests in support of the EUREKA program were conducted in the 40-in. supersonic tunnel|Gas Dynamics Wind Tunnel, Supersonic (A)| of the von Karman Gas Dynamics Facility (VKF) at the Arnold Engineering Development Center (AEDC). The complete series is as follows:

    1. WT-I - static stability tests in support of design feasibility study described in Volume I

    2. WT-IIA - wake survey and forebody surface pressure test (axisymmetric and asymmetric forebodies)

    3. WT-IIB - parachute performance tests (axisymmetric and asymmetric forebodies)

    4. WT-III - shock shape determination (axisymmetric and asymmetric forebodies); surface pressure distribution (asymmetric forebody)

    5. WT-IV - wake centerline survey (axisymmetric forebody)

    6. WT-V - wake survey (axisymmetric forebody)

    7. WT-VI - parachute performance tests (axisymmetric and asymmetric forebodies)

    The tabulated wake survey and forebody surface pressure data are given in Volume III. The static stability tests are described in Volume I; the remaining tests are described in this appendix.

2. **WIND-TUNNEL DESCRIPTION**

    Tunnel A is a continuous, closed-circuit, variable density wind tunnel with an automatically driven, flexible plate-type nozzle and a 40- by 40-in. test section. The tunnel operates from Mach 1.5 to 6 at maximum stagnation pressures from 29 to 200 psia, respectively, and stagnation temperatures up to 300 F ($M_\infty \leq 6$). Minimum operating pressures are about one-tenth the maximum at each Mach number.

3. **MODELS AND SUPPORT SYSTEM**

    Figure 29 shows the forebody models in detail. The basic Arapaho C and the Arapaho C with nose cone forebodies are axisymmetric. The blunted elliptical cone forebody has an elliptical base.

For the wake survey and parachute performance tests, the forebodies were supported with a horizontal wall-to-wall strut having a constant chord and a constant thickness. For the parachute tests, the riser line passed through the forebody and mounting strut and into a plenum tank where it was attached to the tensiometer and winch assembly. Figure 44 shows this setup.

The models were sting-mounted from the rear for the shock shape determination (WT-III).

4. INSTRUMENTATION

From calibration results, the maximum variation of tunnel centerline Mach number is about ±0.5 percent.

The tunnel stilling chamber temperature is accurate to ±3 R. The tunnel stilling pressure, p_o, was measured with transducers of 5, 15, 30, 60, 150, and 300 psid capacity that are considered accurate to within 0.3 percent of full-scale capacity.

The model base pressures were measured with 1, 5, and 15 psid capacity transducers, referenced to a near vacuum, which also are considered accurate to within 0.3 percent of the transducer capacity. The lowest base pressures were encountered at the M_∞ = 5 low Reynolds number test conditions. At these test conditions, base pressures were about 0.008 psia. The 0.3 percent accuracy of a 1 psid transducer then could introduce errors of approximately ±37.5 percent of the measured values.

The local wake pitot and static pressures were measured with transducers of the same capacity as those used for base pressure measurement. The lowest pressures and, therefore, the greatest inaccuracies were encountered at the M_∞ = 5 minimum pressure test conditions. Combined errors in the local static and pitot pressures may introduce inaccuracies of 0.2 M at M_L = 1.0. The inaccuracy, in this case, was determined using maximum errors in pressure measurements assuming (1) the local static pressure was equal to free-stream static pressure and was measured with a 1 psid transducer and (2) the pitot pressure was measured with a 5 psid transducer. Making these same assumptions at free-stream Mach number of 4, 3, and 2 and at the minimum pressure condition, inaccuracies in measuring a local Mach number of 1.0 are 0.11, 0.06, and 0.03 M_L, respectively. At the high-pressure conditions for these tests, the accuracy of measurement at M_∞ = 5, M_L = 1.0 is increased by approximately four. The lower Mach number test cases reflect a similar accuracy increase at the high-pressure test conditions.

Table IX lists the test conditions for the wake survey tests. Based on this table, the error in the measurement of the local static pressures, which are approximately equal to the free-stream static pressure and therefore are the most critical for measurement, due to the inaccuracy of a 1 psid transducer appears in the third significant digit except for the M_∞ = 5 case. The total pressures, being higher than the static pressures, then should reflect a higher degree of accuracy.
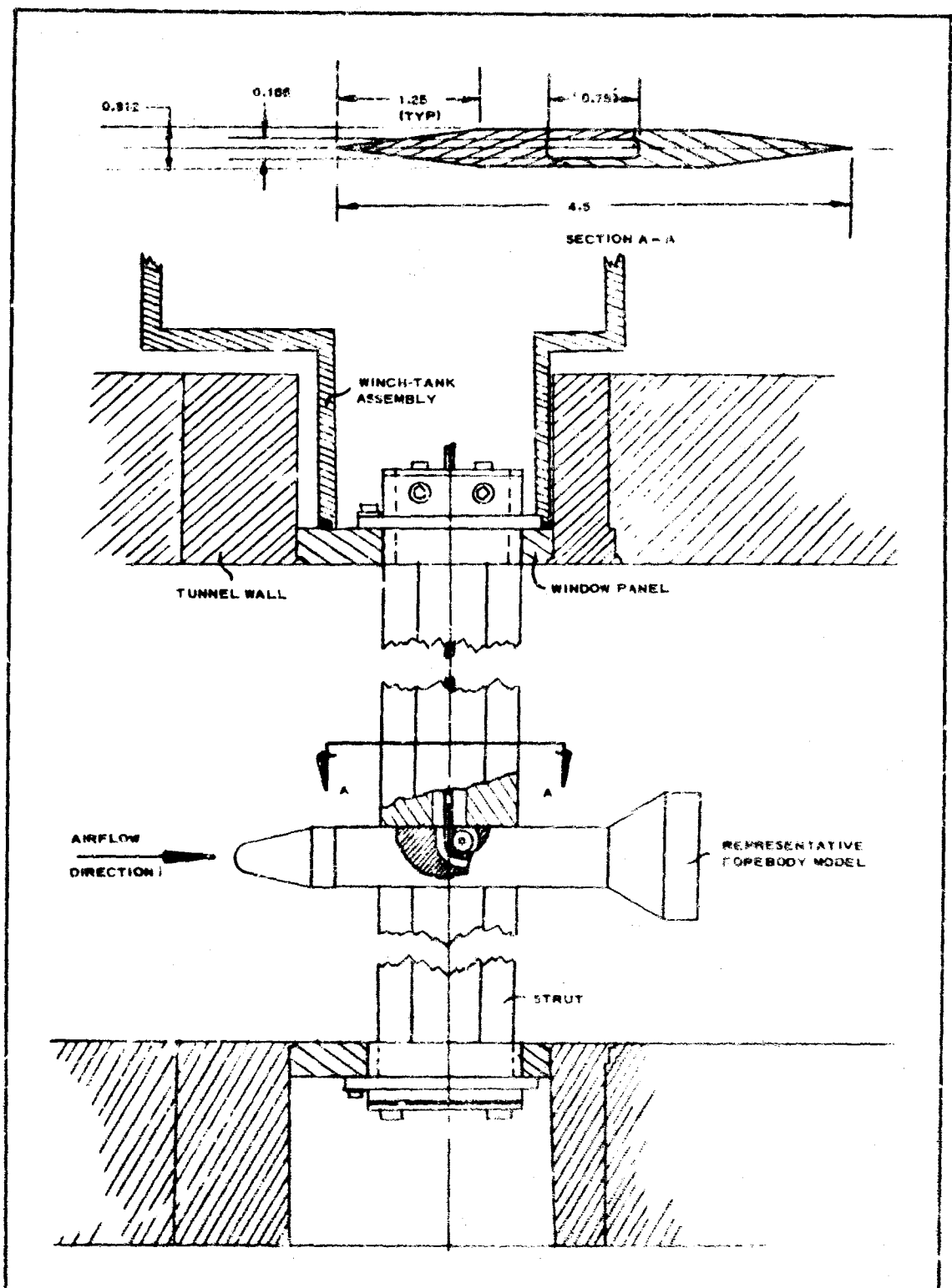
Figure 44 - Forebody Support Installation

TABLE IX - WAKE SURVEY TEST CONDITIONS SUMMARY

Forebodies	M_∞	$\dfrac{Re_\infty}{in.} \times 10^6$	P_o psia	P_∞ (psia)	T_o (deg R)	Probe stations $\dfrac{X}{D}$
Basic Arapaho C, Arapaho C with nose cone, and blunted elliptical cone*	3	0.05	2.8	0.360	581	1, 2, 3, 5, 7, 9, and 11 for all test points
	2	0.365	19.0	2.430	582	
	3	0.06	5.9	0.170	583	
	3	0.50	43.0	1.170	582	
	4	0.09	13.5	0.090	583	
	4	0.50	73.0	0.460	583	
	5	0.13	30.5	0.058	585	
	5	0.50	133.0	0.251	631	
Arapaho C with nose cone only+	2	0.06	2.8	0.360	560	0.5, 1, 2, 3, 5, 6, 7, 9, and 11 for all test points
	3	0.075	5.9	0.170	560	
	4	0.10	13.5	0.090	560	
	5	0.135	30.5	0.058	560	
Arapaho C with nose cone only‡	2	0.06	2.8	0.360	560	0.5, 1, 2, 3, 5, 6, 7, 9, and 11 for all test points
	3	0.075	5.9	0.170	560	
	4	0.10	13.5	0.090	560	
	5	0.135	30.5	0.058	560	

*WT-IIA, pitot and static rakes.

+WT-IV, pitot, static, and total temperature centerline probes.

‡WT-V, pitot rake.

The wake survey rakes used in WT-IIA and WT-V were of a cruciform design with multiple probes, thereby making it possible to obtain complete wake profiles at each X/D station without lateral or vertical movement of the rake. Table X lists locations of the probes; Figure 45 shows the probe geometry.

The centerline probes used in WT-IV have the same geometry as those used on the multiprobe rakes.

The WT-IIB parachute drag measurements were made with a 200-lb tensiometer located in the winch plenum tank. A time history of the dynamic drag output from the tensiometer was recorded on an oscillograph, and the average drag values were determined from the recorded traces. The accuracy of the 200-lb tensiometer determined from static loads is as follows.

TABLE X - WAKE SURVEY PROBE LOCATIONS

Probe number	WT-IIA Pitot rake		WT-IIA Static rake		WT-VI Pitot rake	
	Y (in.)	Z (in.)	Y (in.)	Z (in.)	Y (in.)	Z (in.)
1	-1.610	0	-0.966	0	-4.57	0
2	0	0	-0.483	0	-4.17	0
3	0.322	0	0.322	0	-3.77	0
4	0.644	0	0.805	0	-3.37	0
5	0.966	0	0	-1.449	-2.97	0
6	1.288	0	0	-0.966	-2.57	0
7	1.610	0	0	-0.483	-2.17	0
8	1.932	0	0	0.322	-1.77	0
9	2.576	0	0	0.805	-1.37	0
10	0	-2.576	0	1.289	-0.97	0
11	0	-1.610	0	1.932	-0.64	0
12	0	0.322	0	2.576	-0.32	0
13	0	0.644			2.17	0
14	0	0.966			3.37	0
15	0	1.288			0	-4.57
16	0	1.610			0	-4.17
17	0	1.932			0	-3.77
18	0	2.254			0	-3.37
19	0	2.576			0	-2.97
20	0	2.898			0	-2.57
21	0	3.220			0	-2.17
22	0	3.864			0	-1.77
23	0	4.508			0	-1.37
24	0	5.152			0	0
25					0	0.32
26					0	0.64
27					0	0.96
28					0	1.28
29					0	1.60
30					0	1.92
31					0	2.57
T1	-0.966	0			0.966	0
T2	0	-0.966			0	-0.966
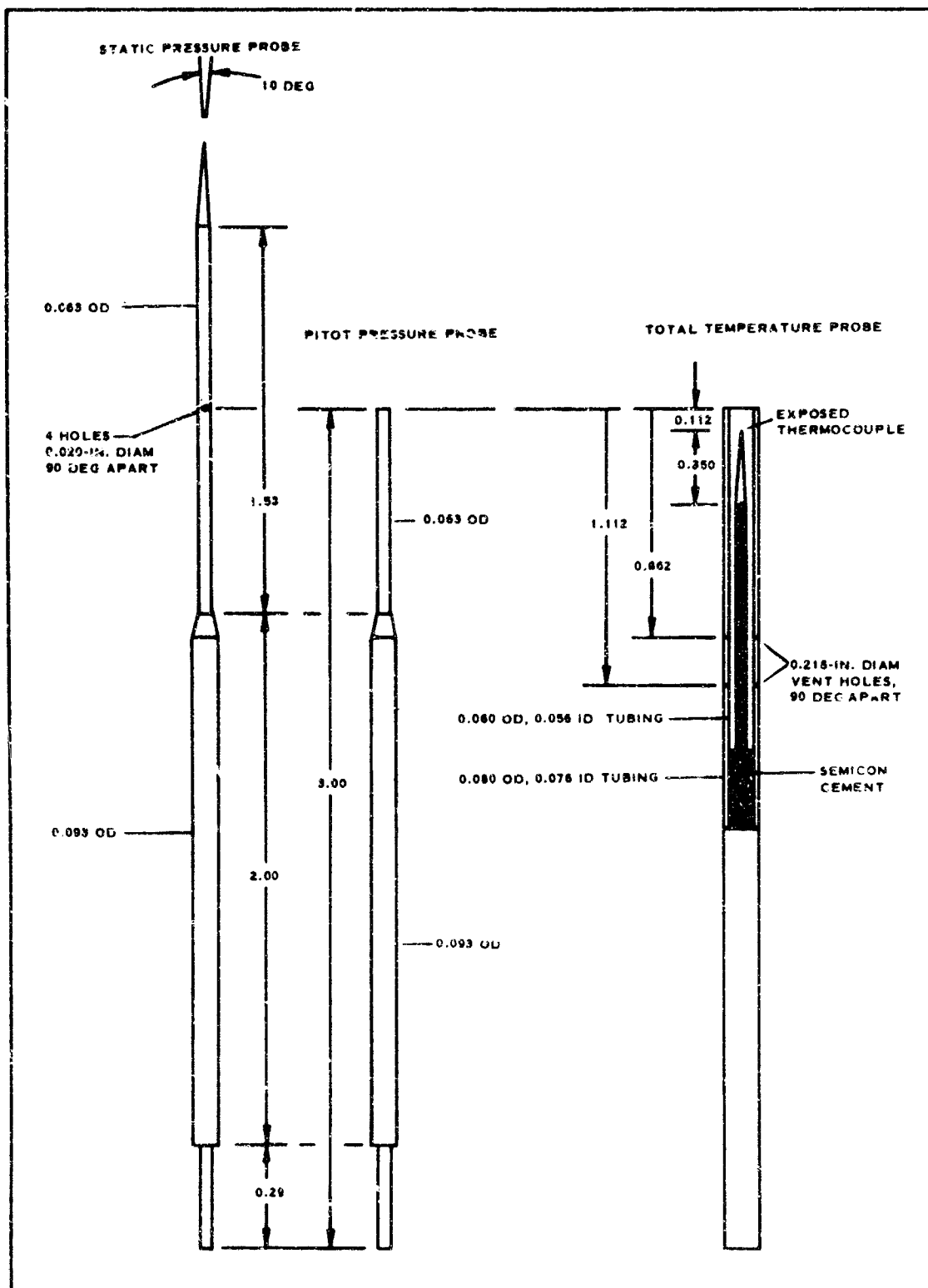
Figure 45 - Probe Geometry

Load range (pounds)	Error (pounds)
0 to 5	±0.536
6 to 15	±0.493
16 to 30	±1.290
31 to 60	±1.820

These accuracy values were for the tensiometer alone and, therefore, do not reflect any further inaccuracies caused by friction in the change-of-direction pulleys in the system.

The WT-VI drag measurements were made with a 60-lb tensiometer. The tensiometer was calibrated for both 30- and 60-lb load ranges. The change-of-direction pulleys in the system were equipped with needle bearings in place of bronze bushings as used in previous tests. Average drag values were monitored with a low response servopotentiometer, and a time history of the dynamic output from the tensiometer was recorded on an oscillograph. The accuracy of the complete drag measuring system, determined from repeated static loads applied before the test, is shown below.

Load range (pounds)	Error (pounds)
0 to 5	±0.15
6 to 15	±0.25
16 to 30	±0.33
31 to 60	±0.84

Parachute performance for both tests was monitored on two high-speed, 16-mm motion picture cameras - one for conventional motion pictures and one for schlieren photography. Still photographs, both conventional and schlieren, also were obtained.

5. PARACHUTE MODELS

PARASONIC parachutes, which have a constructed shape resembling the inflated shaped of a Hyperflo parachute (Reference Figure 28), were tested. The Hyperflo parachutes are constructed with a flat, porous roof and a truncated, conical nonporous skirt. The construction details of the PARASONIC models are given in Table XI.

6. DATA REDUCTION

a. PARASONIC Performance Data

The data obtained from the PARASONIC performance tests are given in

Tables XII and XIII. In addition to the average drag values, it was also desired to have average maximum and minimum drag values. These values were obtained from the recorded oscillographs as shown below.
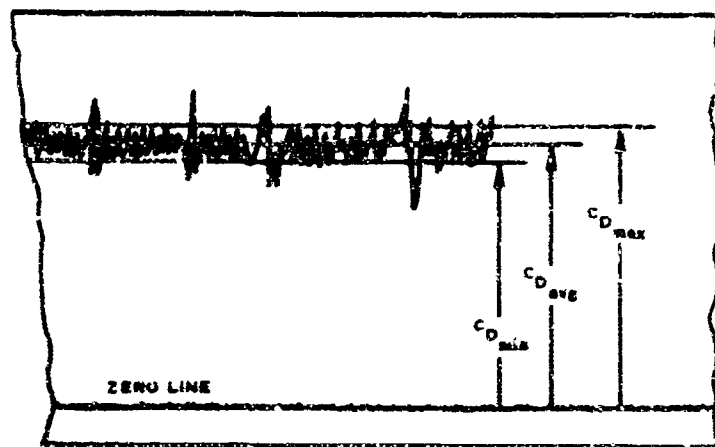
Due to improper oscillograph calibration, average maximum and minimum drag values could not be determined for the WT-VI tests. It was possible, however, to obtain the drag oscillation frequency.

The diametric and angular measurements given in Tables XII and XIII were obtained from the high-speed motion pictures.

b. **Wake Survey Tests**

During the reduction of the wake survey data acquired under WT-LA, a significant amount of data scatter was observed in formulating velocity profiles required for computation of experimental wake momentum defects (see Section III, Item 3a). The scatter was sufficient to cause considerable difficulty in evaluating experimentally achieved wake momentum defects obtained by integration of the velocity profiles. To combat this difficulty, the wake data for each test condition were smoothed by means of a multiple regression technique to permit more meaningful integration of the velocity profiles. This was achieved by expressing the family of curves formed by the velocity profile data points as a two-dimensional power series (i.e., a power series in Y/D - or Z/D - and their cross products) to produce a best statistical fit for the family of curves. The best fit uses an equation of the form

TABLE XI - MODEL DECELERATOR FABR

	Measured parameters											
Model number (580A)	λT (%)	λG (%)	D_c (in.)	D_{open} (in.)	D_i (in.)	l_s (in.)	NS	NG	WR (in.)	DR (in.)	Roof mesh
014-											
-001	4.60	10.7	6.0	3.06	5.83	12.4	12	12	0.25	1.625	HT-83-44 Nome
-002	5.50	10.5	6.0	3.04	5.64	12.5	12	12	0.25	1.688	(172-lb tensile,
-003	4.95	10.5	6.0	3.04	5.85	12.5	12	12	0.25	1.625	3.0i oz/sq yd pr
-004	5.05	10.5	6.0	3.05	5.78	12.7	12	12	0.25	1.625	coated with D156
-005	5.00	10.3	6.0	3.02	5.81	12.4	12	12	0.25	1.625	F839 polyuretha
											porosity control
											coating with D-6
											ible thermal coa
015-											
-001	4.85	7.87	6.0	2.64	5.79	12.69	12	12	0.25	1.625	MIL-T-713A, C
-002	4.75	6.70	6.0	2.43	5.70	12.50	12	12	0.25	1.750	Type S nylon lac
-003	5.12	9.28	6.0	2.86	5.75	12.38	12	12	0.25	1.750	(50-lb tensile) p
											coated on form
											D1569-F839 pol
											thane, porosity
											trolled by coati
											D-65 flexible th
											coating
016-											
-001	5.19	10.9	7.86	4.06	8.04	17.0	12	12	0.25	2.000	HT-83-44 Nome
-002	5.25	10.6	7.86	4.0	7.64	16.5	12	12	0.25	1.937	cloth (172-lb te
-003	5.45	10.7	7.86	4.01	7.50	17.0	12	12	0.25	2.000	warp) 3.01 oz/
											precoated with
											F839 polyuretha
											porosity control
											coating with D-
											ible thermal co
017-											
-001	5.44	8.90	7.86	3.70	7.55	17.0	12	12	0.25	2.300	MIL-C-5040 Ty
-002	5.13	9.60	7.86	3.82	7.50	17.0	12	12	0.25	2.300	with fibers rem
-003	5.44	8.27	7.86	3.54	7.55	17.0	12	12	0.25	2.300	precoated on fo
											with D1569-F83
											polyurethane,
											controlled by c
											with D-65 flexi
											thermal coating

A

DECELERATOR FABRICATION DATA

DR (in.)	Roof mesh	Suspension lines	Roof cap, skirt panels	Skirt reinforcement web, apex reinforcement web, roof/skirt seam, radials
.625 .688 .625 .625 .625	HT-83-44 Nomex cloth (172-lb tensile, warp) 3.01 oz/sq yd precoated with D1569-F839 polyurethane, porosity controlled by coating with D-65 flexible thermal coating	MIL-C-5040 Type I cord, 100-lb tensile strength	0.84 oz/sq yd 4787 nylon coated with D1569-F839 polyurethane	Double fold, cotton bias tape, 88 × 80 count, 20 lb/in.
.625 .750 .750	MIL-T-713A, Class II, Type 8 nylon lacing (50-lb tensile) precoated on form with D1569-F839 polyurethane, porosity controlled by coating with D-65 flexible thermal coating	MIL-C-5040 Type I cord, 100-lb tensile strength	0.84 oz/sq yd 4787 nylon coated with D1569-F839 polyurethane	Double fold, cotton bias tape, 88 × 80 count, 20 lb/in.
.000 .937 .000	HT-83-44 Nomex mesh cloth (172-lb tensile, warp) 3.01 oz/sq yd, precoated with D1569-F839 polyurethane, porosity controlled by coating with D-65 flexible thermal coating	MIL-C-5040 Type III cord with fibers removed	0.84 oz/sq yd 4787 nylon coated with D1569-F839 polyurethane	Double fold, cotton bias tape, 88 × 80 count, 20 lb/in.
.300 .300 .300	MIL-C-5040 Type I with fibers removed precoated on form with D1569-F839 polyurethane, porosity controlled by coating with D-65 flexible thermal coating	MIL-C-5040 Type III cord with fibers removed	0.84 oz/sq yd 4787 nylon coated with D1569-F839 polyurethane	Double fold, cotton bias tape, 88 × 80 count, 20 lb/in.

(Reverse is blank)

Y/D Cases

$$V = a_0 + a_1\left(\frac{X}{D}\right) + a_2\left(\frac{X}{D}\right)^2 + a_3\left(\frac{X}{D}\right)^3 + a_4\left(\frac{Y}{D}\right)^2 + a_5\left(\frac{Y}{D}\right)^2\left(\frac{X}{D}\right) +$$

$$a_6\left(\frac{Y}{D}\right)^2\left(\frac{X}{D}\right)^2 + a_7\left(\frac{Y}{D}\right)^2\left(\frac{X}{D}\right)^3 + a_8\left(\frac{Y}{D}\right)^4 + a_9\left(\frac{Y}{D}\right)^4\left(\frac{X}{D}\right) +$$

$$a_{10}\left(\frac{Y}{D}\right)^4\left(\frac{X}{D}\right)^2 + a_{11}\left(\frac{Y}{D}\right)^4\left(\frac{X}{D}\right)^3 + a_{12}\left(\frac{Y}{D}\right)^6 + a_{13}\left(\frac{Y}{D}\right)^6\left(\frac{X}{D}\right) +$$

$$a_{14}\left(\frac{Y}{D}\right)^6\left(\frac{X}{D}\right)^2 + a_{15}\left(\frac{Y}{D}\right)^6\left(\frac{X}{D}\right)^3 + a_{16}\left(\frac{Y}{D}\right)^8 +$$

$$a_{17}\left(\frac{Y}{D}\right)^8\left(\frac{X}{D}\right) + a_{18}\left(\frac{Y}{D}\right)^8\left(\frac{X}{D}\right)^2 + a_{19}\left(\frac{Y}{D}\right)^8\left(\frac{X}{D}\right)^3$$

Z/D Cases

$$V = b_0 + b_1\left(\frac{X}{D}\right) + b_2\left(\frac{X}{D}\right)^2 + b_3\left(\frac{X}{D}\right)^3 + b_4\left(\frac{Z}{D}\right)^2 + b_5\left(\frac{Z}{D}\right)^2\left(\frac{X}{D}\right) +$$

$$b_6\left(\frac{Z}{D}\right)^2\left(\frac{X}{D}\right)^2 + b_7\left(\frac{Z}{D}\right)^2\left(\frac{X}{D}\right)^3 + b_8\left(\frac{Z}{D}\right)^4 + b_9\left(\frac{Z}{D}\right)^4\left(\frac{X}{D}\right) +$$

$$b_{10}\left(\frac{Z}{D}\right)^4\left(\frac{X}{D}\right)^2 + b_{11}\left(\frac{Z}{D}\right)^4\left(\frac{X}{D}\right)^3 + b_{12}\left(\frac{Z}{D}\right)^6 + b_{13}\left(\frac{Z}{D}\right)^6\left(\frac{X}{D}\right) +$$

$$b_{14}\left(\frac{Z}{D}\right)^6\left(\frac{X}{D}\right)^2 + b_{15}\left(\frac{Z}{D}\right)^6\left(\frac{X}{D}\right)^3 + b_{16}\left(\frac{Z}{D}\right)^8 + b_{17}\left(\frac{Z}{D}\right)^8\left(\frac{X}{D}\right) +$$

$$b_{18}\left(\frac{Z}{D}\right)^8\left(\frac{X}{D}\right)^2 + b_{19}\left(\frac{Z}{D}\right)^8\left(\frac{X}{D}\right)^3 .$$

The curve fits used only even powers of Y/D or Z/D because of symmetry that exists in the wake of the forebody.

The curve fits are made to the experimentally derived velocities and are the best statistical fits to all the data presented. Thus, the curve is matched to the data points with scatter as well as to the more accurate data points. The multiple regression solution then gives the least squares value of the coefficients for a particular sample of observations.

Samples of the curve fits are shown in Figures 46 through 50. The sinusoidal type variation of the polynomials above Y/D values of 0.4 are smoothed out by the integration since the area under the curve is approximately the same as would exist without the sinusoidal type variation of velocity predicted by the polynomial. The sinusoidal trace is caused by the polynomial curve fit as the polynomial tries to pass through the
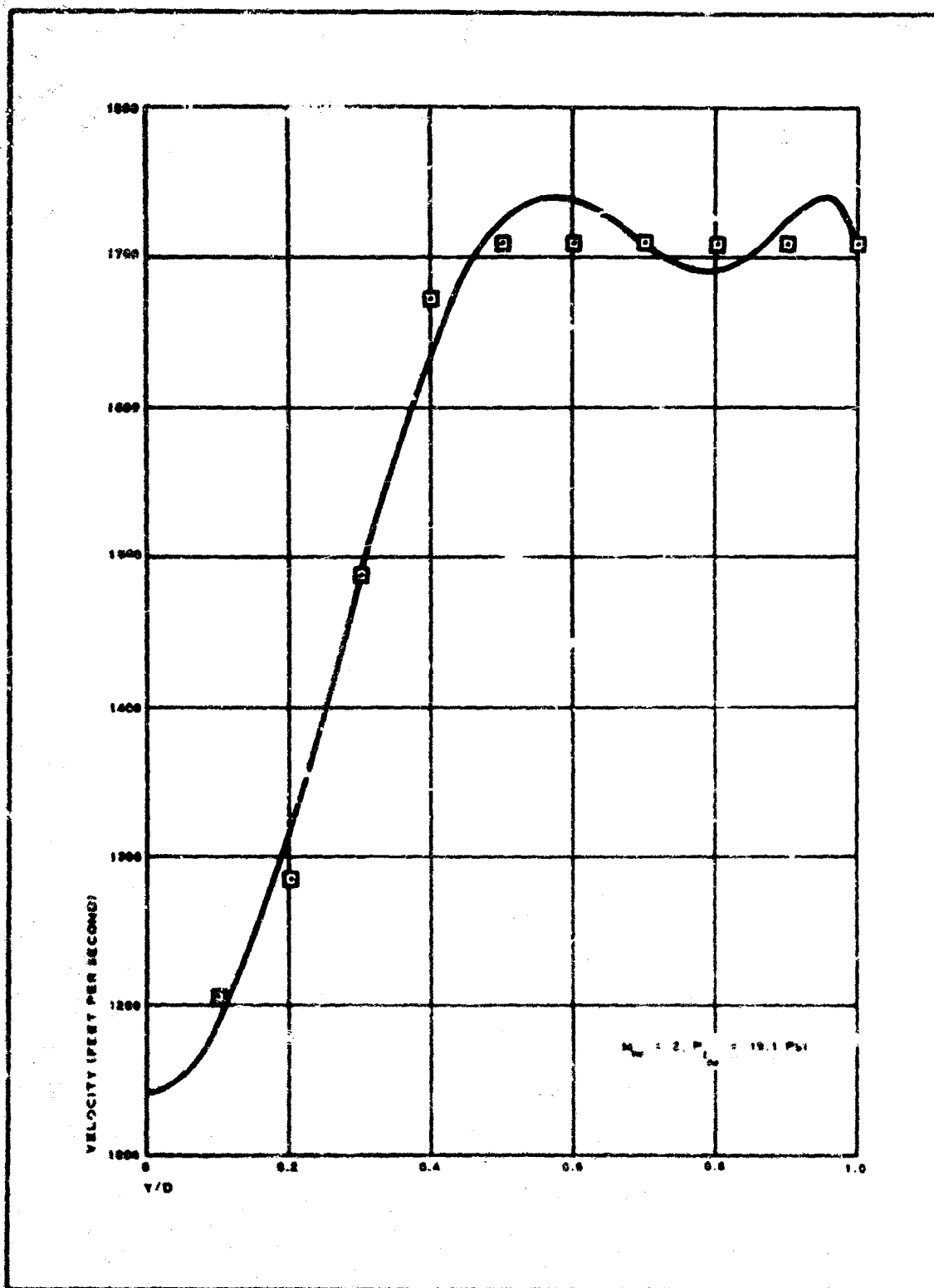
Figure 46 - Experimental Wake Velocity Data Curve Fit, X/D = 3
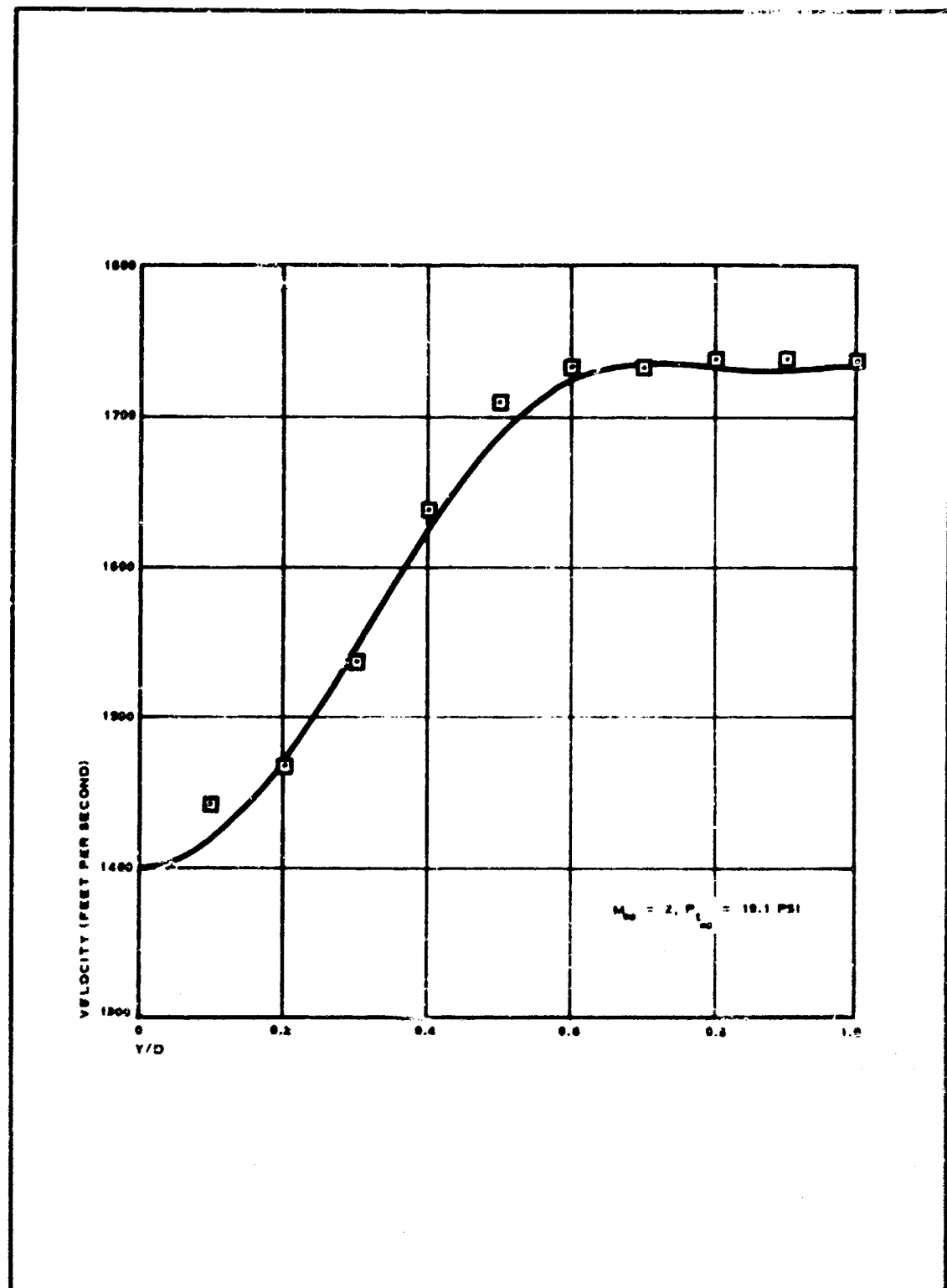
Figure 47 - Experimental Wake Velocity Data Curve Fit, X/D = 5
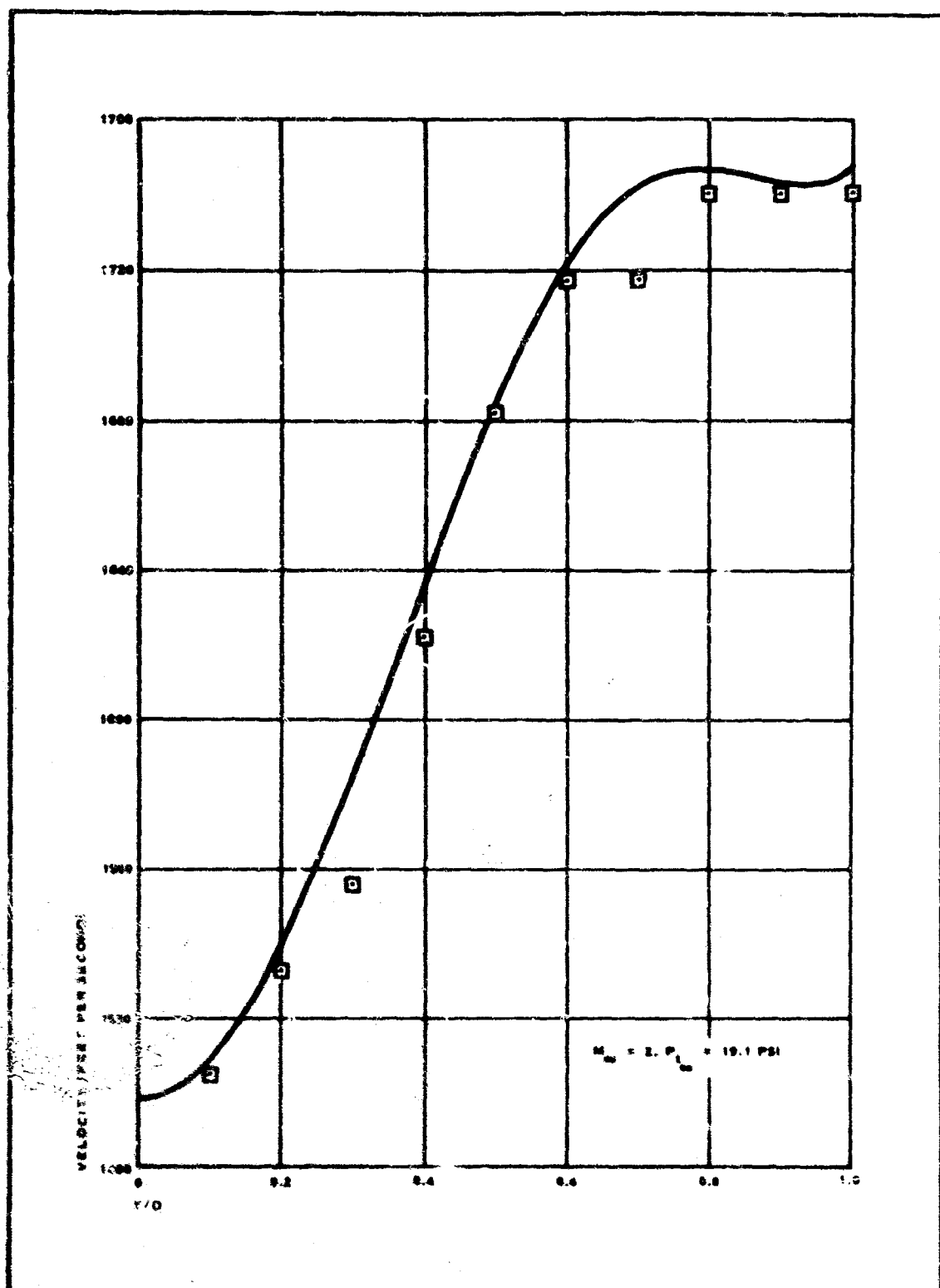
Figure 48 - Experimental Wake Velocity Data Curve Fit, X/D = 7
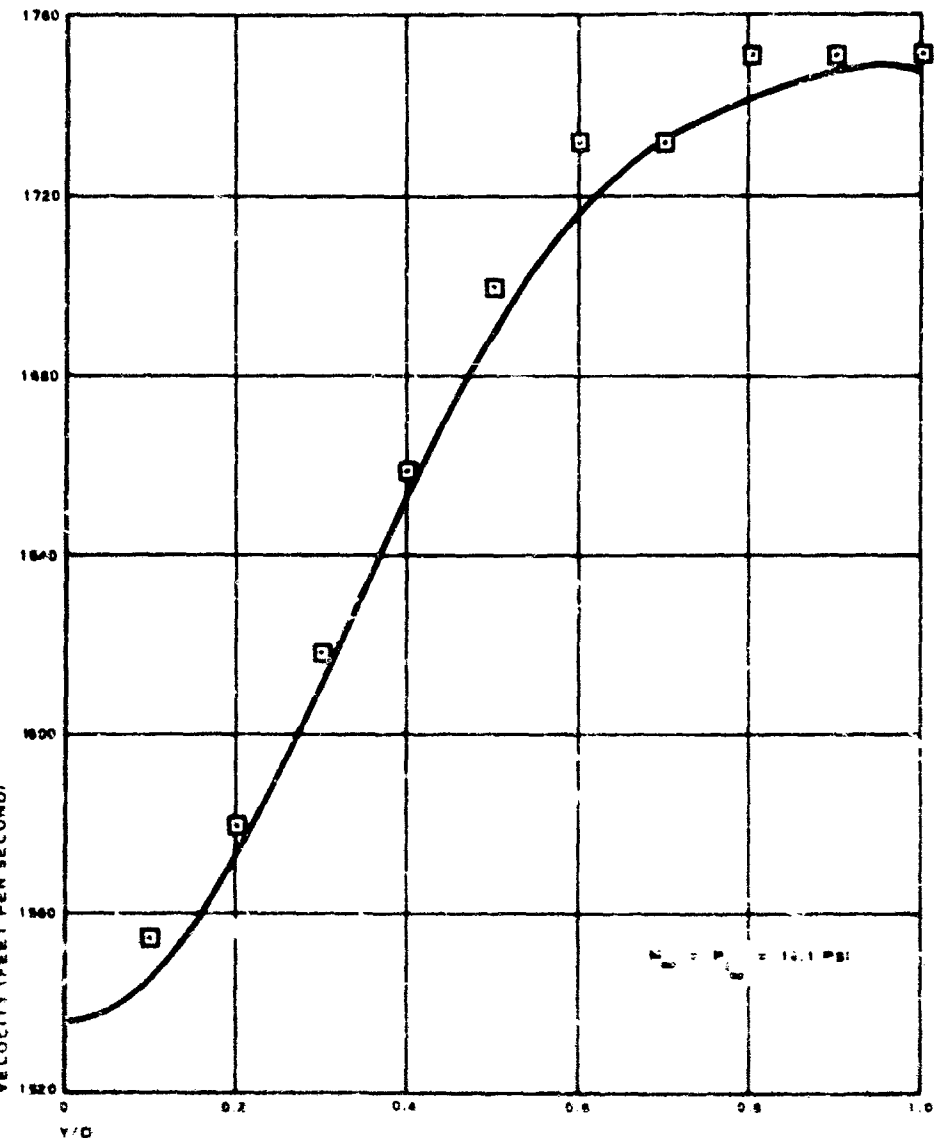
Figure 49 - Experimental Wake Velocity Data Curve Fit, X/D = 9
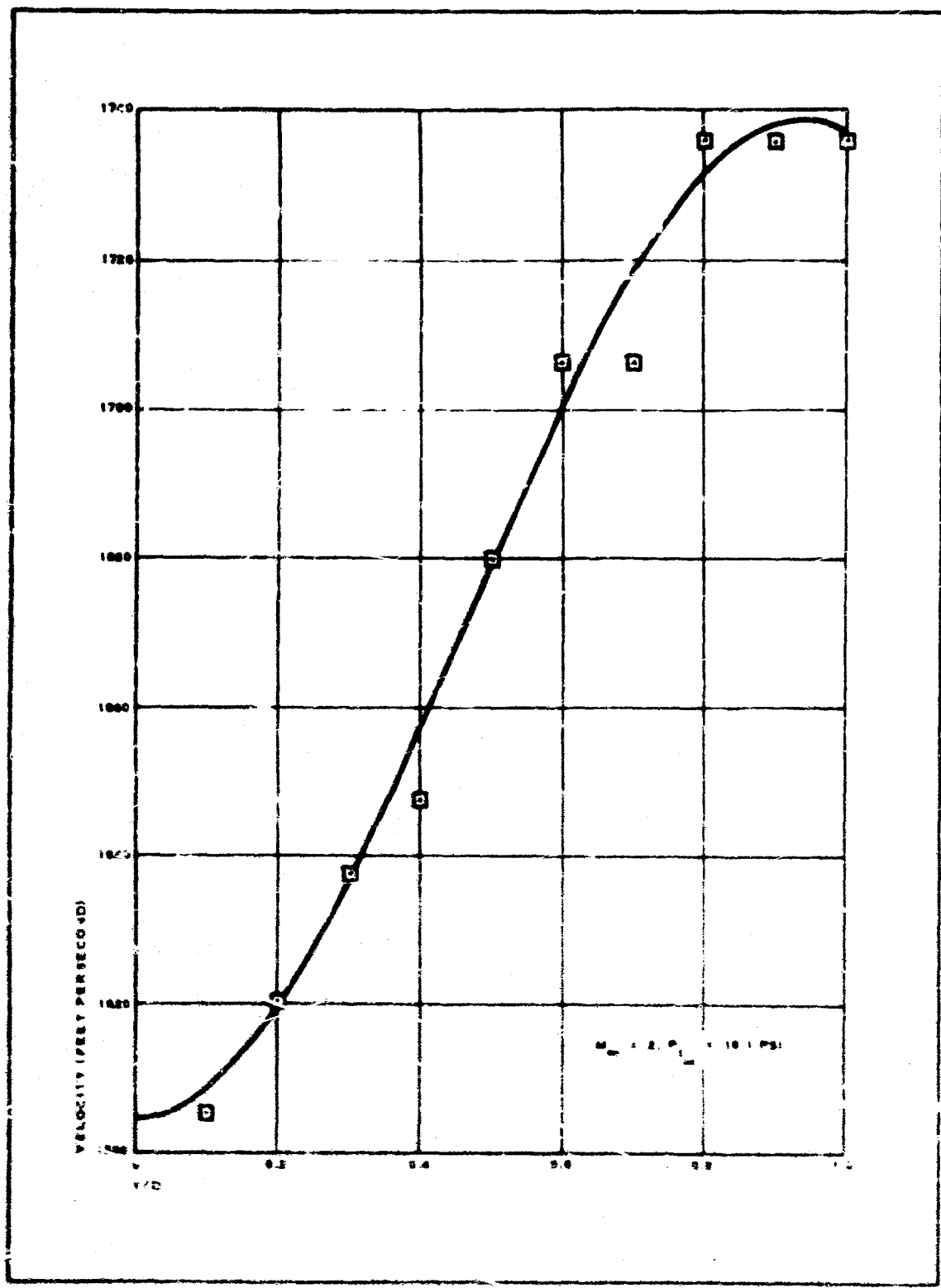
Figure 50 - Experimental Wake Velocity Data Curve Fit, X/D = 11

existing data points. Where the velocity is constant or approximately constant with the change in Y/D or Z/D, the polynomial is unsuccessful in matching the experimental data. The one polynomial for each case is the best fit to all the data points at each X/D station; therefore, the polynomial is attempting to fit or match a surface of points in two dimensions.

c. **Test Data**

Tables XII and XIII give the parachute performance test data (Table XII has data for the WT-IIB series and Table XIII, for the WT-VI series). Both drag and stability parameters were determined.

TABLE XII - PARACHUTE PERFORMANCE TEST DATA, WT-IIB SERIES

TABLE XII – PARACHUTE PERFORMANCE TEST DATA, WT-IIB SERIES (Continued)

Forebody	P/C No.	X/D	Ac/Ab	M∞	q∞ (psi)	R∞/in. ×10^-6	C_D Avg	C_D Max	C_D Min	f_q (cps)	P_b/P_∞ Y/D	P_b/P_∞ Z/D	D_p Max	D_p Min	D_p Avg	f_b (cps)	DP_a/D_c	D_i Max	D_i Min	D_i Avg	a (deg) +	a (deg) −	f_a (cps)
Basic Arapaho "C"	015-002	5.0	3.425	4.00	0.5	0.047	0.235	0.242	0.221	122	2.32	0.28	5.30	5.30	5.30	0.0	0.884	4.80	4.80	4.80	0.0	0.0	0.0
		6.0					0.318	0.339	0.263	111	0.32	0.27				33.3	0.870	4.80	4.30	4.55	4.0	4.5	14.15
		7.0					0.263	0.346	0.242	110	0.31	0.35	5.40	5.03	5.22	32.6	0.665	4.90	4.07	4.49	4.5	4.5	7.14
		8.0			1.0	0.092	0.298	0.367	0.229	144	0.30	0.23	5.43	4.93	5.18	32.6	0.886	4.90	4.87	4.89	0.0	0.0	0.0
		4.5					0.141	0.152	0.131	155	0.59	0.64	5.33	5.33	5.33	0.0	0.868	4.70	4.70	4.70	2.5	2.3	0.0
		5.0					0.159	0.170	0.148	131	0.51	0.51	5.20	5.20	5.20	0.0					4.0	2.0	11.15
		6.0					0.230	0.248	0.202	102	0.38	0.35	5.50	4.57	5.24	47.0	0.831	4.80	4.30	4.55	4.0	4.0	9.90
		7.0					0.201	0.229	0.180	106	0.33	0.29	5.50	4.97	5.24	32.6	0.872	4.97	4.53	4.7	0.0	0.0	9.01
		8.0					0.207	0.242	0.178	155	0.31	0.28	5.27	5.30	5.29	0.0	0.881	4.70	4.70	4.70	0.0	0.0	0.0
		4.5			1.5	0.135	0.208	0.217	0.182	147	0.34	0.35	5.10	5.10	5.10	0.0	0.850	4.50	4.50	4.50	2.0	2.5	0.0
		5.0					0.18?	0.19?	0.173		0.30	0.30									4.0	4.0	0.0
		6.0					0.180	0.19?	0.181		0.22	0.24									2.0		0.9
		7.0					0.185	0.177	0.178		0.24	0.23	5.43	5.07	5.25	42.8	0.875	4.97	4.63	4.80	0.0	0.0	19.25
		8.0					0.199	0.229	0.178	91	0.23	0.23	5.27	5.07	5.17	44.1	0.061	4.97	4.57	4.77	0.0	0.0	10.75
		4.5			0.5	0.068	0.16?	0.26?	0.157		0.63	0.59	5.00	5.00	5.00	0.0	0.833	4.75	4.70	4.73	0.0	0.0	0.9
		5.0					0.190		0.169	88	0.46	0.39	5.20	5.05	5.13	0.0	0.855	4.70	4.70	4.70	2.0	0.0	0.0
		6.0					0.183	0.203	0.176	72	0.43	0.33									1.5	1.5	0.0
		7.0					0.175	0.202	0.169		0.38	0.28	5.50	4.77	5.14	18.05	0.856	4.92	4.13	4.53	0.0	0.0	5.0
		8.0					0.239	0.457	0.218	125	0.35	0.26	5.47	4.73	5.10	34.80	0.650	4.80	4.13	4.47	0.0	0.0	5.0
		4.5			1.0	0.124	0.199	0.255	0.164		0.33	0.30	5.50	5.30	5.40	0.0	0.900	4.93	4.70	4.83	0.0	0.0	0.0
		5.0					0.140	0.175	0.199	103	0.32	0.29	5.47	5.07	5.27	41.6	0.878	5.03	4.47	4.75	2.0	2.0	0.0
		6.0					0.193	0.225	0.130	106	0.30	0.29									2.0	0.0	0.0
		7.0					0.159	0.193	0.141	127	0.28	0.22	5.50	4.77	5.05	31.9	0.842	4.90	4.15	4.53	0.0	0.0	5.0
		8.0					0.154	0.161	0.147	167	0.26	0.20	5.10	4.70	4.90	20.8	0.817	4.60	4.03	4.30	0.0	0.0	5.0
		4.5			1.5	0.171	0.203	0.236	0.170	122	0.25	0.23	5.27	4.80	5.04	51.8	0.840	4.60	4.15	4.38	0.0	0.0	5.0
		5.0					0.176	0.214	0.159	115	0.24	0.23	5.27	4.73	5.00	48.4	0.833	4.83	4.07	4.45	0.0	0.0	5.0
		6.0					0.170	0.197	0.153	134	0.23	0.22	5.37	4.77	5.07	41.6	0.845	4.73	4.03	4.38	0.0	0.0	5.0
		7.0					0.155	0.165	0.143	189	0.23	0.22	5.10	4.67	4.89	26.8	0.814	4.67	4.13	4.40	0.0	0.0	5.0
		8.0					0.153	0.160	0.148	144	0.47	0.45									0.0	0.0	5.0
	016-001	6.0	5.9	3.00	0.5	0.037	0.173	0.179	0.177	148	0.42	0.41	7.50	7.07	7.29	37.4	0.927	6.80	6.20	6.50	0.0	0.0	7.4
		7.0					0.340	0.370	0.222	48	0.39	0.38	7.80	7.00	7.40	46.9	0.490	7.20	6.00	5.60	5.0	5.0	
		8.0					0.431	0.586	0.309		0.37	0.37	7.85	6.10	6.98	0.0	0.890	7.03	3.35	6.20			
		9.0			1.0	0.067	0.449	0.694	0.243		0.37	0.36											
		6.0					0.531	0.879	0.388		0.32	0.36				0.0					0.0	0.0	0.0
		7.0					0.339	0.35?	0.320	144	0.32	0.35	7.67	6.83	7.25	37.4	0.923	6.97	6.27	6.62	0.0	0.0	0.0
		8.0					0.292	0.387	0.240	121	0.32	0.34	7.67	6.72	7.20	40.5	0.916	7.20	6.37	6.79	0.0	0.0	0.0
		9.0					0.333	0.458	0.197	99	0.52	0.32	7.70	6.22	6.95	41.6	0.884	7.17	6.60	6.30	15.0	15.0	15.25
		10.0			1.5	0.102	0.431	0.684	0.236	100	0.51	0.37				0.0					0.0	0.0	
		6.0					0.450	0.860	0.360	85	0.31	0.36									0.0	0.0	0.0
		7.0					0.339	0.427	0.314	153	0.33	0.39									0.0	0.0	0.0
		8.0					0.234	0.436	0.217	112	0.31	0.31	7.07	5.67	7.27	46.9	0.925	7.33	5.87	6.40	15.0	15.0	
	016-002	6.0		4.00	0.5	0.048	0.189	0.306	0.090	87	0.29	0.44					0.874	6.23	5.70	5.97	0.0	0.0	9.0
		7.0					0.178	0.212	0.161	86	0.46	0.35	7.37	6.67	6.87	28.23	0.928	6.47	5.63	6.05	0.0	0.0	0.0
		8.0					0.172	0.180	0.160	72	0.34	0.25	7.13	5.47	7.30	0.0	0.872	6.27	5.97	6.12	0.0	0.0	0.0
		9.0			1.5	0.140	0.201	0.203	0.193	94	0.32	0.22	6.93	6.77	6.45	0.0					0.0	0.0	0.0
							0.120	0.121	0.119	68	0.23	0.24	5.43		6.32	34.1	0.904	6.40	6.43	5.42	0.0	0.0	0.0
							0.186	0.247	0.140		0.24	0.26	7.20										

Blunted
elliptical
cone

016-002

017-001

014-003

TABLE XII - PARACHUTE PERFORMANCE TEST DATA, WT-IIB SERIES (Continued)

Forebody	D/C No.	X/D	A_c/A_b	M_∞	q_∞ (psi)	$Re_\infty/in. \times 10^{-6}$	C_D Avg	C_D Max	C_D Min	f_f (cps)	P_f/P_∞ Y/D	P_f/P_∞ Z/D	D_p (in.) Max	D_p (in.) Min	D_p (in.) Avg	f_b (cps)	DP_s/D_c	D_l (in.) Max	D_l (in.) Min	D_l (in.) Avg	ζ (deg) +	ζ (deg) -	f_s (cps)
Blunted elliptical cone	014-003	7.0	1.91	3.00	1.5	0.103	0.202	0.293	0.158	170	. . .	0.23	6.00	5.20	5.60	0.0	0.934	5.07	6.53	4.60	2.5	3.5	7.62
		8.0					0.209	0.312	0.158	190	. . .	0.23	. . .	. . .	. . .	. . .	. . .	. . .	. . .	. . .	. . .	. . .	. . .
		9.0		4.00	0.3	0.045	0.165	0.366	0.103	. . .	. . .	0.39	5.77	4.17	4.97	31.2	0.828	5.10	3.17	4.14	4.0	4.5	0.0
		6.0					0.234	0.303	0.189	228	. . .	0.43	. . .	. . .	. . .	. . .	. . .	. . .	. . .	. . .	2.0	3.0	7.55
		7.0					0.179	0.290	0.138	292	. . .	0.37	5.83	5.50	5.67	0.0	0.945	5.07	4.57	4.87	1.0	3.0	6.14
		7.5					0.172	0.248	0.138	163	. . .	0.33	5.67	5.23	5.45	45.5	0.909	5.00	4.63	4.82	2.0	3.0	6.74
		4.0			0.090		0.138	0.186	0.096	125	. . .	0.30	. . .	. . .	. . .	. . .	. . .	. . .	. . .	. . .	0.0	0.0	0.0
		4.0					0.290	0.293	0.205	248	. . .	0.20	5.75	5.50	5.63	0.0	0.936	4.95	4.70	4.83	0.0	0.0	0.0
		5.0					0.218	0.316	0.165	161	. . .	0.20	5.60	5.40	5.50	0.0	0.917	4.33	4.33	4.52	0.0	0.0	0.0
		6.0					0.144	0.165	0.130	272	. . .	0.20	5.50	5.37	5.44	0.0	0.905	4.90	4.87	4.89	0.0	0.0	0.0
		7.0			0.136		0.116	0.141	0.105	299	. . .	0.19	. . .	. . .	. . .	. . .	. . .	. . .	. . .	. . .	0.0	0.0	0.0
		8.0					0.141	0.139	0.130	248	. . .	0.20	. . .	. . .	. . .	. . .	. . .	. . .	. . .	. . .	0.0	0.0	9.8
		4.0					0.297	0.409	0.214	107	. . .	0.20	6.13	4.73	5.43	31.3	0.909	5.53	3.90	4.72	6.5	6.5	0.0
		5.0					0.229	0.260	0.196	280	. . .	0.19	5.50	5.30	5.48	0.0	0.934	4.80	4.35	4.58	3.0	4.0	3.97
		6.0			0.060		0.160	0.162	0.147	232	. . .	0.19	5.60	5.05	5.33	0.0	0.914	4.80	4.40	4.60	0.0	0.0	0.0
		7.0					0.142	0.158	0.127	168	. . .	0.19	. . .	. . .	. . .	. . .	0.888	. . .	. . .	. . .	0.0	0.0	0.0
		8.0					0.111	0.132	0.790	233	. . .	0.18	. . .	. . .	. . .	. . .	. . .	. . .	. . .	. . .	0.0	0.0	0.0
		4.0		5.00			0.122	0.149	0.081	128	. . .	0.29	3.90	4.20	5.05	39.3	0.842	5.10	2.63	3.97	5.0	6.5	9.8
		4.0					0.182	0.253	0.142	181	. . .	0.32	5.50	5.10	5.10	0.0	0.834	4.73	4.23	4.48	0.0	0.0	0.0
		6.0			0.173		0.094	0.101	0.081	120	. . .	0.28	5.37	5.03	5.20	0.0	0.867	4.50	4.31	4.47	0.0	0.0	0.0
		7.0					0.101	0.128	0.094	196	. . .	0.24	. . .	. . .	. . .	. . .	. . .	. . .	. . .	. . .	0.0	0.0	0.0
		8.0					0.094	0.094	0.094	138	. . .	0.25	5.87	3.98	4.93	39.3	0.822	5.00	3.37	4.19	10.0	7.0	11.6
		4.0					0.066	0.103	0.030	102	. . .	0.53	5.87	4.20	4.93	. . .	. . .	. . .	. . .	. . .	0.0	0.0	0.0
		4.0					0.170	0.179	0.153	222	. . .	0.37	5.30	5.10	5.20	0.0	0.867	4.40	3.97	4.19	0.0	0.0	0.0
		5.0			0.102		0.125	0.130	0.118	208	. . .	0.24	5.30	4.95	5.13	0.0	0.855	4.75	4.25	4.50	0.0	0.0	0.0
		7.8					0.120	0.125	0.111	188	. . .	0.20	. . .	. . .	. . .	. . .	. . .	. . .	. . .	. . .	0.0	3.0	8.05
		8.0					0.122	0.129	0.113	208	0.54	0.17	5.57	5.25	5.41	0.0	0.902	4.73	4.00	4.37	45.0	45.0	. . .
	018-002	4.0		3.00	0.5	0.037	0.362	0.458	0.350	169	0.54	0.53	5.50	4.93	5.22	25.2	0.870	5.07	3.63	4.45	0.0	6.0	7.7
		5.0					0.581	0.702	0.466	181	0.55	0.53	5.60	5.43	5.53	0.0	0.922	4.83	4.55	4.69	4.0	6.0	6.57
		6.0					0.433	0.561	0.331	94	0.49	0.45	5.60	5.50	5.52	0.0	0.920	5.00	4.95	4.98	5.0	5.0	6.12
		7.0					0.343	0.412	0.248	79	0.46	0.42	5.53	5.50	5.52	0.0	. . .	. . .	. . .	. . .	3.0	5.0	5.28
		8.0					0.325	0.369	0.267	124	0.43	0.38	5.70	5.60	5.65	0.0	0.942	4.85	4.85	4.93	5.0	5.0	0.0
		4.0			0.102		0.579	0.666	0.507	246	0.62	0.52	5.75	5.60	5.68	0.0	0.946	4.95	4.50	4.73	0.0	2.0	0.0
		4.0					0.47	0.614	0.402	124	0.36	0.26	5.50	5.24	5.28	0.0	0.887	4.90	4.75	4.83	3.0	3.0	8.05
		6.0					0.374	0.432	0.327	174	0.31	0.21	5.63	5.20	5.42	0.0	0.905	4.80	4.37	4.59	4.0	3.5	9.17
		7.0			0.048		0.413	0.561	0.355	153	0.28	0.20	5.43	5.13	5.28	0.0	0.880	4.73	4.47	4.60	2.0	2.0	4.24
		8.8					0.93	1.123	0.517	135	0.27	0.19	. . .	. . .	. . .	. . .	. . .	. . .	. . .	. . .	. . .	. . .	. . .
		4.0		4.00	0.5	0.094	0.110	0.151	0.082	178	. . .	0.47	5.50	5.07	5.29	0.0	0.880	4.70	4.27	4.45	7.0	7.0	6.05
		5.0					0.748	0.068	0.034	225	. . .	0.43	5.50	5.13	5.18	0.0	0.864	4.67	4.60	4.64	0.0	0.0	5.06
		6.0					0.161	0.137	0.027	190	. . .	0.39	5.50	5.07	. . .	. . .	. . .	. . .	. . .	. . .	10.0	10.0	5.55
		7.0					0.154	0.096	0.048	231	. . .	0.35	5.23	5.13	. . .	. . .	. . .	. . .	. . .	. . .	10.0	10.0	0.0
		4.0					0.151	0.297	0.062	209	. . .	0.42	5.65	5.45	5.55	0.0	0.925	4.85	4.80	4.82	0.0	0.0	0.0
		4.0					0.236	0.274	0.200	205	. . .	0.52	5.63	5.20	5.42	0.0	0.905	4.80	4.37	4.59	6.0	6.0	12.25
		5.0					0.160	0.236	0.133	221	. . .	0.38	5.43	5.13	5.28	0.0	0.880	4.73	4.47	4.60	4.0	3.5	9.17
		6.0					0.54	0.207	0.129	230	. . .	0.33	. . .	. . .	. . .	. . .	. . .	. . .	. . .	. . .	2.0	2.0	4.24
		7.8					0.16	0.140	0.102	229	. . .	0.29	. . .	. . .	. . .	. . .	. . .	. . .	. . .	. . .	0.0	0.0	0.0
		8.0			0.142		0.102	0.123	0.088	221	. . .	0.24	. . .	. . .	. . .	. . .	. . .	. . .	. . .	. . .	0.0	0.0	0.0
		4.0					0.187	0.231	0.130	125	. . .	0.30	5.43	5.30	5.37	0.0	0.895	4.90	4.90	4.90	0.0	5.0	9.70
							0.160	0.209	0.131	209	. . .	0.24	. . .	. . .	. . .	. . .	. . .	. . .	. . .	. . .	. . .	. . .	. . .

TABLE XII – PARACHUTE PERFORMANCE TEST DATA, WT-IIB SERIES (Continued)

Test body	T/C No.	M.C.	A_c/A_b	M_∞	q_∞ (psi)	$Re_\infty/in \times 10^{-6}$	C_D Avg	C_D Max	C_D Min	f (cps)	P_b/P_∞ Y/D	P_b/P_∞ Z/D	C_p (in.) Max	C_p (in.) Min	C_p (in.) Avg	f_b (cps)	DP_a/D_c	D_1 (in.) Max	D_1 (in.) Min	D_1 (in.) Avg	θ (deg)		f_e (cps)
Blunted elliptical cone	617-001	6.0	3.425	3.00	2.5	0.069	0.145	0.295	0.086	158	0.62	0.50	7.37	6.30	6.86	20.4	0.875	6.23	5.03	5.63	0.0	0.0	0.0
		7.0					0.141	0.263	0.282	115	0.55	0.40	7.13	5.40	6.25	37.0	0.798	6.47	4.50	5.4	0.0	0.0	0.0
		6.0			0.75	0.098	0.129	0.204	0.074	107	0.91	0.35	7.25	3.53	5.39	22.9	0.686	6.65	2.73	4.69	0.0	0.0	0.0
		5.0					0.166	0.232	0.061	158	0.47	0.34									0.0	0.0	0.0
		7.0			1.0	0.123	0.207	0.342	0.126	196	0.51	0.41	7.60	5.17	6.28	22.2	0.800	6.37	4.13	5.25	0.0	0.0	0.0
		6.0					0.248	0.381	0.153	154	0.41	0.33	7.31	5.50	6.42	23.5	0.817	6.67	4.41	5.55	0.0	0.0	0.0
		5.0					0.208	0.349	0.133	125	0.39	0.27									0.0	0.0	0.0
		7.0			0.5	0.032	0.248	0.373	0.141	126	0.39	0.24	7.33	3.43	5.38	27.8	0.684	6.57	2.90	4.79	0.0	0.0	0.0
		6.0					0.152	0.284	0.075	140	0.45	0.33									0.0	0.0	0.0
		5.0					0.231	0.372	0.139	128	0.49	0.38	7.30	5.60	6.65	33.4	0.820	6.23	4.28	5.25	4.0	4.0	9.8
		6.0			1.0	0.035	0.303	0.410	0.180	165	0.44	0.32	7.17	4.37	5.77	20.2	0.735	6.27	3.23	4.75	3.0	3.0	16.5
							0.302	0.408	0.210	106	0.44	0.26	7.60	6.43	7.02		0.893	6.90	5.41	6.17	9.0	9.0	
							0.244	0.347	0.102	120	0.37	0.22											
					0.5		0.669	0.749	0.610	254	0.65	0.64	7.90	7.80	7.85	0.0	0.999	7.05	6.75	6.79	0.0	0.0	0.0
							0.743	0.815	0.647	235	0.65	0.64	7.60	7.70	7.79	0.0	0.985	7.00	6.90	6.95	0.0	0.0	0.0
					1.0	0.64	0.675	0.742	0.623	233	0.65	0.62	7.77	7.17	7.47	0.0	0.950	7.00	6.33	6.67	4.0	4.0	13.15
							0.647	0.701	0.578	216	0.65	0.62	7.60	6.43	7.02		0.893	6.90	5.41	6.17	5.0	5.0	12.90
							0.705	0.879	0.548	207	0.64	0.62			7.56		0.962	6.83	6.75	6.79	16.5	17.5	8.74
							0.348	1.048	0.760	180	0.62	0.61	7.67	7.45	7.46		0.952	6.80	6.70	6.75	2.0	2.0	0.0
							0.744	0.815	0.676		0.54	0.49	7.67	7.07	7.37		0.938	6.91	6.23	6.58	5.0	5.0	0.0
					0.5	0.048	0.733	0.880	0.461	228	0.53	0.59											
							0.791	0.911	0.680	234	0.51	0.59				16.75	0.800	6.43	3.90	5.17	0.0	0.0	0.0
							0.792	0.931	0.694	233	0.51	0.58	7.27	5.30	6.29	44.3					2.0	2.0	0.0
							0.172	0.220	0.128	156	0.81	0.80			5.95								
	617-002						0.519	0.607	0.475	190	0.72	0.65	7.47	7.20	7.23	0.0	0.885	6.60	5.30	6.05	0.0	0.0	15.45
							0.512	0.563	0.473	173	0.41	0.53	7.55	6.80	7.18	42.8	0.864	6.77	5.20	5.99	5.0	5.0	0.0
					0.64		0.494	0.549	0.425	191	0.53	0.45											
							0.636	0.682	0.448	171	0.45	0.40	7.20	6.27	6.74	0.0	0.857	6.63	5.20	5.92	11.0	10.0	8.42
							0.968	0.774	0.433	177	0.43	0.41											
							0.485	0.560	0.438	174	0.43	0.38	7.57	7.50	7.54	0.0	0.958	6.55	6.55	6.54	9.0	9.0	15.45
					1.0	0.048	0.558	0.626	0.492	196	0.39	0.31	7.33	7.07	7.20	0.0	0.916	6.70	6.27	6.49	6.0	6.0	12.78
							0.547	0.628	0.492	188	0.36	0.28											
							0.598	0.805	0.615	146	0.34	0.26									5.0	5.0	9.14
	617-002						0.103	0.196	0.059	177		0.77	7.47	5.30	5.90	0.0	0.737	5.23	3.90	4.62	2.0	2.0	0.0
							0.167	0.187	0.139	206		0.74											
					1.5	0.140	0.264	0.292	0.240	115		0.57									0.0	0.0	0.0
							0.208	0.272	0.120	164		0.44									5.0	5.0	4.79
							0.092	0.249	0.044	116		0.40	6.20	5.60	5.90	0.0	0.730				3.0	3.0	5.38
							0.255	0.194	0.098	148	0.62	0.56											
							0.355	0.245	0.245	159	0.68	0.59		4.53				4.60	2.90	4.95	15.0	15.0	15.4
	617-003				0.5	0.063	0.306	0.462	0.176	161	0.63	0.38	7.47	6.47	6.97	0.0	0.885	4.60	5.30	6.05	11.0	11.0	0.0
							0.227	0.390	0.141	187	0.57	0.29			6.78								
							0.225	0.364	0.129	139	0.90	0.26	6.90	6.53	6.72	0.0	0.855	6.57	5.33	5.45	3.0	3.0	8.94
							0.200	0.240	0.168	142	0.91	0.37	7.40	6.67	7.04	0.0	0.895	6.57	5.73	6.15	2.0	2.0	8.73
							0.208	0.288	0.152	127	0.63	0.63									6.0	6.0	0.0
	617-003				1.0		0.238	0.314	0.210	165		0.57							3.33	5.45	3.0	3.0	9.14
							0.258	0.326	0.219	138		0.48							5.73	6.15	2.0	2.0	9.13
	617-001				1.5	0.176	0.263	0.307	0.231		0.90	0.82	7.63	5.17	6.10	27.8	0.775	6.77	3.83	5.30	6.0	6.0	0.0
							0.242	0.352	0.136	137	0.91	0.82									12.0	12.0	11.55
							0.385	0.512	0.245	143	0.92	0.78									8.0	8.0	

TABLE XII - PARACHUTE PERFORMANCE TEST DATA, WT-IIB SERIES (Continued)

TABLE XII - PARACHUTE PERFORMANCE TEST DATA, WT-IIB SERIES (Continued)

TABLE XIII - PARACHUTE PERFORMANCE TEST DATA. WT-VI SERIES

Remarks	P/C No.	X/D	A_o/A_p	A_b/A_p	L_s/D	$R_e (/in. \times 10^{-5})$	C_D Avg	C_D Max	C_D Min	f_t (cps)	P_o/P_∞ Y/D	P_o/P_∞ Z/D	D_p (in.) Max	D_p (in.) Min	D_p (in.) Avg	f_b (cps)	DP_s/D_c	D_i (in.) Max	D_i (in.) Min	D_i (in.) Avg	α (deg) $+$	α (deg) $-$	f_o (cps)
AFT faired cone Nose cone	014-006	5.0	3.425		1.00	0.127	0.336			102	0.17	0.16	6.23	5.60	5.91	75.0	.985	5.72	4.97	5.37	0.0	0.0	0.0
		5.0					0.375			82	0.16	0.13				0.0		5.30	4.23	4.79	0.0	0.0	0.0
		6.0					0.342			94	0.11	0.12	6.07	5.75	5.91	55.5	0.985	5.37	4.80	5.09	0.0	0.0	0.0
		7.0				0.098	0.361			57	0.12	0.12	6.17	5.67	5.92	0.0	0.987	5.73	5.30	5.73	0.0	0.0	0.0
		5.0		4.00			0.424			136	0.22	0.19	5.27	5.80	6.04	0.0	1.019	5.73	5.03	5.38	5.0	5.0	14.6
		6.0					0.421			94	0.21	0.17				0.0		5.43	4.57	5.00	5.0	2.0	0.0
		5.0		3.00		0.073	0.341			128	0.20	0.30	6.17	5.97	6.02	0.0	1.000	5.52	5.13	5.33	0.0	0.0	0.0
		6.0					0.496			67	0.32	0.30	6.33	6.20	6.27	0.0	1.050	5.73	5.66	5.70	0.0	0.0	12.3
		4.0					0.565			58	0.29	0.25				0.0		5.53	4.43	4.73	10.0	30.0	16.3
		5.0		2.00		0.058	0.453			15	0.29	0.30	6.07	3.87	4.77	55.5	0.830	5.57	3.27	4.42	10.0	10.0	0.0
		5.0					0.47			85	0.32	0.30	6.27	6.17	6.23	0.0	1.040	5.53	4.97	5.39	7.0	7.0	19.0
		6.0					0.848			86	0.87	0.86	6.27	5.82	6.04	0.0	1.910	5.80	5.37	5.44	12.0	12.0	20.4
		7.0					1.044			80	0.54	0.53				0.0		5.59	4.73	5.28	11.0	11.0	15.4
	015-002	5.0	3.425	2.00	1.00	0.058	0.955				0.56	0.56	6.40	5.23	5.81	45.4	0.479	5.82	5.37	4.59	13.0	13.0	0.0
		6.0					0.654			128	0.55	0.54	6.00	6.00	6.00	0.0	1.000	5.40	4.49	3.95	6.0	6.0	0.0
		7.0					0.698				0.53	0.53				0.0		5.50	5.03	5.27	9.0	9.0	12.6
		5.0		3.00		0.00	0.844				0.55	0.30	6.10	5.67	5.89	0.0	0.990	5.76	5.57	5.76	0.0	0.0	0.0
		6.0					0.571				0.35	0.30	6.07	6.00	6.04	0.0	1.101	4.97	4.47	4.97	0.0	0.0	12.3
		7.0					0.446				0.29	0.29	6.00	6.00	6.00	0.0	1.000	5.50	5.13	5.72	0.0	0.0	0.0
		5.0		4.00		0.00	0.441			154	0.33	0.28	6.18	6.00	6.09	0.0	1.000	5.30	5.47	4.77	7.0	3.0	13.9
		6.0					0.376			148	0.20	0.22	6.00	5.78	5.94	0.0	0.845	4.97	5.11	5.24	5.0	6.0	4.0
		7.0					0.334			120	0.26	0.21	6.04	5.47	5.72	0.0	0.965	5.22	4.91	4.91	5.0	5.0	10.9
		5.0		5.00		0.133	0.309			90	0.50	0.45				0.0		5.77	4.69	4.97	0.0	0.0	2.0
		6.0					0.278			148	0.48	0.40	6.00	5.60	5.80	0.0	1.000	5.23	4.65	4.70	0.0	0.0	13.0
		7.0					0.302			125	0.30	0.31				0.0		5.50	4.71	4.97	4.0	4.0	15.3
	016-003	5.0	3.425	5.00	1.00	0.127	0.272			73	0.61	0.63	4.18	3.73	6.41	23.2		5.33	4.77	5.42	0.0	0.0	0.0
		6.0					0.194			85	0.42	0.40	7.17		6.41	35.5		6.02		5.00	0.0	0.0	0.0
		7.0					0.287			87	0.26	0.24	7.35	4.57	5.96	37.6		6.50	4.50		0.0	0.0	0.0
		5.0		4.00		0.093	0.335			74	0.30	0.25									0.0	0.0	0.0
		6.0					0.281			114	0.28	0.23				0.0		6.57		6.69	0.0	0.0	0.0
		7.0					1.026			106	0.25	0.19			7.75	0.0		6.78		6.74	0.0	0.0	16.7
	016-002	5.0	3.425	3.00		0.073	0.025			15	0.52	0.49	7.80	7.70	7.73	0.0	0.918	6.80	6.57	6.74	0.0	0.0	2.0
		6.0					0.772			140	0.49	0.45	7.80	7.57	7.62	0.0	0.917	6.77	6.43	6.02	0.0	0.0	0.0
		7.0					0.827			161	0.48	0.45	7.80	7.57	7.50	0.0	0.292	6.80	6.67	5.79	0.0	0.0	0.0
		5.0		2.00		0.036	0.718			162	0.56	0.57			7.75	0.0		6.90	6.65	6.69	0.0	0.0	0.0
		6.0					1.005			130	0.54	0.56	7.75	7.65	7.08	0.0	0.965	6.75	6.57	6.69	0.0	0.0	0.0
		7.0					1.255				0.53	0.56	7.70	7.55	7.62	0.0	0.947	6.73	6.57	6.45	0.0	0.0	0.0
		5.0		3.00		0.073	0.866			145	0.55	0.56	7.80	7.70	7.75	0.0	0.292	6.87	6.70	4.79	0.0	0.0	0.0
		6.0					0.955			176	0.55	0.56				0.0		6.70	6.57	4.49	0.0	0.0	0.0
Blunted eliptical cone		7.0		4.00		0.673	0.743				0.44	0.44	7.57	2.57	7.49	0.0	0.965	5.77	6.60	6.69	4.0	0.0	4.0
		5.0					0.786			85	0.46	0.42	7.60	2.23	7.42	0.0	0.943	5.83	5.25	4.59	0.0	3.0	0.0
		6.0					0.700			87	0.45	0.42	7.60	7.45	7.93	0.0	0.960	6.20	2.70	6.25	0.0	0.0	0.0
		7.0		5.00		0.050	0.304			47	0.78	0.54	7.60	7.40	7.50	0.0	0.955	6.33	6.40	6.42	0.0	0.0	0.0
		5.0					0.476			107	0.57	0.60	1.60	7.33	7.4	0.0	0.950	6.81	4.50	6.72	0.0	0.0	0.0
		6.0				0.067	0.453			117	0.44	0.49	7.40		7.14	0.0	0.971	6.73	6.43	4.58	0.0	7.0	1.0
		5.0					0.469			125	0.42	0.47				0.0		4.77	5.67	4.70	0.0	0.0	2.0
		6.0					0.132			108	1.03	1.03			6.85	0.0		6.10	5.97	6.04	0.0	0.0	0.0
		7.0					0.169			84	0.96	0.48			7.19	0.0		6.41	6.28	6.41	1.0	1.0	0.0
	017-002	5.0	3.425	5.00		0.067	0.271			166	0.64	0.69	7.40	7.08		0.0	0.914	6.43	3.38	5.81	5.0	6.0	15.0
		6.0					0.247			48	1.12	1.06	7.40	5.87	7.14	23.6	0.909	6.43	6.03	6.27	7.0	4.0	9.8
		7.0					0.382			63	1.09	1.04	7.42	6.93	7.18	0.0	0.914	6.63	5.67	6.15	4.0	4.0	11.1

REFERENCES

1. Kemp, N. H.; Rose, P. H.; and Detra, R. W.: Laminar Heat Transfer Around Blunt Bodies in Dissociated Air. Avco-Everett Research Laboratory Report RR 15, May 1968.

2. Dorrance, W. H.: Viscous Hypersonic Flow. McGraw-Hill, New York, 1964.

3. Moore, F. K.: "Hypersonic Boundary Layer Theory," Theory of Laminar Flows. edited by F. K. Moore, Princeton University Press, Princeton, N. J., 1964, pp 439-527.

4. Lees, L.: "Laminar Heat Transfer over Blunt Nose Bodies at Hypersonic Flight Speeds," Jet Prop. Vol 26, No. 11, November, 1956, pp 259-269.

5. Fay, J. A.; and Riddell, F. R.: "Theory of Stagnation Point Heat Transfer in Dissociated Air," J. Aeron. Sci., Vol 25, No. 2, February 1958, pp 73-85.

6. Stetson, K. F.: "Boundary-Layer Transition on Blunt Bodies with Highly Cooled Boundary Layers," J. Aeron. Sci., Vol 27, No. 2, February 1960 pp 81-91.

7. Reshotko, E.; and Tucker, M: Approximate Calculation of the Compressible Turbulent Boundary Layer with Heat Transfer and Arbitrary Pressure Gradient. NACA Report TN 4154 December, 1957.

8. Stewartson, K.: "Correlated Incompressible and Compressible Boundary Layers," Proc. Roy. Soc. (London). 22 December 1949; Ser. A, Vol 200, No. A 1060, pp 84-100.

9. Ludwieg, H.; and Tillmann, W.: Investigations of the Wall-Shearing Stress in Turbulent Boundary Layers. NACA TM-1285, 1950.

10. Jaremenko, I. M.: "Aerodynamic Characteristics of the Ballute in the 0.1 to 10 Mach Number Speed Regime." Presented at the AIAA 5th Aerospace Sciences Meeting in New York, 23-26 January 1967 (AIAA Paper No. 67-228).

11. Levensteins, Z. J., and Krumins, M. V.: "Experimental Study of Aerodynamic Characteristics of Hypersonic Wakes." Presented at the AIAA 3rd Aerospace Sciences Meeting held in New York, 24-26 January 1966 (AIAA Paper No. 66-53).

12. Pallone, A.; Erdos, J.; and Eckerman, J.: "Hypersonic Laminar Wakes and Transition Studies," AIAA Journal. Vol 2, No. 5, May 1964, pp 855-863.

13. Zakkay, V.; and Fox, H.: "An Experimental and Theoretical Investigation of the Turbulent Far Wake," AIAA Journal. Vol 5, No. 3, March 1967, pp 568-574.

14. Nerem, R. M.: "Pressure and Heat Transfer on High-Speed Aero-
    Dynamic Decelerators of the Ballute-Type," Proceedings of the AIAA
    Aerodynamic Deceleration Systems Conference, Houston, Texas, 7-9
    September 1966, AIAA, New York, 1966.

15. Reeves, B. L., and Lees, L: "Theory of the Laminar Near Wake of
    Blunt Bodies in Hypersonic Flow," AIAA Journal. Vol 3, No. 11,
    November 1965, pp 2061-2074.

16. McCarthy, J. F., Jr. and Kubota, T.: "A Study of Wakes Behind a
    Circular Cylinder at M = 5.7," AIAA Journal. Vol 2, No. 4, April
    1964, pp 629-636.

17. Dewey, C. F., Jr.: "Near Wake of a Blunt Body at Hypersonic Speeds,"
    AIAA Journal. Vol 3, No. 6, June 1965, pp 1001-1010.

18. Zakkay, V.; and Cresci, R. J.: "An Experimental Investigation of the
    Near Wake of a Slender Cone at M_{∞} = 8 and 12," AIAA Journal. Vol 4,
    No. 1, January 1966, pp 41-46.

19. Todisco, A.; and Pallone, A.: "Measurements in Laminar and Turbu-
    lent Near Wakes." Presented at the AIAA 5th Aerospace Sciences Meet-
    ing held in New York, 23-26 January 1967 (AIAA Paper No. 67-30).

20. Webb, W. H.; Golik, R. J.; Vogenitz, F. W.; and Lees, L.: "A Multi-
    moment Integral Theory for the Laminar Supersonic Near Wake," Pro-
    ceedings of the 1965 Fluid Mechanics and Heat Transfer Institute. A.
    F. Charwat, editor; Stanford University Press, 1965, pp 168-189.

21. Webb, W. H.; Golik, R. J.; and Lees, L.: "Preliminary Study of the
    Viscous Inviscid Interaction in the Laminar Supersonic Near Wake."
    TRW Space Technology Laboratories, Report No. 6453-6004-KU-000
    (also BSD-TDR-64-114), July 1964.

22. Golik, R. J.; Webb, W. H.; and Lees, L.: "Further Results of Viscous
    Interaction Theory for the Laminar Supersonic Near Wake." Presented
    at the AIAA 5th Aerospace Sciences Meeting held in New York, 23-26
    January 1967 (AIAA Paper No. 67-61).

23. Weiss, R. F.: "A New Theoretical Solution of the Hypersonic Near
    Wake." Presented at the AIAA 5th Aerospace Sciences Meeting held in
    New York, 23-26 January 1967 (AIAA Paper No. 67-63).

24. Bauer, A. B.: "Some Experiments in the Near Wake of Cones," AIAA
    Journal. Vol 5, No. 7, July 1967, pp 1356-1358.

25. Bauer, A. B.: Effect of Vehicle and Fluid Injection Geometrics on the
    Near Wake Flow Field Structure. Aeronutronic Division, Philco-Ford
    Corporation, Publication No. U-4028 (NASA N67-23411). 15 February
    1967.

26. Sato, H., and Kuriki, K.: "The Mechanism of Transition in the Wake of
    a Thin Flat Plate Placed Parallel to a Uniform Flow," J. Fluid Mechan-
    ics. Vol 11, November 1961, pp 321-352.

27. Todisco, A.; and Pallone, A.: _Near Wake Flow Field Measurements._
AVCO RAD-TM-65-21, May 1965.

28. Todisco, A.; Pallone, A.; and Heron, K.: "Hot-Wire Measurements
of the Stagnation Temperature Field in the Wake of Slender Bodies."
AVCO RAD-TM-64-32, July 1964.

29. Ragsdale, W. C.; and Darling, J. A.: "An Experimental Study of the
Turbulent Wake Behind a Cone at M = 5," _Proceedings of the 1966 Heat_
Transfer and Fluid Mechanics Institute, M. A. Saas and J. A. Miller,
editors; Stanford University Press, 1966, pp 198-209.

30. Martellucci, A.; Trucco, H.; and Agnone, A.: "Measurements of the
Turbulent Near Wake of a Cone at Mach 6," _AIAA Journal._ Vol 4, No. 3
March 1966, pp 385-391.

31. Muntz, E. P.; and Softley, E. J.: _An Experimental Study of Laminar_
Near Wakes. General Electric TIS R65SD6, April 1965.

32. Sims, L. W.: _The Effects of Design Parameters and Local Flow Fields_
on the Performance of Hyperflo Supersonic Parachutes and High Dynamic
Pressure Parachute Concept. AFFDL-TR-65-150, Vol I, October 1965.

33. Nebiker, F. R.: _Aerodynamic Deployable Decelerator Performance -_
Evaluation Processor. AFFDL-TR-65-27, Vol I, May 1965.

34. Heinrich, H. G.; Rose, R. E.; and Kovacevic, N. D.: _Flow Character-_
istics of Rigid Ribbon Parachute Canopies in Supersonic Flow. AFFDL-
TR-65-103, December 1965.

35. Mirels, H.: _Theoretical Wave Drag and Lift of Thin Supersonic Ring_
Airfoils. NACA TN-1768, 1948.

36. Low, M.: "Boundary-Layer Transition at Supersonic Speeds." NACA
RM E56E10, 1956.

37. Gazley, C., Jr.: "Boundary Layer Stability and Transition in Supersonic
Flow," _J. Aeron. Sci.,_ January 1953.

38. Steinback, C. P.: "Some Effects of Roughness and Variable Entropy on
Transition at a Mach Number of 8." AIAA Paper No. 67-132.

39. Deem, R. E.: "Boundary Layer Transition at Hypersonic Speeds."
SM-43056, January 1964.

40 Stewart, D. G.: "Some Observations of Boundary Layer Transition on
Cones at Subsonic and Supersonic Speeds." ARL/ME-267, May 1965.

41. Schlichting, H.: _Boundary Layer Theory._ McGraw-Hill, New York,
1960.

42. Korkegi, R.: "Transition Studies and Skin Friction Measurements on an
Insulated Flat Plate at a Mach Number of 5.8," _J. Aeron. Sci._ Vol 25,
No. 2, February 1956, p 97.

43. Nagamatsu, H. T.; Sheer, R. E.; and Graber, B. C.: "Hypersonic Laminar Boundary Layer Transition on an Eight-Foot Long, Ten-Degree Cone, $M_1 = 9.1 - 16$." AIAA Paper No. 66-494 presented at the 4th Aerospace Sciences Meeting, Los Angeles, June 1966.

44. Braslow, A. L.: "A Review of Factors Affecting Boundary Layer Transition." NASA TN D-3384, August 1966.

45. Diaconis, N. S.; Wisniewski, R. J.; and Jack, J. R.: "Heat Transfer and Boundary Layer Transition on Two Blunt Bodies at Mach Number 3.12." NACA TN 4099, October 1957.

46. Stetson, K. F.: "Boundary Layer Transition on Blunt Bodies with Highly Cooled Boundary Layers," J. Aeron. Sci. Vol 27, No. 2, December 1957, p 885.

47. Van Driest, E. R., and Boison, J. C.: "Experiments on Boundary Layer Transition at Supersonic Speeds," J. Aeron. Sci. Vol 24, No. 12, December 1957, p 885.

48. Reshotko, E.: "Transition Reversal and Tollmien-Schlicting Instability," Phys. Fluids. Vol 6, No. 3, March 1963, p 335.

49. Stetson, K. F., and Rushton, G. H.: A Shock Tunnel Investigation of the Effects of Nose Bluntness, Angle of Attack and Boundary Layer Cooling on Boundary Layer Transition at a Mach Number of 5.5. AIAA Paper No. 66-495 presented at the AIAA 4th Aerospace Sciences Meeting, Los Angeles, June 1966.

50. Lees, L., and Hromas, L. A.: "Turbulent Diffusion in the Wake of a Blunt Nosed Body at Hypersonic Speeds," J. Aeron. Sci. Vol 29, No. 8, August 1962, pp 976-993.

DOCUMENT CONTROL DATA - R & D

(Security classification of title, body of abstract and indexing annotation must be entered when the overall report is classified)

1. ORIGINATING ACTIVITY (Corporate author)	2a. REPORT SECURITY CLASSIFICATION
Goodyear Aerospace Corporation 1210 Massillon Road Akron, Ohio	Unclassified
	2b. GROUP

3. REPORT TITLE

ESTABLISHMENT OF AN UNSYMMETRICAL WAKE TEST CAPABILITY FOR AERODYNAMIC DECELERATORS, VOLUME II, ANALYSIS OF HIGH-SPEED AXISYMMETRIC WAKES AND PARASONIC PARACHUTE PERFORMANCE

4. DESCRIPTIVE NOTES (Type of report and inclusive dates)

Final Report - 1 March 1966 to 15 January 1968

5. AUTHOR(S) (First name, middle initial, last name)

Henke, Daniel W.

6. REPORT DATE	7a. TOTAL NO. OF PAGES	7b. NO. OF REFS
March 1968	152	50

8a. CONTRACT OR GRANT NO	9a. ORIGINATOR'S REPORT NUMBER(S)
AF33(615)-3595	
b. PROJECT NO 6065	GF.-13528
c. Task 606507	9b. OTHER REPORT NO(S) (Any other numbers that may be assigned this report)
d.	AFFDL-TR-67-192, Volume II

10. DISTRIBUTION STATEMENT
This document is subject to special export controls, and each transmittal to foreign governments or foreign nationals may be made only with prior approval of the Air Force Flight Dynamics Laboratory (FDFR), Wright-Patterson Air Force Base, Ohio 45433.

11. SUPPLEMENTARY NOTES	12. SPONSORING MILITARY ACTIVITY
	Air Force Flight Dynamics Laboratory Wright-Patterson AFB, Ohio 45433

13. ABSTRACT

Methods were developed to predict the boundary layer and wake characteristics of symmetric bodies moving at supersonic speeds. The methods developed for predicting boundary layer characteristics are applicable to both laminar and turbulent flow over axisymmetric or two-dimensional bodies and can be used as an approximation for the flow over quasisymmetric bodies. The wake predictive methods were developed for axisymmetric flow and are applicable to both laminar and turbulent wakes. The aforementioned methods were combined and programmed so that wake profiles can be determined based only on inputs of forebody geometry and free-stream conditions.

Also presented is a method for calculating the drag of PARASONIC parachutes using the flow field immediately ahead of the parachute as the free-stream conditions. An analysis of the effects of various geometric and free-stream parameters on PARASONIC parachute performance was conducted and trends determined.

The distribution of this abstract is unlimited.

DD FORM NOV..1473

14. KEY WORDS	LINK A		LINK B		LINK C	
	ROLE	WT	ROLE	WT	ROLE	WT
Boundary Layer						
Boundary Layer Transition						
Supersonic Wake Flow						
Aerodynamics						
Aerodynamic Decelerator						